Improving the Efficacy of Dynamic, Gradient-Based Falling Weight Deflectometer Backcalculation

By

Ryan Christopher Romeo

(Under the Direction of R. Benjamin Davis and S. Sonny Kim)

Abstract

The falling weight deflectometer (FWD) is a type of nondestructive testing equipment used to evaluate the stiffness of asphalt pavements. For the test procedure, the FWD briefly impacts the pavement, and displacement sensors measure the pavement's vibration at several locations. Afterward, a backcalculation method estimates the pavement's stiffness by analyzing the vibration measurements. Typical backcalculation methods comprise two components: a computer model that simulates the FWD test, and an optimization scheme to estimate the pavement's material properties. The optimizer intelligently varies the material properties in the model until the simulated deflections closely match the measured deflections. FWD testing has become the most widely used approach for nondestructive pavement evaluation, and numerous techniques have been developed to improve backcalculation accuracy. However, these developments increase the method's complexity, which brings forth new issues to be investigated.

The contents of this dissertation are organized into four key aspects. The first is the introduction of a new FWD backcalculation software, UGA-PAVE, which employs a state-of-the-art numerical pavement model, ViscoWave, and a novel gradient-based optimization algorithm, tandem trust-region. Second, verification and validation studies are conducted with the software which shed insight on ill-posed backcalculation and the effective frequency range—two prevalent issues hindering modern backcalculation efficacy. Third, a study comprising 720,000 simulated backcalcu-

lations is conducted to identify changes to the FWD testing procedure with the goal of increasing backcalculation accuracy. Fourth, improvements are presented for a widely used approach to approximate interconversion between two primary models of viscoelastic stiffness: dynamic modulus and relaxation modulus.

The results of these studies improve the efficacy of FWD backcalculation. The development, verification, and validation of UGA-PAVE highlights the importance of research on ill-posed optimization and the effective frequency range in FWD backcalculation, which is virtually nonexistent at present. The test procedure examination provides changes to the design of FWD equipment that can improve accuracy of current and future backcalculation approaches. Finally, the interconversion method is particularly useful for FWD backcalculation, because they are typically designed to output results in the form of one viscoelastic modulus but not the other.

Index Words: Falling Weight Deflectometer, Dynamic Backcalculation, Flexible Pavements, Gradient-Based Optimization, Viscoelasticity

Improving the Efficacy of Dynamic, Gradient-Based Falling Weight Deflectometer Backcalculation

By

Ryan Christopher Romeo

B.S., The University of Georgia, 2017

A Dissertation Submitted to the Graduate Faculty of The University of Georgia in Partial Fulfillment of the Requirements for the Degree

Doctor of Philosophy

Athens, Georgia

2022

Improving the Efficacy of Dynamic, Gradient-Based Falling Weight Deflectometer Backcalculation

By

Ryan Christopher Romeo

Major Professors: R. Benjamin Davis
S. Sonny Kim

Committee: Hyung S. Lee
Stephan A. Durham
Javad Mohammadpour Velni

Electronic Version Approved:

Ron Walcott
Vice Provost for Graduate Education and Dean of the Graduate School
The University of Georgia
December 2022

Acknowledgments

This accomplishment was made possible from the support of my friends and loved ones. To my girlfriend, Sohyun, I can't express my appreciation for you. I surely would have lost motivation without your love and encouragement these last few semesters. To my lab fellows over the years, you all hold a special place in my heart. The long hours of grueling work was made bearable by the atmosphere we created together. I dearly treasure the friendships I have made during my time here, and I will forever remember these years fondly thanks to each and every one of you.

I would also like to thank the members of my committee Drs. Hyung Lee, Stephan Durham, and Javad Mohammadpour for your mentorship along this journey. You have been instrumental by lending me guidance in my times of need. I sincerely appreciate all the kindness, patience, and criticism you've given me. To my co-advisor, Dr. Sonny Kim, I feel great honor for the trust you placed in me. Your knowledge and expertise is nothing short of inspirational, and I will always cherish the experience of working with you. To my advisor, Dr. Ben Davis, I cannot express the appreciation I have for you. You saw something in me that I did not initially see in myself, and you gave me the confidence and the courage to make it to where I am today. You have had the single greatest impact on my career, and I will forever be grateful that you entered my life.

Finally, I want to thank my mother and late father for their love and support in my life. To my mother, Lynn, you have undoubtedly had the largest influence on the person I am today. You taught me to be rational, never doubt my ability, and always give my all—the traits without which I would have been unsuccessful in this endeavor. To my father, Chris, you have been the primary source from which I derive my motivation and ambition. The greatest pain in my life is that you cannot be here to share this moment with me, because it is thanks to you that I can experience my greatest joy in this achievement.

Contents

List of Figures

List of Tables

Chapter 1

Introduction

1.1 Motivation

The falling weight deflectometer (FWD) is currently the most popular nondestructive testing (NDT) approach to evaluate the *in situ* stiffness of asphalt concrete pavements. The testing procedure involves dropping a heavy weight onto the pavement surface while numerous deflection sensors measure the resulting vibration. Over the years, FWD backcalculation methods have been developed to estimate the pavement's stiffness by analyzing the force and deflection measurements.

The backcalculation procedure is classified as an inverse problem, which is a prevalent area of study in modern computational engineering. Inverse problems have been discovered in a variety of scientific/mathematical contexts and are notoriously difficult to solve. FWD backcalculation has been used in the United States since the 1980s and has seen continuous research and development since its implementation. Many great strides have been made to improve the accuracy and efficiency of backcalculation methods. However, these improvements increase the sophistication of the method, which begets increased complexity of the issues that arise.

The FWD testing procedure in general has remained largely unchanged since its original inception, and it has become apparent that some of the most pervasive computational issues stem from the experimental configuration. The computational methods have seen significant advancement in the last decade; however, the benefits garnered from these improvements are limited due to the testing procedure. In this dissertation, modern FWD backcalculation is examined from an analyst's perspective. Results from the included studies are aimed toward improving the efficacy and prac-

ticality of FWD backcalculation, and special attention is given to the most severe computational issues—namely ill-posedness and the effective frequency range.

1.2 Outline and Contributions

Falling weight deflectometer backcalculation comprises two key computational aspects: a physics simulation that models the pavement's response to an FWD test, and an optimization scheme that estimates the pavement's stiffness by identifying parameters in the model which minimize the difference between the simulated and measured responses. Although extensive research has been conducted on FWD backcalculation, the vast majority has focused on improving the pavement models. In this dissertation, a new backcalculation software is developed and extensively used to study the most crucial issues plaguing FWD backcalculation. The results are aimed toward improving the effectiveness and practicality of FWD backcalculation, with heavy emphasis on the optimization aspect of backcalculation methodology.

First, a literature review on relevant topics is conducted in Chapter 2. Then, in Chapter 3, a theoretical description is presented for the new backcalculation software, UGA-PAVE. The software combines two state-of-the-art computational techniques. The first is ViscoWave, a finite layer method developed by Lee [7] for modeling the dynamic response of viscoelastic pavements. The second is tandem trust-region, a novel optimization algorithm developed specifically for UGA-PAVE. A demonstration of UGA-PAVE's operation and usage is provided following the theoretical description.

In Chapter 4, the UGA-PAVE software is verified in 36,000 simulated backcalculations. The primary motivation is to backcalculate accurate pavement material properties when the optimization is ill-posed, which is a pervasive issue in FWD practice that occurs when there are more backcalculated variables than measurements. Additionally, this chapter contains an important demonstration of the effective frequency range, another crucial issue in FWD practice which greatly hinders the accuracy of the backcalculate result.

In Chapter 5, UGA-PAVE's backcalculation performance is validated with lab-measured data. The most important material properties in FWD backcalculation pertain to the dynamic modulus, whereby asphalt's viscoelastic stiffness is represented as a function of frequency. Currently, the most

reliable way to measure dynamic modulus is to test pavement cores (*i.e.*, cylindrical samples cut from a pavement) with an asphalt mixture performance tester (AMPT). For the validation study, asphalt cores and FWD testing are conducted at the same locations; then, the dynamic modulus backcalculated by UGA-PAVE is compared to that measured from AMPT. Results highlight the importance of having accurate knowledge of the thicknesses and types of materials underneath the asphalt layer. Additionally, consequences of the effective frequency range are demonstrated in a practical context.

In Chapter 6, the FWD testing procedure is examined in rigorous detail across 720,000 simulated backcalculations. A multitude of different testing configurations are designed to investigate the effects of the FWD load characteristics and the number of measurement devices on backcalculation accuracy. Ill-posed optimization and the effective frequency range are heavily considered to suggest changes to the FWD testing methodology that can significantly improve backcalculation performance. The most importance changes involve using at least as many deflection sensors as backcalculated variables, as well as designing FWD equipment to impact the pavement for a brief a duration as possible.

In Chapter 7, a widely used technique for approximate pavement modulus interconversion is improved based on a rigorous analysis of 30 asphalt samples. Asphalt's viscoelastic stiffness is often represented as a function of time via relaxation modulus, or as a function of frequency via dynamic modulus. Backcalculation methods are typically designed to output one modulus but not the other; however, different situations exist where using the other modulus is more favorable. The improved approach serves as a tool that can be implemented in a matter of seconds to convert pavement modulus with less than 1.5% error on average.

Finally, the major conclusions from this work are discussed in Chapter 8, and the author's views on the current state of FWD backcalculation and future directions are given.

The principal contributions of this work are summarized as:

1. Development of a novel optimization technique, tandem trust-region, for ill-posed falling weight deflectometer backcalculation;

2. Introduction of a dynamic, gradient-based FWD backcalculation software, UGA-PAVE;

3. Verification of UGA-PAVE for ill-posed backcalculation using 36,000 unique simulated backcalculation scenarios;

4. Validation of UGA-PAVE for dynamic modulus backcalculation by comparing backcalculated results to lab-measured results for nine pavement samples of hot mix asphalt;

5. Investigations of the effective frequency range (via FWD pulse characteristics) and ill-posed optimization (via quantity of displacement sensors) on the efficacy of FWD backcalculation using 720,000 unique simulated backcalculation configurations;

6. A robust numerical study of 30 hot mix asphalt samples to improve a popular approximate interconversion technique between dynamic modulus and relaxation modulus.

Chapter 2

Background

2.1 Falling Weight Deflectometer Backcalculation

Numerous FWD backcalculation methods have been developed over the years, and they generally comprise two components: a numerical physics model to simulate the pavement's response to the FWD impact, and a numerical scheme to estimate the layer parameters. Two of the most popular classes of numerical schemes are machine learning and gradient-based optimization—the latter of which is of particular interest in this dissertation. In this chapter, reviews are conducted on literature relevant to the present topics, including the history of the FWD, advancement of the pavement models and optimization methods, and the development of interconversion techniques.

2.1.1 FWD Development and Usage

The FWD was originally developed in France, and its early development and implementation is largely credited to Danish engineers. By 1972, their efforts culminated in the production of approximately 20 impact testing devices based on the FWD [8]. At the same time, the Swedish National Road Administration began using FWDs for its pavement testing [9]. The general design and operation of these devices are largely the same as modern FWD variants, such as the Phoenix FWD developed by Phoenix International A/S in the 1970s. The device was affixed to a small trailer that can be hitched to a towing vehicle for easy transport to desired testing locations. The weights, drop heights, and load plate diameters of FWDs were relatively similar to American impact testing devices. However, in an FWD the weight falls onto a spring damping system which

generates a force pulse resembling a half-sine wave; additionally, the load plate is typically covered with a rubber material to facilitate a uniform distribution of the impact load across the plate [10].

During this time, researchers in the United States focused on development of their own impact load devices. The genesis of flexible pavement impact testing in the United States can be traced to the Cornell Aeronautical Laboratory (CAL), which developed a trailer-mounted impact tester in the early 1960s to detect seasonal variations in flexible pavement stiffness [11]. The CAL device involved dropping a 227 kg weight up to 1.2 m above the pavement. When released, the weight would strike an aluminum plate that was 38 cm in diameter and 2.5 cm thick, and two displacement sensors would measure the response at the surface. From preliminary testing, CAL researchers concluded that impact testing could be a viable NDT approach for flexible pavements by analyzing the peak deflection response of each sensor. Later in 1972, Washington State University (WSU) developed two impact testing instruments: a highly portable version residing in a suitcase, and a larger variant equipped to a vehicle [12, 13]. Both versions used an impact hammer to create the load and two piezoelectric transducers to measure the deflection response. The WSU researchers' method involved placing one transducer adjacent to the load point and the other 45 cm away; then, they calculated an "Impulse Index" by taking a ratio between the time integrals calculated from both sensors' measurement histories. The researchers found good agreement with results from Benkelman Beam and Dynaflect measurements—two popular NDT devices at the time that used static and steady-state harmonic loading, respectively.

After seeing its effectiveness in Europe, United States institutions had started to abandon their own designs in favor of the FWD. By 1985, the FWD had been adopted by several state agencies, including those of Arizona, Florida, and Minnesota [9]. The most popular commercial products at that time were the Dynatest Model 8000, KUAB, and Phoenix FWDs. Over time, the most popular FWD analysis approach has been backcalculation (a portmanteau of *backward* and *calculation*) [14], whereby an optimization method iteratively adjusts material property values and runs a computational model of the pavement section until the difference between the simulated and measured deflections is minimized. Despite the loads and deflections being dynamic in nature, traditional backcalculation methods are based on static interpretations of the FWD measurements [15–17]. Specifically, only the peak load and peak deflections measured by each transducer are considered, as opposed to using the entire load and deflection time histories. Such analyses are

prone to inaccuracies due to the viscoelastic nature of asphalt concrete in flexible pavements [18–20], where the material's stiffness varies with both temperature and the rate of loading. Thus, dynamic backcalculation methods have been developed which offer increases to accuracy by considering multiple time points in each deflection sensor time history [19, 21–27].

Traffic speed deflection devices (TSDDs) have recently emerged as nondestructive testing instruments that use a moving load instead of an impact excitation, and can be interpreted as the natural progression of impact-based methodology. In general, TSDDs are large vehicles which are similar in appearance to freight trucks. Displacement sensors are placed both upstream and downstream of a particular wheel pair, and deflections are measured as the vehicle travels at typical traffic speeds. Because of their high mobility, TSDDs allow for dramatically faster data collection compared to FWD, and many moving-load pavement models [28–31] and backcalculation methods [32–38] have been developed since its inception. However, TSDD backcalculation approaches have yet to see extensive development due to its recent emergence, and FWD-based methods remain the current standard of practice [34, 39, 40].

2.1.2 Forward Problem Models for FWD Backcalculation

Pavement models based on the finite element method has been shown to be effective for predicting dynamic response of flexible pavements [15, 16, 18]. However, when modeling dynamic pavement responses, significant errors can arise due to the reflection of waves at the edges of bounded domains. Thus far, the solution to this problem has been to increase the domain of the model to the point where the effects of the reflections become negligible; this creates computationally expensive models which are impractical to use [17]. Recent efforts have made progress on the issue of wave reflection for bounded domains. One approach is that of the Perfectly Matched Layer (PML). The method was originally devised by Berenger [41] for use with electromagnetic analysis, and Basu and Chopra [42] later adapted the technique for use in elastodynamics. In PML, an artificial layer is created at the boundary of the FEM domain. When waves reach the PML interface, a coordinate transform is applied that causes them to exponentially decay. Recently, Madsen et al. [43] adapted the PML to a moving frame of reference for use with Rolling Weight Deflectometer testing; however, the technique was not experimentally validated.

Another technique is that of the enriched/enhanced finite element method (EFEM) initially proposed by Kohno et al. [44] for one-dimensional cases. In their technique, the dynamic model is constructed using low-order finite elements which are then "enriched" using harmonic functions, which increase the number of degrees of freedom in the element. Typically in FEA, higher degrees of freedom are achieved in an element by increasing its polynomial order of approximation (*i.e.*, parameters such as stress and displacement vary within the element according to the degree of polynomial). For dynamic problems of wave propagation, this enrichment using harmonic functions is more computationally efficient that increasing the order of approximation, because an infinite series of polynomials is required to exactly represent a sinusoid. Ham and Bathe [45] later extended EFEM to multi-dimensional applications; however, they did not compare the method's effectiveness to its computational expense.

The Layer Transfer Matrix Method (LTMM) was developed to solve for continuous harmonic responses in layered media [46, 47]. The technique is formulated similarly to FEA by defining a relationship between the forces and resulting displacements at nodes in the interfaces between material layers, and the technique was further improved by Kausel and Roësset [48] by reformulating the layer transfer matrix in symmetric form. However, the method involves solving a set of continuous transcendental equations requiring improper integration, which can create difficulties for numerical computations. Kausel and Roësset [48] also developed a semi-discrete solution for solving harmonic responses in layered media by generalizing Lysmer's [49] Lumped Mass Method (LMM). By dividing each material layer into sublayers thinner than the wavelengths of interest, the set of transcendental equations from the continuous solution can be replaced with a more numerically robust eigenvalue problem. However, the subdivision of each layer significantly increases computational expense due to the higher number of equations to be solved.

The Spectral Element Method (SEM) developed by Rizzi and Doyle [50, 51] solves for the harmonic motions of layered media by incorporating elements from the previously mentioned methods. The technique circumvents the needs for the improper integration in LTMM by employing the Discrete Fourier Transform (DFT) to convert from the time domain to the frequency domain and then performing a double summation over the frequencies and wavenumbers of interest. In addition, the need for layer subdivisions from LMM is eliminated by modeling the mass distribution of each layer exactly. Al-Khoury *et al.* [52–54] developed axisymmetric spectral elements for use

with layered media modeled as geometric half-spaces and demonstrated the method's viability for pavement FWD problems, considering both linearly elastic and viscoelastic element formulations. Finite Layer methods (FLM) are similar to SEM in that they use the DFT to solve the system of equations in the frequency domain [23, 55, 56]. However, FLMs compute unit impulse responses at discrete frequencies, convert them to the time domain, and then convolve them with the FWD load to determine the surface deflections.

A significant problem with the aforementioned techniques is that they use the Discrete Fourier Transform (DFT) to convert between the time and frequency domains. FWD time-histories are transient nonperiodic signals, often containing a non-negligible amount of noise, and they are measured only for a short duration wherein the pavement does not come to rest. Additionally, a large number of harmonics are required to model flexible pavements in the frequency domain due to their viscoelastic nature. For these reasons, it has been shown [23, 56–59] that DFT is not an effective tool for time conversion of such signals. The ViscoWave algorithm developed by Lee [7, 25, 60] is a recent FLM technique that has eliminated this problem by instead using both the Laplace and Hankel transforms, and it has been shown to successfully reconstruct asphalt master curves [61]. In addition, previous Finite Layer Models [23, 55, 56] required layer subdivisions for sufficient accuracy akin to LMM; however, ViscoWave improves computational efficiency by incorporating Al-Khoury's spectral element definitions which do not require sublayers.

2.1.3 Optimization Methods for FWD Backcalculation

Traditional backcalculation approaches typically involve gradient-based optimization, and in recent years, machine learning methods such as artificial neural networks (ANNs) have become a popular choice for FWD backcalculation [19, 22, 27, 62–66]. However, ANN validation using field measurements has revealed that the accuracy of ANN methods is often insufficient for FWD backcalculation; consequently, optimization schemes via genetic algorithms (GAs) have been applied to ANNs to improve their accuracy. Li and Wang [27, 67] performed studies where they developed and tested ANN-GA programs capable of FWD backcalculation of load-displacement responses and viscoelastic material properties in flexible pavements. They used axisymmetric FEMs in ABAQUS to create a database of synthetic relationships describing how variations in dynamic loading, material properties, and temperature affect the pavement response. This synthetic database was then

used to create the training and verification sets for the ANN-GA program, and the program was validated using a pavement section from the long-term pavement performance database. It was found that the ANN-GA technique had great accuracy, though it is limited to the range of parameters used to create the synthetic database and requires further development. Such methods offer significantly reduced backcalculation time with similar accuracy when compared to gradient-based techniques, but they require a large volume of training data, and their applicability is constrained by the range of configurations included in these data [17].

Due to the limitations and ongoing development of machine learning methods, gradient-based optimization is still a popular choice for modern FWD backcalculation methods; however, it remains challenging because the optimization problem is ill-posed [68]. Analogous to an underdetermined system of linear equations, ill-posedness refers to having more estimation parameters (*e.g.*, material property variables) than observations (*e.g.*, deflection sensor time histories). The issue of ill-posedness becomes increasingly problematic as backcalculation methods are improved, because the computational pavement models are formulated with higher fidelity. In reality, the asphalt concrete layer often comprises up to three lifts, or sub-layers, of distinct asphalt mixture types. Historically, the pavement structure has been modeled by aggregating the asphalt lifts as a single layer to reduce the number of parameters in the optimization. Such an approach is effective for reducing the degree of ill-posedness, but it is a fundamentally inaccurate representation of the real structure.

An ill-posed optimization contains a myriad of non-unique solutions [19, 69], and the issue has been studied extensively in other research spaces (*e.g.*, see *Journal of Inverse and Ill-Posed Problems*). In FWD backcalculation, the non-unique solutions manifest as different sets of stiffness parameters for which the model generates near-identical deflection time histories. Consequently, the optimizer will likely encounter significant difficulty in identifying the correct parameters for the pavement's viscoelastic stiffness. Despite the gravity of this issue, there is an apparent lack of research regarding the topic in the context of FWD backcalculation.

2.2 Pavement Modulus Interconversion

Asphalt's viscoelastic stiffness is often expressed via dynamic modulus, $|E^*|$—a function of loading frequency in Hz—or by relaxation modulus, $E(t)$—a function of loading time in seconds. Because these material response functions represent the modulus in different domains, choosing between them typically depends on the usage scenario [70, 71]. In general, dynamic modulus is favorable for describing viscoelastic materials under periodic excitation, whereas relaxation modulus is more suitable for sustained loads. It is common in practice for pavement engineers to have asphalt stiffness represented by one modulus but not the other; then, when a situation arises where it is preferable to use the other stiffness function, they require some way to convert between them. This general concept is referred to as interconversion, and it is useful in the context of FWD backcalculation methods because they typically output either $|E^*|$ or $E(t)$ (*e.g.*, see Refs. [17, 19, 25–27, 72–74]).

Several exact interrelationships [75–78] have been determined between relaxation modulus and the storage and loss moduli, $E^{'}$ and $E^{''}$, which are the components of dynamic modulus. Most exact interconversion methods contain integrals with infinite bounds that are difficult to evaluate analytically and numerically [79]. Exact analytical conversion is manageable when a Prony series expression is obtained for any one of $|E^*|$, $E^{'}$, $E^{''}$, or $E(t)$; however, the moduli are often modeled in practice using sigmoidal functions which do not have closed-form interrelationships. Consequently, pavement engineers have developed approximate relationships between the dynamic and relaxation moduli to facilitate quick interconversion with acceptable costs to accuracy.

The earliest approximate technique is the Ninomiya-Ferry (NF) method [80], which can interconvert between the storage, loss, and relaxation moduli, and it was later shown by Fernández *et al.* [81] that the NF method is suitable for converting the $E^{'}$ and $E^{''}$ of polymethyl methacrylate materials to $E(t)$. However, the method requires two of the moduli to be known for estimation of the third, which is practical for conversion from $|E^*|$ to $E(t)$ but not vice versa. The Park-Schapery (PS) method [82] has also been developed, which involves adjustment factors based on sinusoids and gamma functions to interconvert among $E^{'}$, $E^{''}$, and $E(t)$. Mun *et al.* [83] compared the PS approach to exact Prony series interconversion and found they produced similar results with asphalt concrete materials. Recently, Tarefder and Asifur Rahman [84, 85] proposed a method for

converting from $|E^*|$ to $E(t)$ wherein the Prony series expression for $E^{'}$ is fit to $|E^*|$ data, but they found poor agreement with experimental data.

Apart from the aforementioned techniques, several approximate methods have been developed based on a direct relationship between the time and frequency domains. The origin of these approaches is often attributed to Christensen [77], who derived an approximate interrelationship between the storage and relaxation moduli. The relationship is remarkably simple, whereby conversion between the time and frequency domains is approximated by $t = 1/\pi^2 f \approx 0.1/f$. Specifically, if the storage modulus is known at a frequency point, then the relaxation modulus is assumed to have the same value at the corresponding time point given by the interrelationship. Since its introduction, $|E^*| \leftrightarrow E(t)$ interconversion has often been performed based on this simplified approximation with the general form $t = \beta/f$, but there is an apparent lack of consensus on the generally appropriate value of the time-frequency equivalency factor, β [70]. Daniel and Kim [86] proposed using $\beta = 0.08$ based on an internal study involving conversion between creep compliance and complex compliance. Alternatively, a common value used by viscoelastic rheologists is $\beta \approx 0.16$ based on the relationship between time and temporal frequency $t = 1/2\pi f$ [87, 88]. Furthermore, a research project as part of the Mechanistic-Empirical Pavement Design Guide recommends $\beta = 1$ [70]. A summary of these values are given in Table 2.1.

Table 2.1. Table of proposed values for the time-frequency equivalency factor, β.

Source	Author	β
NCHRP 9-29 Report	R. Bonaquist	1
Textbook [76]	J. D. Ferry	$1/2\pi$
Personal Correspondence [70]	M. G. Sharma	$1/2\pi$
Textbook [77]	R. M. Christensen	$1/\pi^2$
Personal Correspondence [70]	R. Schapery	0.1
Journal Paper [86]	J. S. Daniel and Y. R. Kim	$1/4\pi$

2.3 Issues with FWD Testing Methodology

The FWD testing procedure was originally designed around the early 1970s and has remained largely unchanged since that time. The original motivation was to mimic the forces exerted on the pavement by typical traffic loads. Consequently, progressive development of the FWD has

culminated in a load pulse that impacts the pavement for a similar duration as a truck tire, which primarily excites a single frequency. This quality is well known, and numerous analyses that have been performed wherein the FWD load is approximated as exciting one frequency [86, 89–94]. However, the ultimate goal of FWD testing and analysis is not to replicate traffic loads, but rather to determine the *in situ* material properties of the pavement [95]. Therefore, designing the FWD load to mimic traffic is not necessarily the best approach to extract information from the structure, because traffic loads excite a very narrow range of frequencies.

Since the FWD's introduction in the United States, numerous researchers have investigated the range of frequencies excited by the impact load. In an early study, Sebaaly *et al.* [96] observed the excited frequencies span 0 to 45.5 Hz. Later, Kim *et al.* [97] developed an ANN method for FWD backcalculation; when testing their method's backcalculation performance, they identified 17 Hz as the dominant frequency in backcalculation. Chatti and Lei [98] developed a forward calculation model and concluded that 10-25 Hz as the range of frequencies relevant in the pavement response to an FWD impact. Applying the fast Fourier transform to a synthetic haversine signal that resembles a typical FWD load, Zhao *et al.* [99] found that frequencies beyond 250 Hz are negligibly excited.

Recently, researchers have observed that the backcalculation analysis is highly sensitive to the range of frequencies excited by the FWD. Madsen and Levenberg [26] found that the backcalculated parameters are sensitive to characteristics of the FWD pulse, noting that new constitutive information is revealed under different loadings. Bazi and Assi [100] observed that the best backcalculation matching occurs around 17 Hz, and noted their method was not sensitive to very low frequencies (*e.g.*, below 0.1 Hz). In a recent study, Fu *et al.* [101] rigorously investigated the range of frequencies that are considered in backcalculation analysis. Denoting the phenomenon as the effective frequency range (EFR), they simulated several backcalculations of the same model with different seed moduli (*i.e.*, initial guesses) and identified the EFR from the overlap of the dynamic modulus curve solutions. In their analysis, they found that the EFR typically spans 5 to 65 Hz.

As mentioned in Section 2.1.3, ill-posed optimization is another pervasive issue in modern FWD backcalculation practice [19]. In FWD backcalculation, the analysis is ill-posed when the number of deflections sensor time histories is less than the number of pavement layer moduli parameters being optimized. Ill-posed problem structures are well known to introduce a myriad of undesirable solutions to the optimization space, which considerably reduces the chance of backcalculating accu-

rate layer moduli. Despite its significance, ill-posedness has seen little investigation in the context of FWD backcalculation over the years. Perhaps the earliest to mention the effects of ill-posed backcalculation are Davies and Mamlouk [102]. In a review of nondestructive pavement evaluation techniques, they explained backcalculation issues arise due to limited amount of measurements from FWD testing, which makes identification of a correct solution difficult. Since then, a handful of researchers such as Turkiyyah [103] have become aware of the issue and added considerations for ill-posedness in their developed methods. However, investigations into inverse and ill-posed problems is ongoing in numerous engineering fields [68], and no generally effective solution methods have been discovered thus far.

In a review of early nondestructive pavement testing methods, Moore *et al.* [10] noted that impact loads should have durations of less than 1 ms to excite a sufficient range of frequencies in the pavement. However, modern FWD devices typically have pulse durations ranging approximately between 20 and 35 ms [104]. Furthermore, as pavement models become more advanced, they increase the number of parameters in the optimization. Only seven or nine sensors are typically used in contemporary FWD practice [6]; however, modern pavement models can easily require more than nine variables in the backcalculation. Thus, a significant discrepancy is evident between the optimal FWD testing procedure and that which is being used in practice.

Chapter 3

UGA-PAVE Development

In this chapter, the theoretical details of the methods used to develop UGA-PAVE are outlined. UGA-PAVE is a dynamic FWD backcalculation technique comprising state-of-the-art computational methods for the forward model (which simulates the FWD impact response physics) and the optimization routine (which estimates the pavement layer moduli). For the forward model, UGA-PAVE employs the ViscoWave algorithm devised by Lee [7, 25, 60]. For the optimization, it uses a novel tandem trust-region technique, which combines both the STIR and LMA methods into a hybrid scheme.

3.1 Forward Model

The computational algorithm ViscoWave, developed by Lee [7], is used to solve the forward problem (*i.e.*, calculate displacements resulting from an input force and set of pavement layer moduli). The algorithm is a finite layer technique that models the pavement section axisymmetrically and incorporates spectral element theory to describe the wave motions through each layer.

3.1.1 Wave Equations for Linearly Elastic Materials

The generalized equations of motion for a continuum body are derived from the balance of linear momentum

$$\nabla \cdot \boldsymbol{\sigma} + \boldsymbol{b} = \rho \ddot{\boldsymbol{u}}, \tag{3.1}$$

where ∇ is the vector gradient operator, $\boldsymbol{\sigma}$ is the stress tensor, $\cdot$ is the dot product operator, $\boldsymbol{b}$ is the vector of body forces per unit volume, ρ is the mass density of the body, $\boldsymbol{u}$ is the displacement vector, and $\ddot{\circ}$ denotes the second time derivative. The stress-strain relationship of homogeneous, isotropic, linearly elastic materials is defined using Hooke's Law:

$$\boldsymbol{\sigma} = \lambda \, \mathrm{tr}(\boldsymbol{\epsilon})\boldsymbol{I} + 2\mu\boldsymbol{\epsilon}, \tag{3.2}$$

where $\boldsymbol{\epsilon}$ is the strain tensor, $\boldsymbol{I}$ is the identity tensor, and λ and μ are the Lamé moduli, defined as

$$\lambda = \frac{\nu E}{(1+\nu)(1-2\nu)}, \qquad \mu = \frac{E}{2(1+\nu)}, \tag{3.3}$$

where ν is Poisson's ratio and E is Young's modulus. The strain-displacement relationship is derived from continuum mechanics as

$$\boldsymbol{\epsilon} = \frac{1}{2}[\nabla\boldsymbol{u} + (\nabla\boldsymbol{u})^T]. \tag{3.4}$$

The equations of motion are then found by substituting Eqs. (3.2) and (3.4) into Eq. (3.1), yielding

$$(\lambda+\mu)\nabla(\nabla\cdot\boldsymbol{u}) + \mu\nabla^2\boldsymbol{u} = \rho\ddot{\boldsymbol{u}}. \tag{3.5}$$

Using Helmholtz decomposition, the displacement of the material can be expressed as

$$\boldsymbol{u} = \nabla\varphi + \nabla\times\boldsymbol{\psi}, \tag{3.6}$$

where φ is a scalar potential representing the translational component of $\boldsymbol{u}$, $\boldsymbol{\psi}$ is a vector potential representing the rotational component of $\boldsymbol{u}$, and $\times$ is the cross-product operator.

By employing an axisymmetric model, important simplifications can be made. Because the model is in cylindrical coordinates, the displacement vector can be decomposed into radial (r), circumferential (θ), and vertical (z) components: u, v, and w, respectively. Similarly, the rotational potential vector of $\boldsymbol{u}$ can also decomposed into three scalar components: ψ_r, ψ_θ, and ψ_z. Due to axisymmetry, the circumferential components of $\boldsymbol{u}$ and $\nabla\varphi$ as well as the radial and vertical

components of $\boldsymbol{\psi}$ become zero (*i.e.*, $v = \frac{\partial \varphi}{\partial \theta} = \psi_r = \psi_z = 0$). Applying these conditions to Eq. (3.6) gives

$$u = \frac{\partial \varphi}{\partial r} - \frac{\partial \psi_\theta}{\partial z}, \tag{3.7a}$$

$$w = \frac{\partial \varphi}{\partial z} + \frac{1}{r}\psi_\theta + \frac{\partial \psi_\theta}{\partial r}. \tag{3.7b}$$

Substituting Eqs. (3.7) into Eq. (3.5) yields the wave equations for the axisymmetric medium

$$\frac{\partial^2 \varphi}{\partial r^2} + \frac{1}{r}\frac{\partial \varphi}{\partial r} + \frac{\partial^2 \varphi}{\partial z^2} = \frac{1}{c_P^2}\ddot{\varphi}, \tag{3.8a}$$

$$\frac{\partial^2 \psi_\theta}{\partial r^2} + \frac{1}{r}\frac{\partial \psi_\theta}{\partial r} + \frac{\partial^2 \psi_\theta}{\partial z^2} - \frac{1}{r^2}\psi_\theta = \frac{1}{c_S^2}\ddot{\psi}_\theta. \tag{3.8b}$$

where c_P and c_S are the speeds of sound of the compression (P) and shear (S) waves defined as

$$c_P = \sqrt{\frac{\lambda + 2\mu}{\rho}}, \qquad c_S = \sqrt{\frac{\mu}{\rho}}. \tag{3.9}$$

3.1.2 Wave Equations for Viscoelastic Materials

3.1.2.1 Derivation of Equations of Motion

Viscoelastic materials are defined as those whose properties are time-dependent; therefore, their stresses, strains, and Lamé moduli must be defined as functions of time. Due to this, for linearly viscoelastic materials [7], the stress-strain relationship takes the form

$$\boldsymbol{\sigma} = \lambda * \mathrm{tr}(\boldsymbol{\epsilon})\boldsymbol{I} + 2\mu * \boldsymbol{\epsilon}, \tag{3.10}$$

where the $*$ operator denotes the the Stieltjes convolution integral

$$F * G = \int_0^t F(t-\tau)\frac{\partial G(\tau)}{\partial \tau} d\tau. \tag{3.11}$$

The equations of motion are found by substituting Eqs. (3.10) and (3.4) into Eq. (3.1), giving

$$(\lambda + \mu) * \nabla(\nabla \cdot \boldsymbol{u}) + \mu * \nabla^2 \boldsymbol{u} = \rho \ddot{\boldsymbol{u}}. \tag{3.12}$$

Applying Eq. (3.6) and axisymmetry again yields the linear, viscoelastic wave equations

$$(\lambda + 2\mu) * \nabla^2 \varphi \equiv (\lambda + 2\mu) * \left[\frac{\partial^2 \varphi}{\partial r^2} + \frac{1}{r} \frac{\partial \varphi}{\partial r} + \frac{\partial^2 \varphi}{\partial z^2} \right] = \rho \ddot{\varphi}, \tag{3.13a}$$

$$\mu * \left[\nabla^2 \psi_\theta - \frac{\psi_\theta}{r^2} \right] \equiv \mu * \left[\frac{\partial^2 \psi_\theta}{\partial r^2} + \frac{1}{r} \frac{\partial \psi_\theta}{\partial r} + \frac{\partial^2 \psi_\theta}{\partial z^2} - \frac{\psi_\theta}{r^2} \right] = \rho \ddot{\psi}_\theta, \tag{3.13b}$$

where Eqs. (3.13a) and (3.13b) represent the compression and shear waves through the medium, respectively. It becomes convenient to simplify the shear wave equation by relating the circumferential component of the rotational vector potential, ψ_θ, to a scalar potential, γ, as

$$\psi_\theta = -\frac{\partial \gamma}{\partial r}. \tag{3.14}$$

By employing Eq. (3.14), the equation of shear wave motion in Eq. (3.13b) becomes

$$\mu * \nabla^2 \gamma = \mu * \left[\frac{\partial^2 \gamma}{\partial r^2} + \frac{1}{r} \frac{\partial \gamma}{\partial r} + \frac{\partial^2 \gamma}{\partial z^2} \right] = \rho \ddot{\gamma}, \tag{3.15}$$

and the radial and vertical components of displacement in Eqs. (3.7a) and (3.7b) are now

$$u = \frac{\partial \varphi}{\partial r} + \frac{\partial^2 \gamma}{\partial r \partial z}, \tag{3.16a}$$

$$w = \frac{\partial \varphi}{\partial z} - \frac{\partial^2 \gamma}{\partial r^2} - \frac{1}{r} \frac{\partial \gamma}{\partial r}. \tag{3.16b}$$

3.1.2.2 Solutions to Equations of Motion

Solving Eqs. (3.13a) and (3.15) can be made practical by use of the Laplace and Hankel transforms. First, the Laplace transform, defined as $\mathcal{L}\{f(t)\} = \hat{f}(s) = \int_0^\infty f(t)e^{-st}\ dt$, is applied to obtain

$$(\hat{\lambda} + 2\hat{\mu}) \cdot \Big[\frac{\partial^2 \hat{\varphi}}{\partial r^2} + \frac{1}{r}\frac{\partial \hat{\varphi}}{\partial r} + \frac{\partial^2 \hat{\varphi}}{\partial z^2}\Big] = s\rho\hat{\varphi}, \tag{3.17a}$$

$$\hat{\mu} \cdot \Big[\frac{\partial^2 \hat{\gamma}}{\partial r^2} + \frac{1}{r}\frac{\partial \hat{\gamma}}{\partial r} + \frac{\partial^2 \hat{\gamma}}{\partial z^2}\Big] = s\rho\hat{\gamma}, \tag{3.17b}$$

for the compression and shear equations, respectively, where s is the complex Laplace domain variable and $\hat{\circ}$ denotes an entity that has been transformed to the Laplace domain. Next, the ν^{th}-order Hankel transform, defined as $\mathcal{H}_\nu\{\hat{f}(r)\} = \bar{f}_\nu(k) = \int_0^\infty r\hat{f}(r)J_\nu(kr)\ dr$, is applied to Eqs. (3.17a) and (3.17b). Henceforth, Hankel-transformed entities of order zero (*i.e.*, $\bar{f}_0(k)$) will have their subscripts dropped for convenience. Using the identity $\int_0^\infty r\Big(\frac{d^2\hat{f}}{dr^2} + \frac{1}{r}\frac{d\hat{f}}{dr} - \frac{\nu^2}{r^2}\hat{f}\Big)J_\nu(kr)\ dr = -k^2\bar{f}_\nu(k)$ [105] and rearranging, the wave equations in the Laplace-Hankel domain become

$$\frac{\partial^2 \bar{\varphi}}{\partial z^2} - \Big(k^2 + \frac{s}{\hat{c}_P^2}\Big)\bar{\varphi} = 0, \tag{3.18a}$$

$$\frac{\partial^2 \bar{\gamma}}{\partial z^2} - \Big(k^2 + \frac{s}{\hat{c}_S^2}\Big)\bar{\gamma} = 0, \tag{3.18b}$$

where J_ν is the ν^{th}-order Bessel function of the first kind, k is the Hankel domain variable, $\bar{\circ}$ denotes a Hankel-transformed entity, and

$$\hat{c}_P = \sqrt{\frac{\hat{\lambda} + 2\hat{\mu}}{\rho}}, \qquad \hat{c}_S = \sqrt{\frac{\hat{\mu}}{\rho}}. \tag{3.19}$$

The solutions to Eqs. (3.18a) and (3.18b) are the waves that propagate in the r (compression) and z (shear) directions, respectively, and they take the form

$$\bar{\varphi} = A_1 e^{-z\bar{p}}, \tag{3.20a}$$

$$\bar{\gamma} = B_1 e^{-z\bar{q}}, \tag{3.20b}$$

where A_1 and B_1 are arbitrary constants determined from boundary conditions and

$$\bar{p} = \sqrt{k^2 + \frac{s}{\hat{c}_P^2}}, \qquad \bar{q} = \sqrt{k^2 + \frac{s}{\hat{c}_S^2}}. \tag{3.21}$$

3.1.2.3 Expressions for Stress and Displacement in Laplace-Hankel Domain

To make use of the solutions in Eqs. (3.20a) and (3.20b), the displacements and stresses must be determined and likewise transformed into the Laplace-Hankel domain. When applying the Laplace and Hankel transforms to the displacements and stresses, special care must be given to the Hankel transform in particular due to the axisymmetry condition. Points along the z-axis are only allowed to displace in the z-direction and cannot move in the r-direction. Thus, when the point at $r = z = 0$ is subjected to a load, the displacements at the point must begin with $u = 0$ and $w \neq 0$. This condition requires that Bessel functions of different orders must be used in the Hankel transforms for the stress and displacements depending on the directions they act. As demonstrated in Fig. 3.1, the zeroth order Bessel function has a nonzero value ($J_0(0) \neq 0$) at the origin, and is best used to describe the stress and displacement in the z-direction, σ_{zz} and w. Similarly, the first order Bessel function is zero ($J_1(0) = 0$) at the origin, which is more akin to the stress and displacement in the r-direction, σ_{zr} and u.

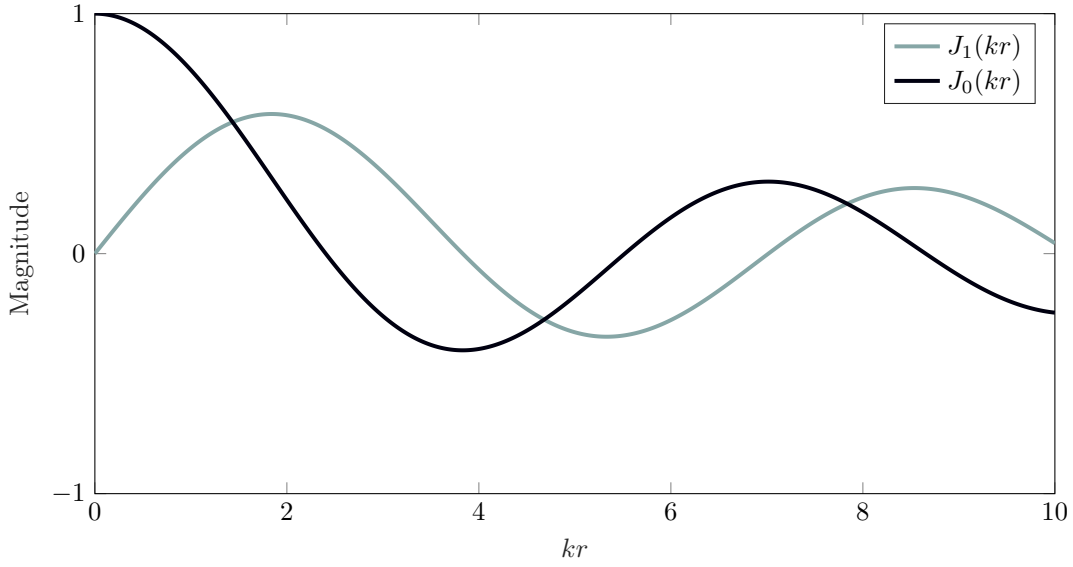

Figure 3.1. Bessel functions of the zeroth and first kinds.

Before obtaining the displacements in the transformed domain, it is useful to note two Bessel function identities. The first is that which was used to obtain Eqs. (3.18a) and (3.18b). The second identity relates the zeroth-order Hankel transform of a function to the first-order transform of its derivative [7], $\mathcal{H}_1\Big\{\frac{\partial \hat{f}(r)}{\partial r}\Big\} = -k \cdot \mathcal{H}_0\{\hat{f}(r)\} \equiv -k\bar{f}(k)$. Now, the displacements in Eqs. (3.16) can be transformed into the Laplace-Hankel domain, giving

$$\begin{aligned}
\mathcal{H}_1\{\mathcal{L}\{u\}\} &= \mathcal{H}_1\{\ \mathcal{L}\Big\{\frac{\partial \varphi}{\partial r} + \frac{\partial^2 \gamma}{\partial r \partial z}\Big\}\ \}, \\
&= \mathcal{H}_1\Big\{\frac{\partial \hat{\varphi}}{\partial r} + \frac{\partial^2 \hat{\gamma}}{\partial r \partial z}\Big\} \equiv -k \cdot \mathcal{H}_0\Big\{\frac{\partial \hat{\varphi}}{\partial r} + \frac{\partial^2 \hat{\gamma}}{\partial r \partial z}\Big\}, \\
\bar{u} &= -k\bar{\varphi} - k\frac{\partial \bar{\gamma}}{\partial z}; \qquad (3.22a)
\end{aligned}$$

$$\begin{aligned}
\mathcal{H}_0\{\mathcal{L}\{w\}\} &= \mathcal{H}_0\{\ \mathcal{L}\Big\{\frac{\partial \varphi}{\partial z} - \frac{\partial^2 \gamma}{\partial r^2} - \frac{1}{r}\frac{\partial \gamma}{\partial r}\Big\}\ \}, \\
&= \mathcal{H}_0\Big\{\frac{\partial \hat{\varphi}}{\partial z} - \frac{\partial \hat{\gamma}^2}{\partial r^2} - \frac{1}{r}\frac{\partial \hat{\gamma}}{\partial r}\Big\}, \\
\bar{w} &= \frac{\partial \bar{\varphi}}{\partial z} + k^2\bar{\gamma}. \qquad (3.22b)
\end{aligned}$$

Inserting Eqs. (3.4) and (3.16) into (3.10) yields expressions for the viscoelastic stresses in the r and z directions, respectively, due to a vertical loading,

$$\sigma_{zr} = \mu * \frac{\partial}{\partial r}\Big[2\frac{\partial \varphi}{\partial z} - \frac{\partial^2 \gamma}{\partial r^2} - \frac{1}{r}\frac{\partial \gamma}{\partial r} + \frac{\partial^2 \gamma}{\partial z^2}\Big], \qquad (3.23a)$$

$$\sigma_{zz} = \lambda * \Big[\frac{\partial^2 \varphi}{\partial r^2} + \frac{1}{r}\frac{\partial \varphi}{\partial r} + \frac{\partial^2 \varphi}{\partial z^2}\Big] + 2\mu * \frac{\partial}{\partial z}\Big[\frac{\partial \varphi}{\partial z} - \frac{1}{r}\frac{\partial \gamma}{\partial r} - \frac{\partial^2 \gamma}{\partial r^2}\Big]. \qquad (3.23b)$$

Using the same Bessel identities for transforming the displacements, the stresses in the Laplace-Hankel domain can then be determined as

$$\begin{aligned}
\mathcal{H}_1\{\mathcal{L}\{\sigma_{zr}\}\} &= \mathcal{H}_1\{\mathcal{L}\Big\{\mu * \frac{\partial}{\partial r}\Big[2\frac{\partial \varphi}{\partial z} - \frac{\partial^2 \gamma}{\partial r^2} - \frac{1}{r}\frac{\partial \gamma}{\partial r} + \frac{\partial^2 \gamma}{\partial z^2}\Big]\Big\}\}, \\
&= \mathcal{H}_1\Big\{s\hat{\mu}\frac{\partial}{\partial r}\Big[2\frac{\partial \hat{\varphi}}{\partial z} - \frac{\partial^2 \hat{\gamma}}{\partial r^2} - \frac{1}{r}\frac{\partial \hat{\gamma}}{\partial r} + \frac{\partial^2 \hat{\gamma}}{\partial z^2}\Big]\Big\}, \\
&= -sk\hat{\mu}\cdot\mathcal{H}_0\Big\{2\frac{\partial \hat{\varphi}}{\partial z} - \frac{\partial^2 \hat{\gamma}}{\partial r^2} - \frac{1}{r}\frac{\partial \hat{\gamma}}{\partial r} + \frac{\partial^2 \hat{\gamma}}{\partial z^2}\Big\}, \\
&= -sk\hat{\mu}\Big[2\frac{\partial \bar{\varphi}}{\partial z} + 2\frac{\partial^2 \bar{\gamma}}{\partial z^2} - \frac{s}{\hat{c}_S^2}\bar{\gamma}\Big] \\
\bar{\sigma}_{zr} &= -sk\hat{\mu}\Big[2\frac{\partial \bar{\varphi}}{\partial z} + \Big(k^2 + \bar{q}^2\Big)\bar{\gamma}\Big];
\end{aligned} \tag{3.24a}$$

$$\begin{aligned}
\mathcal{H}_0\{\mathcal{L}\{\sigma_{zz}\}\} &= \mathcal{H}_0\{\mathcal{L}\Big\{\lambda * \Big[\frac{\partial^2 \varphi}{\partial r^2} + \frac{1}{r}\frac{\partial \varphi}{\partial r} + \frac{\partial^2 \varphi}{\partial z^2}\Big] + 2\mu * \frac{\partial}{\partial z}\Big[\frac{\partial \varphi}{\partial z} - \frac{\partial^2 \gamma}{\partial r^2} - \frac{1}{r}\frac{\partial \gamma}{\partial r}\Big]\Big\}\}, \\
&= \mathcal{H}_0\Big\{s\hat{\lambda}\Big[\frac{\partial^2 \hat{\varphi}}{\partial r^2} + \frac{1}{r}\frac{\partial \hat{\varphi}}{\partial r} + \frac{\partial^2 \hat{\varphi}}{\partial z^2}\Big] + 2s\hat{\mu}\frac{\partial}{\partial z}\Big[\frac{\partial \hat{\varphi}}{\partial z} - \frac{\partial^2 \hat{\gamma}}{\partial r^2} - \frac{1}{r}\frac{\partial \hat{\gamma}}{\partial r}\Big]\Big\}, \\
&= s\hat{\lambda}\Big[\frac{\partial^2 \bar{\varphi}}{\partial z^2} - k^2\bar{\varphi}\Big] + 2s\hat{\mu}\Big[\frac{\partial^2 \bar{\varphi}}{\partial z^2} + k^2\frac{\partial \bar{\gamma}}{\partial z}\Big], \\
&= \hat{\mu}\frac{s^2}{\hat{c}_S^2}\bar{\varphi} + 2sk^2\hat{\mu}\Big[\bar{\varphi} + \frac{\partial \bar{\gamma}}{\partial z}\Big], \\
\bar{\sigma}_{zz} &= s\hat{\mu}\Big(k^2 + \bar{q}^2\Big)\bar{\varphi} + 2sk^2\hat{\mu}\frac{\partial \bar{\gamma}}{\partial z}.
\end{aligned} \tag{3.24b}$$

Note the relationships from Eqs. (3.18a) and (3.18b) were employed to simplify the expressions. Similarly, applying the Laplace and Hankel transforms to the displacements in Eqs. (3.16a) and (3.16b) yields

$$\bar{u} = -k\bar{\varphi} - k\frac{\partial \bar{\gamma}}{\partial z}, \tag{3.25a}$$

$$\bar{w} = k^2\bar{\gamma} + \frac{\partial \bar{\varphi}}{\partial z}. \tag{3.25b}$$

Due to the nature of the loading, the Hankel transforms of orders one and zero were used to convert the radial and vertical displacements, respectively. In FWD experimentation, a vertical impulse load is applied instantaneously at time $t = 0$ and at location $r = 0$, after which the system is unloaded for $t > 0$. This means that $w(t = 0) \neq 0$, whereas $u(t = 0) = 0$. Similarly, the first-order Bessel function, J_1, begins at a nonzero value, whereas the zeroth-order Bessel function, J_0, begins at zero.

3.1.3 Layer Stiffness Matrices

Here, the finite layer method (FLM) is used to construct the forward models of the pavement for FWD backcalculation based on the stresses and displacements from Eqs. (3.24) and (3.25). The finite element method has been the most popular choice for modeling the forward problem since the inception of FWD backcalculation; however, approaches based on the spectral element method (SEM) [51–54] are significantly more computationally efficient for modeling wave propagation in layered structures. The computational benefits are attributed to two features: (1) SEM can always calculate the solution in the frequency domain (via the Fourier transform) instead of the time domain, and (2) SEM only requires one element to sufficiently represent each material layer. The FLM is effectively the same as SEM, except the solution is calculated in the Laplace-Hankel domain instead of the Fourier domain.

The finite-layer elements from Lee's [7,60] ViscoWave algorithm are formulated here. Two types of elements used in FLM: a two-node element with a finite thickness and a single-node element with a semi-infinite thickness. The individual stiffness matrices for both element types are derived in the following sections. To model a pavement in FLM, one element should be used to represent each material layer, and the individual stiffness matrices can be linked together using the same procedure as used in FEM.

3.1.3.1 Finite-Layer Element

An axisymmetric finite-layer element (*i.e.*, with a finite thickness) can be imagined as the rectangular cross-section of a cylinder with infinite radius. It consists of two nodes—one each on its top and bottom surfaces. Both nodes comprise one radial and one vertical degree of freedom (DOF), where the vertical DOFs are defined with positive direction oriented downward (in the direction the ver-

tical waves propagate from the impact load). The response at any location within the element can be calculated via superposition of the incident waves (introduced by the load) and reflected waves (induced by the top/bottom element boundaries) traveling through the element. This response can be dissected into a compression wave traveling at speed c_P and a shear wave with speed c_S.

To account for the vertical waves reflecting off the bottom boundary, additional terms are added to Eqs. (3.20a) and (3.20b), giving

$$\bar{\varphi} = A_1 e^{-\bar{p}z} + A_2 e^{-\bar{p}(h-z)}, \tag{3.26a}$$

$$\bar{\gamma} = B_1 e^{-\bar{q}z} + B_2 e^{-\bar{q}(h-z)}, \tag{3.26b}$$

where h is the vertical thickness of the layer, and A_2 and B_2 are additional arbitrary constants determined from boundary conditions. Inserting Eq. (3.26a) into (3.25a) as well as (3.26b) into (3.25b) yields the radial and vertical displacement within the finite-layer element as

$$\bar{u} = -k\Big(A_1 e^{-\bar{p}z} + A_2 e^{-\bar{p}(h-z)}\Big) + k\bar{q}\Big(B_1 e^{-\bar{q}z} - B_2 e^{-\bar{q}(h-z)}\Big), \tag{3.27a}$$

$$\bar{w} = -\bar{p}\Big(A_1 e^{-\bar{p}z} - A_2 e^{-\bar{p}(h-z)}\Big) + k^2\Big(B_1 e^{-\bar{q}z} + B_2 e^{-\bar{q}(h-z)}\Big). \tag{3.27b}$$

Similarly, substituting the Laplace-Hankel transformed potentials into Eqs. (3.24a) and (3.24b) gives

$$\bar{\sigma}_{zr} = 2sk\bar{p}\hat{\mu}\Big(A_1 e^{-\bar{p}z} - A_2 e^{-\bar{p}(h-z)}\Big) - sk\hat{\mu}(k^2+\bar{q}^2)\Big(B_1 e^{-\bar{q}z} + B_2 e^{-\bar{q}(h-z)}\Big), \tag{3.28a}$$

$$\bar{\sigma}_{zz} = s\hat{\mu}(k^2+\bar{q}^2)\Big(A_1 e^{-\bar{p}z} + A_2 e^{-\bar{p}(h-z)}\Big) - 2sk^2\bar{q}\hat{\mu}\Big(B_1 e^{-\bar{q}z} - B_2 e^{-\bar{q}(h-z)}\Big). \tag{3.28b}$$

Now, Eqs. (3.27) and (3.28) are arranged into two systems of equations with a common vector of arbitrary constants. Both systems can be simplified by inserting two known conditions. The first is the top node (represented by subscript 1 below) exists at $z = 0$, and the second is the bottom node (denoted by subscript 2 below) lies on $z = h$. Inserting these two conditions into the two

systems of equations gives

$$\begin{Bmatrix} \bar{u}_1 \\ \bar{w}_1 \\ \bar{u}_2 \\ \bar{w}_2 \end{Bmatrix} = \begin{bmatrix} -k & -ke^{-\bar{p}h} & k\bar{q} & -k\bar{q}e^{-\bar{q}h} \\ -\bar{p} & \bar{p}e^{-\bar{p}h} & k^2 & k^2e^{-\bar{q}h} \\ -ke^{-\bar{p}h} & -k & k\bar{q}e^{-\bar{q}h} & -k\bar{q} \\ -\bar{p}e^{-\bar{p}h} & \bar{p} & k^2e^{-\bar{q}h} & k^2 \end{bmatrix} \begin{Bmatrix} A_1 \\ A_2 \\ B_1 \\ B_2 \end{Bmatrix},$$

$$\bar{\boldsymbol{U}} = \boldsymbol{Q_d A}; \tag{3.29}$$

$$\begin{Bmatrix} \bar{\sigma}_{zr,1} \\ \bar{\sigma}_{zz,1} \\ \bar{\sigma}_{zr,2} \\ \bar{\sigma}_{zz,2} \end{Bmatrix} = s\hat{\mu} \begin{bmatrix} 2k\bar{p} & -k\bar{p}e^{-\bar{p}h} & -k(k^2+\bar{q}^2) & -k(k^2+\bar{q}^2)e^{-\bar{q}h} \\ (k^2+\bar{q}^2) & (k^2+\bar{q}^2)e^{-\bar{p}h} & -2k^2\bar{q} & 2k^2\bar{q}e^{-\bar{q}h} \\ 2k\bar{p}e^{-\bar{p}h} & -2k\bar{p} & -k(k^2+\bar{q}^2)e^{-\bar{q}h} & -k(k^2+\bar{q}^2) \\ (k^2+\bar{q}^2)e^{-\bar{p}h} & (k^2+\bar{q}^2) & -2k^2\bar{q}e^{-\bar{q}h} & 2k^2\bar{q} \end{bmatrix} \begin{Bmatrix} A_1 \\ A_2 \\ B_1 \\ B_2 \end{Bmatrix},$$

$$\bar{\boldsymbol{S}} = s\hat{\mu}\boldsymbol{Q_s A}. \tag{3.30}$$

From the finite element method, the stiffness matrix of an element, $\boldsymbol{K}$, is the relationship between the displacements and surface tractions, defined by

$$\bar{\boldsymbol{T}} = \boldsymbol{K}\bar{\boldsymbol{U}}, \tag{3.31}$$

where $\bar{T}$ is the vector of surface tractions. The traction vector is from the Cauchy stress theorem and is obtained by multiplying the unit vector normal to each boundary of the element with the stress vector at that boundary. The tractions of the finite-layer element with positive z-direction oriented downward are

$$\begin{Bmatrix} \bar{T}_{r,1} \\ \bar{T}_{z,1} \\ \bar{T}_{r,2} \\ \bar{T}_{z,2} \end{Bmatrix} = \begin{bmatrix} -1 & 0 & 0 & 0 \\ 0 & -1 & 0 & 0 \\ 0 & 0 & 1 & 0 \\ 0 & 0 & 0 & 1 \end{bmatrix} \begin{Bmatrix} \bar{\sigma}_{zr,1} \\ \bar{\sigma}_{zz,1} \\ \bar{\sigma}_{zr,2} \\ \bar{\sigma}_{zz,2} \end{Bmatrix},$$

$$\bar{\boldsymbol{T}} = \boldsymbol{N_f}\bar{\boldsymbol{S}}. \tag{3.32}$$

Finally, the stiffness matrix for the finite-layer element, $\boldsymbol{K_f}$, is determined by combining Eqs. (3.29), (3.30), and (3.32) into (3.31), rearranging to eliminate $\boldsymbol{A}$, and post-multiplying by $\boldsymbol{Q_d^{-1}}$ to yield

$$\boldsymbol{K_f} = s\hat{\mu}\boldsymbol{N_f}\boldsymbol{Q_s}\boldsymbol{Q_d^{-1}}. \tag{3.33}$$

3.1.3.2 Semi-Infinite Element

Similar to the finite-thickness element, an axisymmetric element with a semi-infinite thickness is the rectangular cross-section of a half-space cylinder spanning infinite distance in the radial direction and extends semi-infinitely into the positive z-direction. Implementation of this element is useful for avoiding wave reflections that occur at the bottom surface of the model. Consequently, the element has only one node located on its top surface.

The displacements and stresses within the semi-infinite element can be determined with the same approach used for the finite-thickness element. Because wave reflections need not be considered, Eqs. (3.18a) and (3.18b) are sufficient for describing wave propagation within the element. Substituting them into Eqs. (3.25a) and (3.25b) yields the displacements for the semi-infinite element as

$$\bar{u} = -kA_1e^{-\bar{p}z} + k\bar{q}B_1e^{-\bar{q}z}, \tag{3.34a}$$

$$\bar{w} = -\bar{p}A_1e^{-\bar{p}z} + k^2B_1e^{-\bar{q}z}. \tag{3.34b}$$

Likewise, the stresses of the element are found by inserting Eqs. (3.18a) and (3.18b) into (3.24a) and (3.24b), giving

$$\bar{\sigma}_{zr} = 2sk\bar{p}\hat{\mu}A_1e^{-\bar{p}z} - sk(k^2+\bar{q}^2)\hat{\mu}B_1e^{-\bar{q}z}, \tag{3.35a}$$

$$\bar{\sigma}_{zz} = s(k^2+\bar{q}^2)\hat{\mu}A_1e^{-\bar{p}z} - 2sk^2\bar{q}\hat{\mu}B_1e^{-\bar{q}z}. \tag{3.35b}$$

When arranging the semi-infinite element's displacements and stresses into matrix form, only one node exists. Employing the same strategy as used for the finite-layer element yields

$$\begin{Bmatrix} \bar{u}_1 \\ \bar{w}_1 \end{Bmatrix} = \begin{bmatrix} -k & -k\bar{q} \\ -\bar{p} & k^2 \end{bmatrix} \begin{Bmatrix} A_1 \\ B_1 \end{Bmatrix},$$

$$\bar{\boldsymbol{U}} = \boldsymbol{Q_d A}; \tag{3.36}$$

$$\begin{Bmatrix} \bar{\sigma}_{zr,1} \\ \bar{\sigma}_{zz,1} \end{Bmatrix} = s\hat{\mu} \begin{bmatrix} 2k\bar{p} & -k(k^2+\bar{q}^2) \\ (k^2+\bar{q}^2) & -2k^2\bar{q} \end{bmatrix} \begin{Bmatrix} A_1 \\ B_1 \end{Bmatrix},$$

$$\bar{\boldsymbol{S}} = s\hat{\mu}\boldsymbol{Q_s A}. \tag{3.37}$$

The Cauchy stress theorem is applied once again to determine the surface tractions. With positive z-direction oriented downward, the surface tractions of the semi-infinite element are

$$\begin{Bmatrix} \bar{T}_{r,1} \\ \bar{T}_{z,1} \end{Bmatrix} = \begin{bmatrix} -1 & 0 \\ 0 & -1 \end{bmatrix} \begin{Bmatrix} \bar{\sigma}_{zr,1} \\ \bar{\sigma}_{zz,1} \end{Bmatrix},$$

$$\bar{\boldsymbol{T}} = -\bar{\boldsymbol{S}}. \tag{3.38}$$

Inserting Eqs. (3.36)–(3.38) into (3.31) and applying the same steps as for the previous element gives

$$\boldsymbol{K_s} = -s\hat{\mu}\boldsymbol{Q_s Q_d^{-1}}, \tag{3.39}$$

where $\boldsymbol{K_s}$ is the stiffness matrix for the semi-infinite element.

3.1.3.3 Laplace-Hankel Inversion

After the system response due to the FWD impulse load is calculated in the Laplace-Hankel domain using FLM, it must be converted back to the time domain. This is accomplished by applying the inverse Hankel transform followed by the inverse Laplace transform. For the purposes of FWD backcalculation, only the vertical displacements at the surface of the model are of interest; consequently, the inverse Hankel transform of order zero is used. The analytical expression for this

transform is

$$\hat{W}_j(r) = \int_0^\infty k\bar{W}_j(k)J_0(kr)\ dk, \tag{3.40}$$

where W_j is the vertical deflection of the model at the j^{th} surface location. Although the upper limit of the integration is infinity, it has been shown the solution converges well when integrating over only the first five roots of the derivative of the Bessel function used in the transform [7, 106, 107]. Because J_0 is used in Eq. (3.40) to transform the vertical displacements, the roots of its derivative J_1 are used to subdivide the integration, thereby becoming the finite series of integrals

$$\begin{aligned}\hat{W}_j(r) = &\int_{b_0}^{b_1} k\bar{W}_j(k)J_0(kr)\ dk + \int_{b_1}^{b_2} k\bar{W}_j(k)J_0(kr)\ dk \\ &+ \cdots + \int_{b_4}^{b_5} k\bar{W}_j(k)J_0(kr)\ dk,\end{aligned} \tag{3.41}$$

where b_n is the n^{th} root of J_1, and $b_0 = 0$. Each sub-integration can be numerically computed using 6-point Gaussian quadrature of the form

$$\int_{b_{n-1}}^{b_n} k\bar{W}_j(k)J_0(kr)\ dk = \frac{b_n - b_{n-1}}{2}\sum_{p=1}^{6} v_p\beta_p\bar{W}_j J_0(\beta_p), \tag{3.42}$$

where v_p is the weight of the p^{th} node, x_p, in the quadrature rule, and

$$\beta_p = \Big(\frac{b_n - b_{n-1}}{2}\Big)x_p + \Big(\frac{b_n + b_{n-1}}{2}\Big). \tag{3.43}$$

The closed-form inverse Laplace transform is given by

$$W_j(t) = \frac{1}{2\pi i}\int_B \hat{W}_j(s)e^{st}\ ds, \tag{3.44}$$

where $i = \sqrt{-1}$ is the imaginary constant. Herein, the inverse Laplace transform is solved numerically via Abate and Valko's [108] fixed Talbot algorithm (FTA), wherein the contour path, B, is defined as

$$s(\theta) = \alpha\theta\big(\cot(\theta) + i\ \big), \qquad -\pi < \theta < \pi, \tag{3.45}$$

where

$$\alpha = \frac{2M}{5t}. \tag{3.46}$$

Parameter α is introduced to control the numerical precision of the integration, which is accomplished by specifying the number of subdivisions of the contour path, M. Specifically, the value of M corresponds to the number of precision decimal places. By inserting Eq. (3.45) into (3.44), the analytical expression for the inverse Laplace transform becomes

$$W_j(t) = \frac{\alpha}{\pi} \int_0^{\pi} \Re\big[\hat{W}_j\big(s(\theta)\big) e^{s(\theta)t} \big(1 + i\xi(\theta)\big)\big] \, d\theta, \tag{3.47}$$

where $\Re[\circ]$ takes the real part of complex quantity $\circ$, and

$$\xi(\theta) = \theta - \cot(\theta) + \theta \cot^2(\theta). \tag{3.48}$$

Finally, Eq. (3.47) can be numerically approximated using trapezoidal rule as

$$W_j(t) = \frac{\alpha}{M} \left(\frac{1}{2} \hat{W}_j(\alpha) e^{\alpha t} + \sum_{q=1}^{M-1} \Re\Big[\hat{W}_j\Big(s(\theta_q)\Big) e^{s(\theta_q)t} \Big(1 + i\xi(\theta_q)\Big)\Big] \right), \tag{3.49}$$

where θ_q is the angle corresponding to the q^{th} subdivision of the contour path, given by

$$\theta_q = \frac{q\pi}{M}. \tag{3.50}$$

3.2 Optimization Algorithm

The optimization in FWD backcalculation is posed as a nonlinear least-squares minimization with the form

$$\min_{\boldsymbol{x}} f(\boldsymbol{x}) = ||\boldsymbol{F}(\boldsymbol{x}) - \boldsymbol{y}||^2 \equiv \boldsymbol{\epsilon}(\boldsymbol{x})^T \boldsymbol{\epsilon}(\boldsymbol{x}), \quad \boldsymbol{b}^L \leq \boldsymbol{x} \leq \boldsymbol{b}^U, \tag{3.51}$$

where $\boldsymbol{x}$ is the vector of n unknown parameters (*e.g.*, stiffness moduli), $\boldsymbol{y}$ is the concatenated vector of m time histories measured by the deflection sensors, $\boldsymbol{F}$ is vector of deflections predicted by the "forward model" of the pavement structure, $\boldsymbol{\epsilon}(\boldsymbol{x}) = \boldsymbol{F}(\boldsymbol{x}) - \boldsymbol{y}$ is the "residual errors" function, $f(\boldsymbol{x})$ is the sum of errors squared, $\boldsymbol{b}^L$ and $\boldsymbol{b}^U$ are the lower and upper bounds of $\boldsymbol{x}$, and $||\circ||$ denotes

the Euclidean norm. The values of $\boldsymbol{x}$ are adjusted such that the value of $f(\boldsymbol{x})$ decreases relative to the previous iteration. The process of changing $\boldsymbol{x}$ is called the *step calculation* and is defined as

$$\boldsymbol{x}_{k+1} = \boldsymbol{x}_k + \boldsymbol{p}_k, \tag{3.52}$$

where $\boldsymbol{x}_k$ is the set of values at the current iteration k, $\boldsymbol{x}_{k+1}$ is the subsequent iterate, and $\boldsymbol{p}_k$ is the *step vector*. A new step is calculated each iteration until no further decreases in $f(\boldsymbol{x})$ can be found, and the final parameters are the optimal solution, $\boldsymbol{x}^*$.

Trust-region (TR) methods solve nonlinear least-squares minimization problems by conducting a secondary optimization of the step vector from Eq. (3.52) during each iteration of the primary optimization from Eq. (3.51). In traditional TR methods, the step vector optimization is defined using a second-order Taylor series approximation of $f(\boldsymbol{x}_k + \boldsymbol{p}_k)$ with respect to $\boldsymbol{p}_k$ and the solution is confined to a trust-region. Thereby, the *step optimization* problem takes the form

$$\min_{\boldsymbol{p}_k} \phi(\boldsymbol{p}_k) = f(\boldsymbol{x}_k) + \boldsymbol{g}_k^T \boldsymbol{p}_k + \frac{1}{2} \boldsymbol{p}_k^T \boldsymbol{H}_k \boldsymbol{p}_k, \quad ||\boldsymbol{p}_k|| \leq \Delta_k, \tag{3.53}$$

where $\boldsymbol{g}_k$ and $\boldsymbol{H}_k$ are the gradient and Hessian of $f(\boldsymbol{x}_k)$. The constraint, $||\boldsymbol{p}_k|| \leq \Delta_k$, is an n-dimensional sphere of radius Δ_k. The term "trust-region" refers to this hypersphere, and the inequality constraint restricts the step vector, $\boldsymbol{p}_k$, to exist on or within the region.

The calculations for $\boldsymbol{g}_k$ and $\boldsymbol{H}_k$ rely on computing the partial derivatives of $\boldsymbol{\epsilon}_k$ with respect to $\boldsymbol{x}_k$, which are not available in closed form for FWD backcalculation models; apropos, the forward finite difference approximation is used to compute the derivatives. In least-squares minimization problems, the gradient can be calculated by

$$\boldsymbol{g}_k = 2\boldsymbol{J}_k \boldsymbol{\epsilon}_k, \tag{3.54}$$

where $\boldsymbol{\epsilon}_k$ is shorthand for $\boldsymbol{\epsilon}(\boldsymbol{x}_k)$, and $\boldsymbol{J}_k = [\frac{\partial \boldsymbol{\epsilon}_k}{\partial x_1} \ \frac{\partial \boldsymbol{\epsilon}_k}{\partial x_2} \ ... \ \frac{\partial \boldsymbol{\epsilon}_k}{\partial x_n}]$ is the Jacobian of $\boldsymbol{\epsilon}_k$ [109]. Furthermore, the Hessian can be defined as

$$\boldsymbol{H}_k = 2\boldsymbol{J}_k^T \boldsymbol{J}_k + 2\boldsymbol{\epsilon}_k^T \nabla^2 \boldsymbol{\epsilon}_k, \tag{3.55}$$

where $\nabla^2 \boldsymbol{\epsilon}_k$ is the vector-wise Laplacian of the residuals. The residuals become increasingly small as the optimization proceeds; thus, it is common to drop the second term in Eq. (3.55) and approximate the Hessian as

$$\boldsymbol{H}_k \approx 2\boldsymbol{J}_k^T \boldsymbol{J}_k. \tag{3.56}$$

This approximation considerably reduces each iteration's computational expense at the cost of increased error when the omitted term is significant—such as in early iterations when values of $\boldsymbol{\epsilon}_k$ are largest, or in highly nonlinear regions with large $\nabla^2 \boldsymbol{\epsilon}_k$.

3.2.1 Tandem Trust-Region Method

The tandem trust-region method is a hybrid technique which uses two robust nonlinear least-squares solvers simultaneously to minimize Eq. (3.51). The first solver chosen is the subspace trust-region interior reflective (STIR) method developed by Branch *et al.* [1], and the second is a Levenberg-Marquardt algorithm (LMA) based on Bellavia and Riccietti's [2] method. The tandem approach is inspired by the observation that each method outperforms the other in different situations; by using them simultaneously, the strengths of one can be used to mitigate the other's weaknesses. The increased computational expense of conducting a second optimization is dwarfed by the cost of the numerical derivatives, which must be calculated when using only one optimizer.

Each iteration, two step vector solutions are computed via STIR and LMA, and the $\boldsymbol{p}_k$ producing a lower value of $f(\boldsymbol{x}_{k+1})$ is taken as the "trial iterate". After the superior $\boldsymbol{p}_k$ is determined, its minimization effectiveness is evaluated and used to update the trust-region for the next iteration. The key difference between the two optimizers lies in how the step calculation is performed. The STIR method solves for $\boldsymbol{p}_k$ using a second-order model based on $\boldsymbol{g}_k$ and $\boldsymbol{H}_k$, whereas the LMA uses a first-order model based on $\boldsymbol{J}_k$. Because STIR employs a higher-ordered model, it tends to take more accurate steps in general compared to its counterpart; however in models where the Hessian is approximated as in Eq. (3.56), the STIR's step calculation becomes prone to errors when the excluded nonlinear term (*i.e.*, $2\boldsymbol{\epsilon}_k^T \nabla^2 \boldsymbol{\epsilon}_k$) is non-negligible. In such cases, the LMA's step calculation tends to be superior because it circumvents the need to approximate the second-order derivatives while maintaining a higher degree of accuracy than the first-order Newton-based approximation.

Thus, the tandem trust-region method seeks to improve the trust-region approach as a whole by using the best aspects of its two components to cover the other's weaknesses.

A comprehensive outline of the TTR algorithm is provided in Fig. 3.2, and the remainder of this section explains the calculations performed in every iteration of the method. In Section 3.2.2, the tandem step solvers, STIR and LMA, are described. Then, a procedure of step refinements is discussed in Section 3.2.3. Finally, the process of updating the trust-region radius between iterations, $\Delta_k \rightarrow \Delta_{k+1}$, is provided in Section 3.2.4.

3.2.2 Step Optimization Solvers

3.2.2.1 STIR Method

Branch *et al.*'s [1] subspace trust-region interior reflective method begins by posing the step optimization problem in an "affine-scaled" space as

$$\min_{\bar{\boldsymbol{p}}_k} \bar{\phi}(\bar{\boldsymbol{p}}_k) = f(\boldsymbol{x}_k) + \bar{\boldsymbol{g}}_k^T \bar{\boldsymbol{p}}_k + \frac{1}{2} \bar{\boldsymbol{p}}_k^T \bar{\boldsymbol{H}}_k \bar{\boldsymbol{p}}_k, \quad ||\bar{\boldsymbol{p}}_k|| \leq \Delta_k, \tag{3.57}$$

where $\bar{\boldsymbol{g}}_k = \boldsymbol{D}_k \boldsymbol{g}_k$, $\bar{\boldsymbol{H}}_k = \boldsymbol{D}_k(\boldsymbol{H}_k + \boldsymbol{C}_k)\boldsymbol{D}_k$, and $\bar{\boldsymbol{p}}_k = \boldsymbol{D}_k^{-1}\boldsymbol{p}_k$. The matrices $\boldsymbol{D}_k$ and $\boldsymbol{C}_k$ come from Coleman and Li's [4, 110] affine-scaling transformation, which introduces the bound constraints, $\boldsymbol{b}^L$ and $\boldsymbol{b}^U$, into the step calculation. The first affine-scaling matrix, $\boldsymbol{D}_k$, applies weights to each parameter in $\boldsymbol{x}_k$ depending on how far it is from its upper and lower bounds. Hence, calculating $\boldsymbol{D}_k$ requires first computing the boundary-distance vector, $\boldsymbol{\sigma}(\boldsymbol{x}_k)$, whose i^{th} element is defined by

$$\sigma_i = \begin{cases} x_i - b_i^L, & g_i \geq 0 \ \& \ b_i^L > -\infty; \\ 1, & g_i \geq 0 \ \& \ b_i^L = -\infty; \\ b_i^U - x_i, & g_i < 0 \ \& \ b_i^U < \infty; \\ -1, & g_i < 0 \ \& \ b_i^U = \infty. \end{cases} \tag{3.58}$$

For a completely unbounded optimization, $\boldsymbol{D}_k$ is equal to identity, leaving $\boldsymbol{x}_k$ unchanged after the affine-scaling transformation. The first affine-scaling matrix is then calculated via

$$\boldsymbol{D}_k = \text{diag}\Big(|\boldsymbol{\sigma}_k|^{1/2}\Big), \tag{3.59}$$

Tandem Trust-Region Algorithm
Given $\boldsymbol{y},\ \boldsymbol{F},\ \boldsymbol{x}_0,\ \Delta_0,\ \boldsymbol{b}^L,\ \boldsymbol{b}^U,\ \varepsilon_p,\ \varepsilon_f$, and $k_{\max}$

FOR $k = 1,\ 2,\ \ldots,\ k_{\max}$

1. Calculate $f(\boldsymbol{x}_k),\ \boldsymbol{J}_k,\ \boldsymbol{g}_k,\ \boldsymbol{H}_k,\ \boldsymbol{D}_k,\ \boldsymbol{C}_k,\ \boldsymbol{S}_k$, and $\boldsymbol{W}_k$.

2. Calculate STIR trial step via:

2.1. Solve Eq. (3.61) for $\hat{\boldsymbol{p}}_k$ using Cholesky factorization algorithm, and determine the step vector using $\boldsymbol{p}_k = \boldsymbol{D}_k \boldsymbol{S}_k \hat{\boldsymbol{p}}_k$.

2.2. Conduct line search from Eq. (3.78) to determine the scaling coefficient, α.

2.3. Apply the reflective projection from Fig. 3.5 to $\boldsymbol{x}_k + \alpha \boldsymbol{p}_k$ and obtain $\boldsymbol{x}_{k+1}^{\text{trial}}$.

3. Calculate LMA trial step via:

3.1. Perform the singular value decomposition of $\tilde{\boldsymbol{J}}_k$ as in Eq. (3.69) and compute $\tilde{\boldsymbol{B}}_k^{1/2},\ \tilde{\boldsymbol{g}}_k$, and $\tilde{\boldsymbol{B}}_k$ using Eqs. (3.70)–(3.72).

3.2. Solve Eq. (3.73) for $\tilde{\boldsymbol{z}}_k$ using Choleksy Factorization algorithm with substitutions described in Section 3.2.2.2, and determine the step vector via $\boldsymbol{p}_k = \boldsymbol{W}_k \tilde{\boldsymbol{B}}_k^{1/2} \tilde{\boldsymbol{z}}_k$.

3.3. Conduct line search from Eq. (3.79) to determine the scaling coefficient, α.

3.4. Apply the reflective projection from Fig. 3.5 to $\boldsymbol{x}_k + \alpha \boldsymbol{p}_k$ and obtain $\boldsymbol{x}_{k+1}^{\text{trial}}$.

4. Select the trial step that produces the lowest value of $f(\boldsymbol{x}_{k+1}^{\text{trial}})$.

5. Calculate η_k using Eq. (3.81) and set $\boldsymbol{x}_{k+1}$ and Δ_{k+1} according to Fig. 3.6.

6. IF $\Delta_k \leq \varepsilon_f$ **OR** $||\boldsymbol{p}_k|| \leq \varepsilon_p$ **OR** $f(\boldsymbol{x}_{k+1}) \leq \varepsilon_f$

6.1. Terminate.

END

END

Figure 3.2. Outline of the tandem trust-region algorithm, which combines Branch *et al.*'s [1] STIR and Bellavia and Riccietti's [2] LMA optimization techniques.

where $|\circ|$ denotes the element-wise absolute value, and $\text{diag}(\circ)$ converts an input vector to a diagonal matrix. The second affine-scaling matrix, $\boldsymbol{C}_k$, adjusts the diagonal elements of the Hessian based on the same principle. Similarly, its computation requires first calculating the Jacobian of $\boldsymbol{\sigma}_k$ with

respect to $\boldsymbol{x}_k$, $\boldsymbol{J}_k^\sigma$, which is a diagonal matrix with values of ± 1 and 0. Thereafter, the second affine-scaling matrix is computed by

$$\boldsymbol{C}_k = \boldsymbol{D}_k\big(\mathrm{diag}(\boldsymbol{g}_k)\ \boldsymbol{J}_k^\sigma\big)\boldsymbol{D}_k. \tag{3.60}$$

Note that all elements of $\boldsymbol{C}_k$ are non-negative because the nonzero elements of $\boldsymbol{J}_k^\sigma$ have the same sign as their correspondents in $\boldsymbol{g}_k$.

The STIR algorithm then applies a "subspace" implementation to Eq. (3.57), which reduces the step optimization from the full size of n variables to two dimensions by only evaluating points in the span of two basis vectors: $\boldsymbol{u}_1$ and $\boldsymbol{u}_2$. The first basis vector is the *steepest descent direction*, which in this case is the negative of the inversely affine-scaled gradient $\boldsymbol{u}_1 = -\boldsymbol{D}_k^{-1}\boldsymbol{g}_k$.

For the second subspace vector, calculation of an affine-scaled direction of negative curvature (*i.e.*, a vector satisfying $\boldsymbol{u}_2^T\bar{\boldsymbol{H}}_k\boldsymbol{u}_2 < 0$) is typically desired. However, when using the Hessian approximation from Eq. (3.56), sufficient directions of negative curvature cannot exist because $\boldsymbol{J}_k^T\boldsymbol{J}_k$ is always positive-definite. The definition of a negative curvature direction requires the Hessian to have at least one negative eigenvalue [111], which then allows for the existence of a vector satisfying $\boldsymbol{u}_2^T(\boldsymbol{H}_k + \boldsymbol{C}_k)\boldsymbol{u}_2 < 0$. Inserting the Hessian approximation from Eq. (3.56), the condition can be split into two terms as $2\boldsymbol{u}_2^T\boldsymbol{J}_k^T\boldsymbol{J}_k\boldsymbol{u}_2 + \boldsymbol{u}_2^T\boldsymbol{C}_k\boldsymbol{u}_2 < 0$. The left term is equivalent to $2(\boldsymbol{J}_k\boldsymbol{u}_2)^T(\boldsymbol{J}_k\boldsymbol{u}_2) \equiv 2||\boldsymbol{J}_k\boldsymbol{u}_2||^2$, which can never be negative. Similarly, the right term $\boldsymbol{u}_2^T\boldsymbol{C}_k\boldsymbol{u}_2$ must also be non-negative, because $\boldsymbol{C}_k$ is a diagonal matrix with only non-negative elements as discussed prior. Consequently, an approximate affine-scaled *Newton direction* is used for the second subspace vector, which is a solution to $\bar{\boldsymbol{H}}_k\boldsymbol{u}_2 = -\bar{\boldsymbol{g}}_k$.

Once the basis vectors are computed, the subspace is created by concatenating them into an n-by-2 transformation matrix, $\boldsymbol{S}_k = \big[\boldsymbol{u}_1\ \boldsymbol{u}_2\big]$. Following that, the gradient and Hessian are mapped to the 2D subspace by $\hat{\boldsymbol{g}}_k = \boldsymbol{S}_k^T\bar{\boldsymbol{g}}_k$ and $\hat{\boldsymbol{H}}_k = \boldsymbol{S}_k^T\bar{\boldsymbol{H}}_k\boldsymbol{S}_k$. Finally, by applying the transformation to the affine-scaled subproblem from Eq. (3.57), the affine-scaled subspace step optimization problem is obtained as

$$\min_{\hat{\boldsymbol{p}}_k} \hat{\phi}(\hat{\boldsymbol{p}}_k) = f(\boldsymbol{x}_k) + \hat{\boldsymbol{g}}_k^T\hat{\boldsymbol{p}}_k + \frac{1}{2}\hat{\boldsymbol{p}}_k^T\hat{\boldsymbol{H}}_k\hat{\boldsymbol{p}}_k, \quad ||\boldsymbol{S}_k\hat{\boldsymbol{p}}_k|| \le \Delta_k, \tag{3.61}$$

where the subspace step solution, $\hat{\boldsymbol{p}}_k$, is related to the full n-space solution by $\boldsymbol{p}_k = \boldsymbol{D}_k \boldsymbol{S}_k \hat{\boldsymbol{p}}_k$, thus determining the trial step vector for Eq. (3.52).

A Cholesky factorization algorithm [3, 112, 113] can be used to approximately solve Eq. (3.61). The technique is designed to calculate a solution for $\hat{\boldsymbol{p}}_k$ which resides on the trust-region boundary (*i.e.*, $||\boldsymbol{S}_k \hat{\boldsymbol{p}}_k|| = \Delta_k$). First, the subspace step optimization problem is re-posed as a scalar root-finding problem of the form

$$\hat{\varphi}(\lambda) = \frac{1}{||\boldsymbol{S}_k \hat{\boldsymbol{p}}_\lambda||} - \frac{1}{\Delta_k} = 0, \tag{3.62}$$

where $\lambda \geq 0$ is the Lagrange multiplier of the constraint from Eq. (3.61). By this formulation, step optimization involves solving for the optimal value of λ, which then implicitly determines the solution of interest, $\hat{\boldsymbol{p}}_\lambda$. A 1D Newton method is used to find a solution to Eq. (3.62). During each iteration of the Newton method, the current iterate of λ is added to the diagonal elements of the Hessian, and the result is Cholesky factorized such that

$$\hat{\boldsymbol{R}}_\lambda^T \hat{\boldsymbol{R}}_\lambda = \hat{\boldsymbol{H}}_k + \lambda \boldsymbol{I}_{2\times 2}, \tag{3.63}$$

where $\hat{\boldsymbol{R}}_\lambda$ is an upper triangular matrix and $\boldsymbol{I}_{2\times 2}$ is the 2-by-2 identity matrix. Afterward, the preconditioned conjugate gradients (PCG) method [1] is used to approximately solve

$$\hat{\boldsymbol{R}}_\lambda^T \hat{\boldsymbol{R}}_\lambda \hat{\boldsymbol{p}}_\lambda = -\hat{\boldsymbol{g}}_k \tag{3.64}$$

for the Cholesky-factorized step vector. Finally, the derivative of Eq. (3.62) is calculated via

$$\frac{d\hat{\varphi}}{d\lambda} = \frac{||\hat{\boldsymbol{R}}_\lambda^{-1} \hat{\boldsymbol{p}}_\lambda||^2}{||\boldsymbol{S}_k \hat{\boldsymbol{p}}_\lambda||^3}, \tag{3.65}$$

which is then used in the 1D Newton method to calculate the next iterate of λ. The initial guess for the Lagrange multiplier is $\lambda_0 = 1/\lambda_H$, where λ_H is the largest eigenvalue of $\hat{\boldsymbol{H}}_k$. The factorization algorithm terminates when either $\left|\frac{||\boldsymbol{S}_k \hat{\boldsymbol{p}}_\lambda|| - \Delta_k}{\Delta_k}\right| < 10^{-10}$ or 1,000 iterations have been performed. An outline of the Cholesky factorization algorithm is provided in Fig. 3.3.

Cholesky Factorization Algorithm
Given $\hat{\boldsymbol{H}}_k,\ \hat{\boldsymbol{g}}_k,\ \boldsymbol{S}_k,\ \Delta_k,\ \lambda_0$, and $i_{\max}$.

FOR $i = 1,\ 2,\ \ldots,\ i_{\max}$

1. Attempt Cholesky factorization for $\hat{\boldsymbol{R}}_\lambda = \hat{\boldsymbol{H}}_k + \lambda_{i-1}\boldsymbol{I}$

2. IF Factorization succeeds (*i.e.*, $\hat{\boldsymbol{R}}_\lambda$ exists)

2.1 Set $\hat{\boldsymbol{p}}_\lambda = -(\hat{\boldsymbol{R}}_\lambda^T \hat{\boldsymbol{R}}_\lambda)^{-1}\hat{\boldsymbol{g}}_k$.

ELSEIF Factorization fails **OR** $\lambda_{i-1} < 0$

2.2 Return $\hat{\boldsymbol{p}}_\lambda = -\frac{\Delta_k}{||\boldsymbol{S}_k \hat{\boldsymbol{H}}_k^{-1}\hat{\boldsymbol{g}}_k||}\hat{\boldsymbol{H}}_k^{-1}\hat{\boldsymbol{g}}_k$. (*Terminate algorithm.*)

END

3. Compute $\lambda_i = \lambda_{i-1} - \frac{\hat{\varphi}(\lambda_{i-1})}{\hat{\varphi}'(\lambda_{i-1})}$ using Eqs. (3.62) and (3.65).

4. IF $\left|\frac{||\boldsymbol{S}_k\hat{\boldsymbol{p}}_\lambda|| - \Delta_k}{\Delta_k}\right| < 10^{-10}$

4.1 Return current $\hat{\boldsymbol{p}}_\lambda$. (*Terminate algorithm.*)

ELSE

4.2 Continue.

END

END

Figure 3.3. Outline of Cholesky factorization algorithm adapted from Conn *et al.* [3].

3.2.2.2 Levenberg-Marquardt Algorithm

Compared to traditional trust-region methods, LMAs [114–116] use a slightly different approach to solve Eq. (3.52) for $\boldsymbol{p}_k$ by taking further advantage of the special structure of least-squares minimization problems. Because both the gradient and (approximate) Hessian are defined in relation to $\boldsymbol{J}_k$, the step optimization problem can be posed instead as a first-order Taylor series approximation of $\boldsymbol{\epsilon}(\boldsymbol{x}_k + \boldsymbol{p}_k)$ with respect to $\boldsymbol{p}_k$, yielding

$$\min_{\boldsymbol{p}_k} \psi(\boldsymbol{p}_k) = ||\boldsymbol{\epsilon}_k + \boldsymbol{J}_k\boldsymbol{p}_k||^2, \quad ||\boldsymbol{p}_k|| \leq \Delta_k. \tag{3.66}$$

In the formulation above, $\psi(\boldsymbol{p}_k)$ serves as an alternative to $\phi(\boldsymbol{p}_k)$ for estimating $f(\boldsymbol{x}_k + \boldsymbol{p}_k)$.

Recently, Bellavia and Riccietti [2] developed a robust Levenberg-Marquardt algorithm for ill-posed nonlinear least-squares problems with bound constraints. In this chapter, a modified version of their approach is used which better handles significant differences in the orders of magnitude among parameters commonly used in FWD backcalculation. First, the objective function is redefined as

$$\min_{\boldsymbol{p}_k} \psi(\boldsymbol{p}_k) = ||\boldsymbol{\epsilon}_k + \boldsymbol{B}_k^{1/2}\boldsymbol{p}_k||^2, \quad ||\boldsymbol{B}_k^{-1/2}\boldsymbol{W}_k^{-2}\boldsymbol{p}_k|| \leq \Delta_k. \tag{3.67}$$

Here, $\boldsymbol{B}_k$ is referred to as the *effective Hessian* and is analogous to $\boldsymbol{H}_k$ in Eq. (3.56); however, it is calculated instead via the singular value decomposition (SVD) of $\boldsymbol{J}_k$, which will be shown later. Similarly, $\boldsymbol{B}_k^{1/2}$ is the *effective Jacobian*, because $\boldsymbol{J}_k^T\boldsymbol{J}_k \equiv \boldsymbol{B}_k^{1/2,T}\boldsymbol{B}_k^{1/2} \equiv \boldsymbol{B}_k^{1/2}\boldsymbol{B}_k^{1/2}$. The weighting matrix, $\boldsymbol{W}_k = \text{diag}(\log|\boldsymbol{x}_k|)$, is used to scale the step vector such that each element is near the same order of magnitude based on a technique from Conn *et al.* [3] (§6.7.1). Similar to the affine-scaling procedure in the STIR method, Eq. (3.67) can be scaled based on the weighting matrix, yielding the equivalent problem

$$\min_{\tilde{\boldsymbol{p}}_k} \tilde{\psi}(\tilde{\boldsymbol{p}}_k) = ||\boldsymbol{\epsilon}_k + \tilde{\boldsymbol{B}}_k^{1/2}\tilde{\boldsymbol{p}}_k||^2, \quad ||\tilde{\boldsymbol{B}}_k^{-1/2}\tilde{\boldsymbol{p}}_k|| \leq \Delta_k, \tag{3.68}$$

where $\tilde{\boldsymbol{B}}_k^{1/2} = \boldsymbol{W}_k\boldsymbol{B}_k^{1/2}$, $\tilde{\boldsymbol{B}}_k^{-1/2} = \boldsymbol{W}_k^{-1}\boldsymbol{B}_k^{-1/2}$, and $\tilde{\boldsymbol{p}}_k = \boldsymbol{W}_k^{-1}\boldsymbol{p}_k$.

When solving for the LMA step in Eq. (3.68), $\tilde{\boldsymbol{B}}_k$ can be computed directly from the weighted Jacobian, $\tilde{\boldsymbol{J}}_k = \boldsymbol{J}_k\boldsymbol{W}_k$, instead of using the above relationships. First, the SVD of the weighted Jacobian is defined by

$$\boldsymbol{U}_k\boldsymbol{\Sigma}_k\boldsymbol{V}_k^T = \tilde{\boldsymbol{J}}_k, \tag{3.69}$$

where $\boldsymbol{U}_k$ and $\boldsymbol{V}_k$ are the $m \times m$ and $n \times n$ unitary matrices, respectively, and $\boldsymbol{\Sigma}_k$ is the $m \times n$ diagonal matrix of singular values corresponding to $\tilde{\boldsymbol{J}}_k$. From the decomposition, the weighted effective Jacobian ($\tilde{\boldsymbol{B}}_k^{1/2}$), weighted gradient ($\tilde{\boldsymbol{g}}_k$), and weighted effective Hessian ($\tilde{\boldsymbol{B}}_k$) are computed

from

$$\tilde{\boldsymbol{B}}_k^{1/2} = \boldsymbol{V}_k(\boldsymbol{\Sigma}_k^T\boldsymbol{\Sigma}_k)^{1/2}\boldsymbol{V}_k^T, \tag{3.70}$$

$$\tilde{\boldsymbol{g}}_k = 2\boldsymbol{V}_k\boldsymbol{\Sigma}_k^T\boldsymbol{U}_k^T\boldsymbol{\epsilon}_k, \tag{3.71}$$

$$\tilde{\boldsymbol{B}}_k = \boldsymbol{V}_k(\boldsymbol{\Sigma}_k^T\boldsymbol{\Sigma}_k)\boldsymbol{V}_k^T. \tag{3.72}$$

Finally, the objective function is restructured such that the constraint is of similar form as in Eq. (3.53) by reparameterizing $\tilde{\psi}$ with respect to $\tilde{\boldsymbol{z}}_k = \tilde{\boldsymbol{B}}_k^{-1/2}\tilde{\boldsymbol{p}}_k$. Applying this relationship and expanding $\tilde{\psi}$ yields

$$\min_{\tilde{\boldsymbol{z}}_k} \tilde{\psi}(\tilde{\boldsymbol{z}}_k) = f(\boldsymbol{x}_k) + (\tilde{\boldsymbol{B}}_k^{1/2}\tilde{\boldsymbol{g}}_k)^T\tilde{\boldsymbol{z}}_k + \tilde{\boldsymbol{z}}_k^T(\tilde{\boldsymbol{B}}_k^T\tilde{\boldsymbol{B}}_k)\tilde{\boldsymbol{z}}_k, \quad ||\tilde{\boldsymbol{z}}_k|| \leq \Delta_k, \tag{3.73}$$

whose solution is related to the full-space LMA step by $\boldsymbol{p}_k = \boldsymbol{W}_k\tilde{\boldsymbol{B}}_k^{1/2}\tilde{\boldsymbol{z}}_k$. In this formulation, the step optimization problem inherently adopts Tikhonov regularization properties that improve numerical characteristics of the calculation [2].

With minor adjustments, the Cholesky factorization algorithm can also solve Eq. (3.73). Here, the root-finding problem takes the form

$$\tilde{\gamma}(\lambda) = \frac{1}{||\tilde{\boldsymbol{z}}_\lambda||} - \frac{1}{\Delta_k} = 0, \tag{3.74}$$

where λ is now the Lagrange multiplier of the constraint from Eq. (3.73). Each iteration, the Cholesky factorization is performed via

$$\tilde{\boldsymbol{R}}_\lambda^T\tilde{\boldsymbol{R}}_\lambda = \tilde{\boldsymbol{B}}_k^T\tilde{\boldsymbol{B}}_k + \lambda\boldsymbol{I}_{n\times n}, \tag{3.75}$$

where $\tilde{\boldsymbol{R}}_\lambda$ is again an upper triangular matrix. Then, the Cholesky-factorized step vector is obtained by solving

$$\tilde{\boldsymbol{R}}_\lambda^T\tilde{\boldsymbol{R}}_\lambda\tilde{\boldsymbol{z}}_\lambda = -\tilde{\boldsymbol{B}}_k^{1/2}\tilde{\boldsymbol{g}}_k, \tag{3.76}$$

and the derivative of the root-finding problem for use in the 1D Newton method is now

$$\frac{d\tilde{\gamma}}{d\lambda} = \frac{||\tilde{\boldsymbol{R}}_\lambda^{-1}\tilde{\boldsymbol{z}}_\lambda||^2}{||\tilde{\boldsymbol{z}}_\lambda||^3}. \tag{3.77}$$

Thus, the Cholesky factorization procedure outlined in Fig. 3.3 can solve for the LMA step by applying the following substitutions: $\tilde{\boldsymbol{z}}_\lambda \rightarrow \hat{\boldsymbol{p}}_\lambda$, $\tilde{\boldsymbol{B}}_k^{1/2}\tilde{\boldsymbol{g}}_k \rightarrow \hat{\boldsymbol{g}}_k$, $\tilde{\boldsymbol{B}}_k^T\tilde{\boldsymbol{B}}_k \rightarrow \hat{\boldsymbol{H}}_k$, $\tilde{\boldsymbol{R}}_\lambda \rightarrow \hat{\boldsymbol{R}}_\lambda$, and $\boldsymbol{I}_{n\times n} \rightarrow \boldsymbol{S}_k$.

3.2.3 Step Vector Refinements

3.2.3.1 Line Search

The trust-region step vectors computed from the STIR or LMA methods are not always of optimal magnitude for reducing the error of the function at the current iteration because the factorization algorithm often terminates early—either when the Cholesky factorization of the current λ does not exist or when $\lambda < 0$. Early termination signifies a solution does not exist directly on the boundary of the trust-region for the current iteration (*i.e.*, $||\boldsymbol{S}_k\hat{\boldsymbol{p}}_k|| < \Delta_k$ for STIR or $||\tilde{\boldsymbol{z}}_k|| < \Delta_k$ for LMA). When termination occurs, the resulting step is adjusted using a line search optimization, which linearly scales the step vector along its direction. The line searches applied to the STIR and LMA step solutions are respectively

$$\min_\alpha \phi(\alpha\boldsymbol{p}_k) = f(\boldsymbol{x}_k) + \alpha\boldsymbol{g}_k^T\boldsymbol{p}_k + \frac{1}{2}\alpha^2\boldsymbol{p}_k^T\boldsymbol{H}_k\boldsymbol{p}_k, \tag{3.78}$$

$$\min_\alpha \psi(\alpha\boldsymbol{p}_k) = ||\epsilon_k + \alpha\boldsymbol{J}_k\boldsymbol{p}_k||^2. \tag{3.79}$$

Fig. 3.4 contains examples of how the approximation functions in Eqs. (3.78) and (3.79) can significantly vary with respect to the scaling factor, α. A step vector resulting from an early termination of the Cholesky factorization algorithm corresponds to $\alpha = 1$, which does not always produce a $\boldsymbol{p}_k$ of optimal length. The goal of the line search is to determine a value in the range $0.1 \leq \alpha \leq 10$ which produces the lowest $\phi(\alpha\boldsymbol{p}_k)$ when using the STIR method, or $\psi(\alpha\boldsymbol{p}_k)$ when using the LMA.

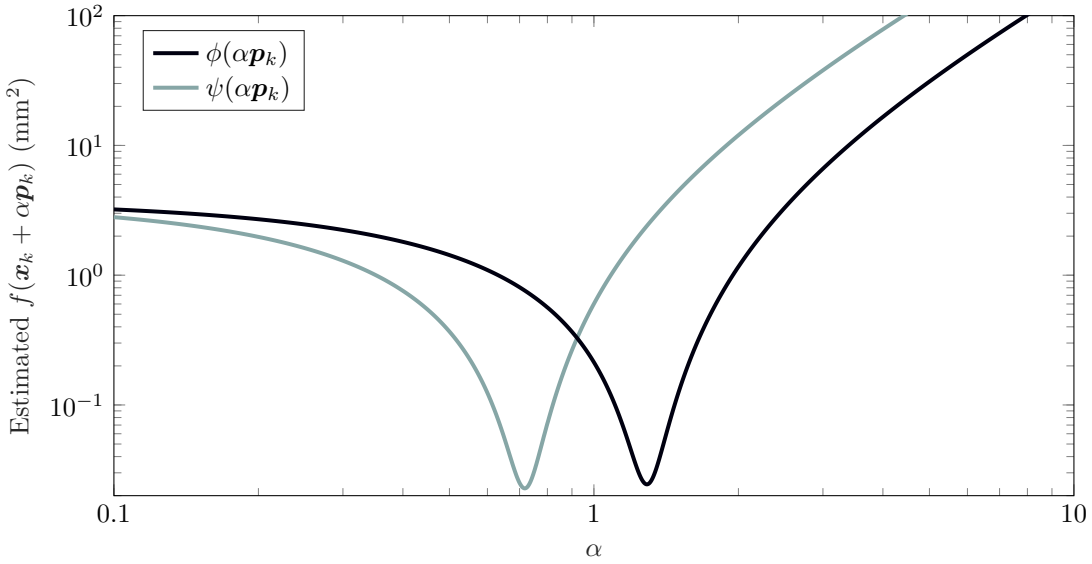

Figure 3.4. Demonstration of how scaling the step vector, $\boldsymbol{p}_k$, can significantly change the estimated value of $f(\boldsymbol{x}_k + \alpha \boldsymbol{p}_k)$ predicted by $\phi(\alpha \boldsymbol{p}_k)$ (from STIR, in black) and $\psi(\alpha \boldsymbol{p}_k)$ (from LMA, in gray). The unscaled step (*i.e.*, $\alpha = 1$) corresponds to the step vector output by the Cholesky factorization algorithm. Both approximations are calculated using the same values for $\boldsymbol{x}_k$, $\boldsymbol{J}_k$, $\boldsymbol{\epsilon}_k$, and $\boldsymbol{D}_k$.

3.2.3.2 Reflective Projection

The second adjustment made to the trust-region step solutions is to apply Coleman and Li's [4] reflective projection when $\alpha \boldsymbol{p}_k$ would cause $\boldsymbol{x}_{k+1}$ to exist outside the feasible region (*i.e.*, $\boldsymbol{x}_k$ breaches $\boldsymbol{b}^L$ or $\boldsymbol{b}^U$). The idea is to follow each variable in $\boldsymbol{x}_k$ as it travels along the step length and symmetrically reflect it off the boundary each time it would move past its upper or lower limit. The final value of the optimization variables after reflection becomes

$$\boldsymbol{x}_{k+1}^{\text{trial}} = \mathbb{R}(\boldsymbol{x}_k + \alpha \boldsymbol{p}_k), \tag{3.80}$$

where $\boldsymbol{x}_{k+1}^{\text{trial}}$ is the trial iterate produced by the trust-region step optimization problem, and $\mathbb{R}$ is the reflective projection. The algorithm used to perform the reflective transformation in the following numerical studies is summarized in Fig. 3.5. The technique has shown to be considerably robust in reducing the number of iterations in quadratic minimization problems such as Eq. (3.61) [1].

Reflective Projection Algorithm
Given $\boldsymbol{x} = \boldsymbol{x}_k + \alpha \boldsymbol{p}_k$, $\boldsymbol{b}^L$, $\boldsymbol{b}^U$, and $i_{\max}$.

FOR $i = 1,\ 2,\ \ldots,\ i_{\max}$

IF $b_i^L > -\infty$ **AND** $b_i^U = \infty$

$x_i = \max(\ x_i\ ,\ 2b_i^L - x_i\ )$

ELSEIF $b_i^L = \infty$ **AND** $b_i^U < \infty$

$x_i = \min(\ x_i\ ,\ 2b_i^U - x_i\ )$

ELSE

$\delta = \text{mod}\ (\ x_i - b_i^L\ ,\ 2(b_i^U - b_i^L)\ )$

$x_i = b_i^L + \min(\ \delta\ ,\ 2(b_i^U - b_i^L) - \delta\ )$

END

END

Figure 3.5. Algorithm for applying Coleman and Li's [4] reflective transformation.

3.2.4 Updating the Trust-Region Size

The final component of a TR method is to change the radius of the trust-region according to how effective the trial iterate is at reducing $f(\boldsymbol{x})$; after which, the trial iterate will be either accepted or rejected. Once the step optimization has been solved and any necessary refinements have been applied, the reduction quality of the trial step vector is determined by

$$\eta_k = \begin{cases} \dfrac{f(\boldsymbol{x}_{k+1}^{\text{trial}}) - f(\boldsymbol{x}_k)}{\phi(\alpha \boldsymbol{p}_k) - f(\boldsymbol{x}_k)}, & \text{for STIR solution;} \\ \\ \dfrac{f(\boldsymbol{x}_{k+1}^{\text{trial}}) - f(\boldsymbol{x}_k)}{\psi(\alpha \boldsymbol{p}_k) - f(\boldsymbol{x}_k)}, & \text{for LMA solution.} \end{cases} \tag{3.81}$$

The reduction quality parameter, η_k, is the ratio between the actual reduction and the predicted reduction in the function value when moving from $\boldsymbol{x}_k$ to the trial iterate. If the minimization is poor (*i.e.*, η_k is too low), then $\boldsymbol{x}_{k+1} = \boldsymbol{x}_k$ and the trust-region radius Δ_k is reduced for the next iteration. When the minimization is satisfactory, then $\boldsymbol{x}_{k+1} = \boldsymbol{x}_{k+1}^{\text{trial}}$, and the trust-region

radius either remains the same or is increased depending on how reduction effectiveness, which is determined by quality thresholds set at the user's discretion. The general procedure for updating the trust-region size each iteration is provided in Fig. 3.6.

Trust-Region Radius Updating Procedure
Given Δ_k, η_k, η_{low}, η_{high}.

IF $\eta_k \leq 0$

$$\boldsymbol{x}_{k+1} = \boldsymbol{x}_k, \quad \Delta_{k+1} = \xi_0 \Delta_k$$

ELSEIF $\eta_k < \eta_{\text{low}}$

$$\boldsymbol{x}_{k+1} = \boldsymbol{x}_k, \quad \Delta_{k+1} = \xi_1 \Delta_k$$

ELSEIF $\eta_k < \eta_{\text{high}}$

$$\boldsymbol{x}_{k+1} = \boldsymbol{x}_{k+1}^{\text{trial}}, \quad \Delta_{k+1} = \Delta_k$$

ELSE

$$\boldsymbol{x}_{k+1} = \boldsymbol{x}_{k+1}^{\text{trial}}, \quad \Delta_{k+1} = \xi_2 \Delta_k$$

END

Figure 3.6. Procedure for updating the trust-region radius for the next iteration, Δ_{k+1}. Here, $\boldsymbol{x}_{k+1}^{\text{trial}}$ is obtained from applying the reflective transformation to $\boldsymbol{x}_k + \boldsymbol{p}_k$.

3.3 Software Description

The primary goal of UGA-PAVE is to estimate the dynamic modulus master curve of the asphalt concrete layers using the FWD experimental data. The $|E^*|$ master curve can be considered "Level 1.5 inputs" in reference to the input hierarchy defined by the Mechanistic-Empirical Pavement Design Guide (MEPDG). The $|E^*|$ curves generated by UGA-PAVE resemble (but are not actually) Level 1 inputs. Obtaining true Level 1 inputs for a dynamic modulus master curve requires site-specific data tested at different temperatures; however, FWD testing can only be feasibly conducted at a single temperature *in situ*. To counteract this, a general time-temperature superposition (TTS) model is developed with the form

$$\beta(T) = \alpha_1 T^2 + \alpha_2 T + \alpha_3, \tag{3.82}$$

where β is the time-temperature superposition factor used to shift given $|E^*|$ curve, T is the desired temperature the curve will be shifted to, and α_i is the i^{th} TTS model coefficient. The model coefficients used by UGA-PAVE are based on averaged dynamic modulus data for hot-mix asphalt (HMA) from Kim [5], where the values are $\alpha_1 = 0.0012$, $\alpha_2 = -0.1773$, and $\alpha_3 = 3.2262$. With the model defined, the time-temperature superposition shifting is performed via

$$\log f_R = \log f - \log \beta(T), \tag{3.83}$$

where f is the frequency of the $|E^*|$ curve prior to shifting, and f_R is the corresponding reduced frequency in the master curve domain. In summary, the above procedure allows UGA-PAVE to estimate Level 1 $|E^*|$ master curve inputs from a single FWD test by extrapolating from averaged dynamic modulus data for HMA.

The first input page of the software is the Data Import Wizard, shown in Fig. 3.7. Additionally, a viewing pane that shows the current selections has been added for ease of viewing for large datasets. The second page is for Material Properties management, shown in Fig. 3.8. Here, the geometry and guesses for the layer moduli are entered into the software.

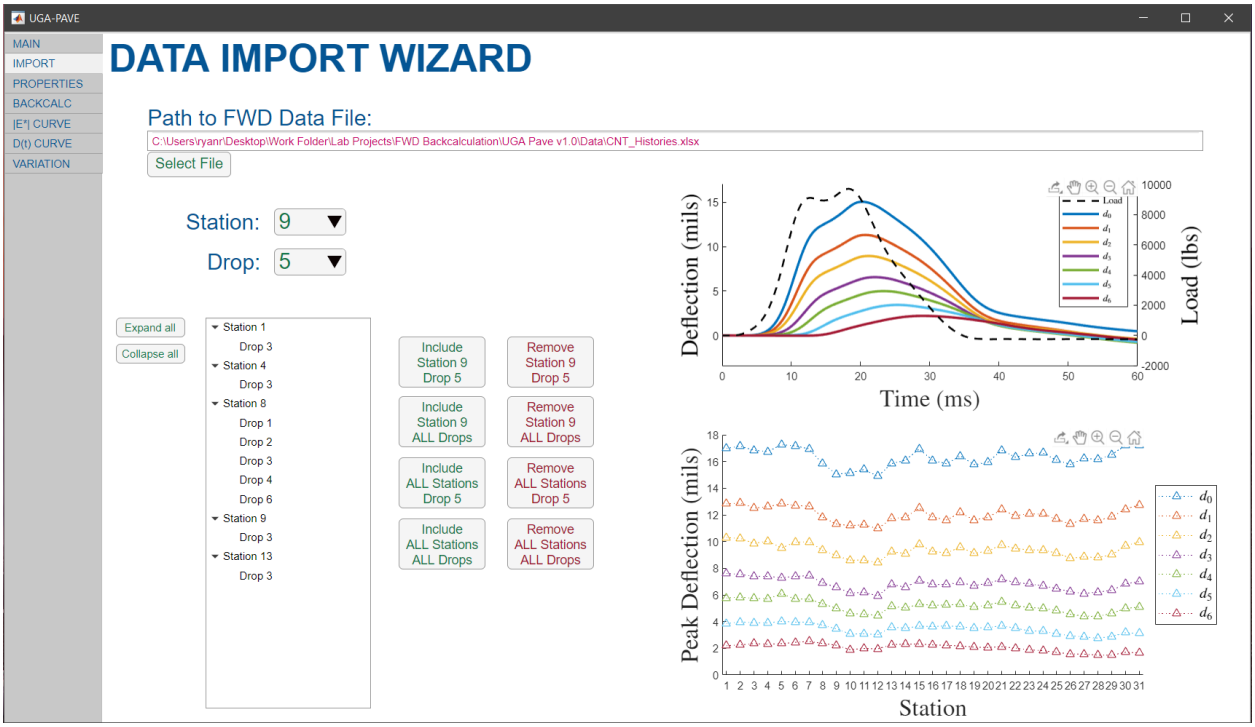

Figure 3.7. Example of the UGA-PAVE Data Import Wizard screen.

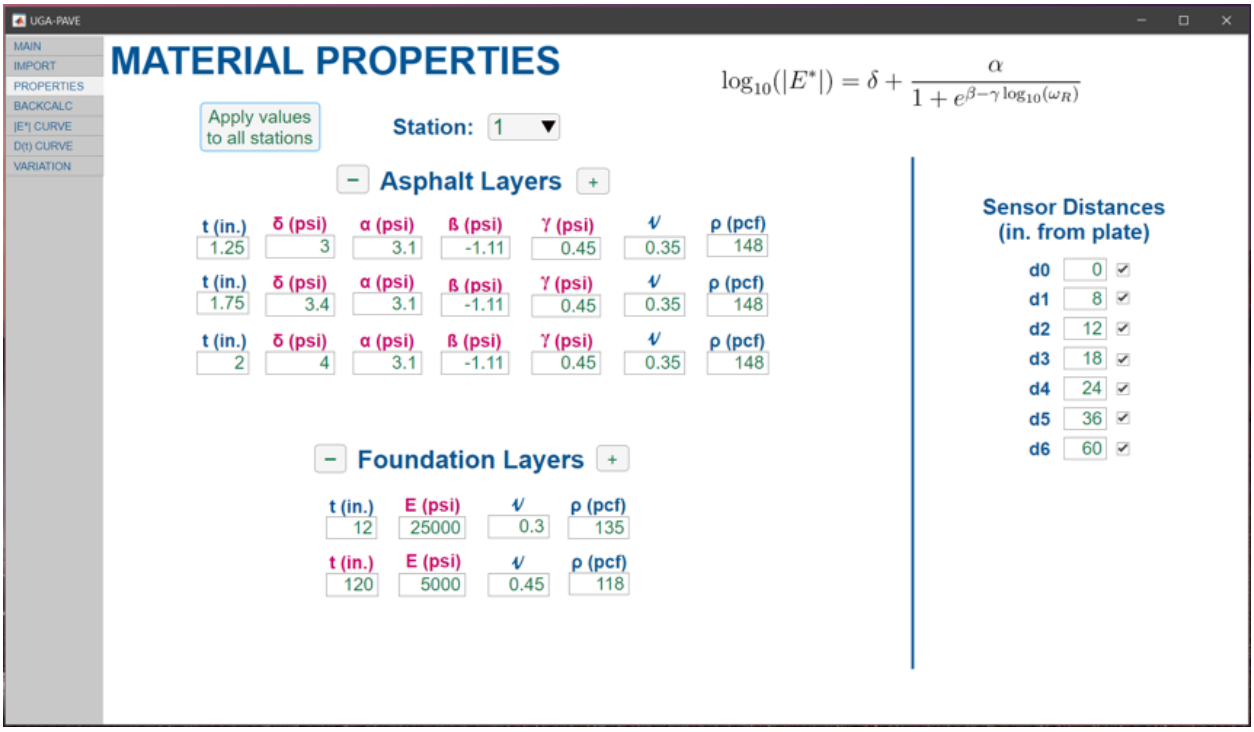

Figure 3.8. Example of the UGA-PAVE Material Properties input screen.

The third pertinent page is shown in Fig. 3.9 and is used to run and observe the FWD backcalculation. A notable feature has been implemented: an optional "2-Step BC" checkbox that is placed above the BACKCALCULATE button. Essentially, the first of the two steps performs the backcalculation by assuming all the asphalt lifts are equivalent; for example, if three lifts are specified on the material properties input page, all three are aggregated into one layer. Then, the second step segments the asphalt layer into the number of lifts specified on the Material Properties input page and conducts the backcalculation as intended, and the starting values for the dynamic moduli are set as the result obtained in the first step for the aggregate asphalt layer. This method increases the time each backcalculation takes but can potentially improve the accuracy of the backcalculation.

The following pages are for the software outputs. The first is the Dynamic Modulus Mastercurve results page in Fig. 3.10. The interface allows the user to view the entire backcalculated result from a selected station. For each station, there are five input fields for temperatures. In the primary input field "Station Temp:", the user should input the temperature of the pavement when the FWD test was performed. The other four temperature inputs correspond to the shifting temperatures used

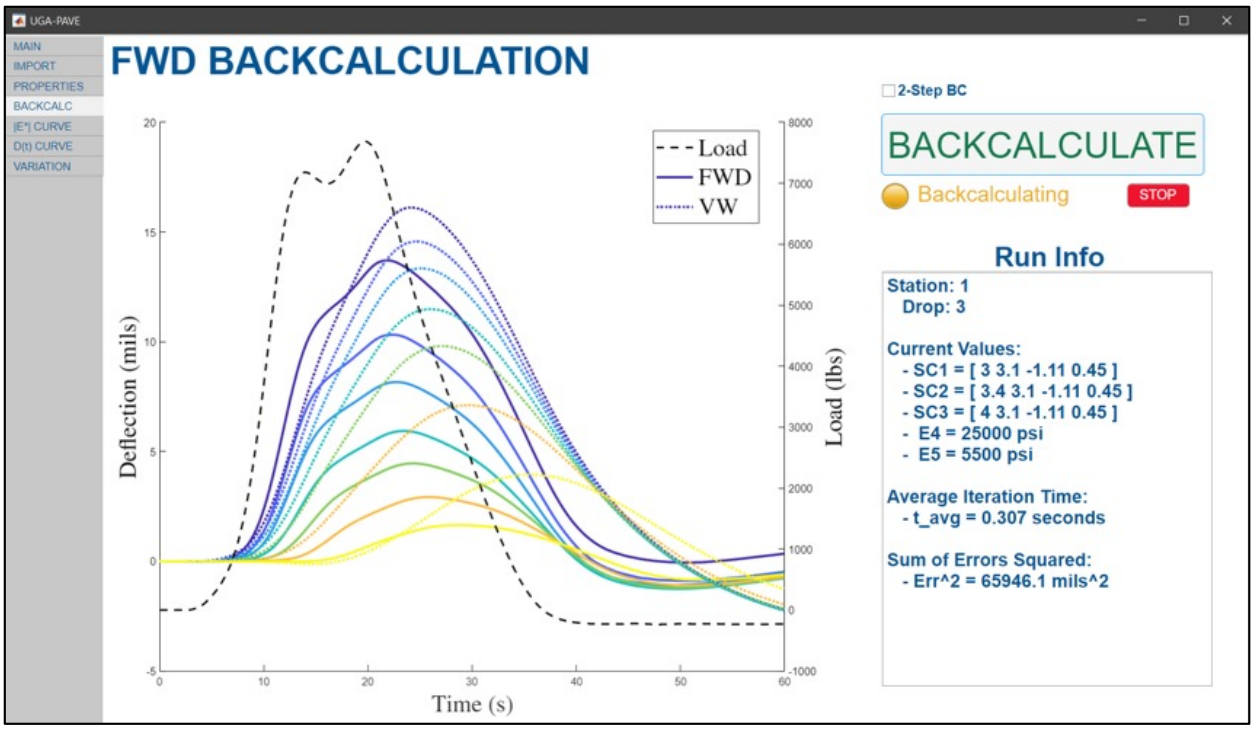

Figure 3.9. Example of the UGA-PAVE FWD Backcalculation runtime screen.

to construct the master curve, and they are already preset to AASHTOWare Pavement ME Design (PMED) software specifications. Below the temperature inputs are a number of time–temperature superposition factors. These allow the user to control the characteristics of the shifting used to construct the master curve, with predetermined values provided by default. The values are valid for a large range of hot mix asphalt mixes and were determined by averaging the lab results from asphalt cores tested by Kim *et al.* [5]. Finally, at the bottom right is a table of $|E^*|$ values that are taken from the master curve, which are automatically set to the arrangement used in PMED, and an export button that will output the values directly to the `.xml` file format used by PMED to be as user-friendly as possible. Each asphalt lift will have its own master curve generated, and a dropdown box is used to view and export the tabulated result.

The master curves generated are currently considered "Pseudo-Level 1" inputs. This name is adopted because the data at each temperature were not directly obtained through FWD testing at the temperatures. In other words, to have true Level 1 inputs, an FWD test would have to be performed at four different temperatures. However, for Pseudo-Level 1 inputs, an FWD test is only performed at one temperature, and the time–temperature superposition factors obtained

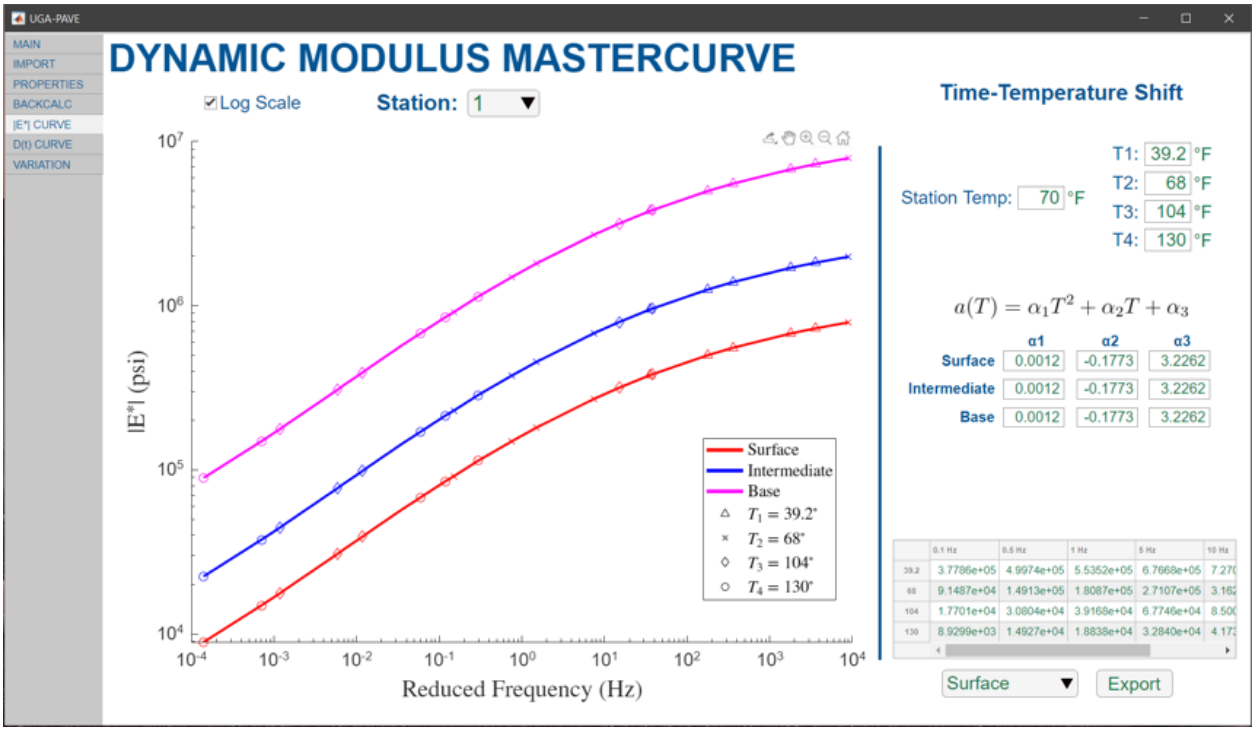

Figure 3.10. Example of the UGA-PAVE Dynamic Modulus Mastercurve results screen.

from a database are used to extrapolate what the FWD test results would be at all the other temperatures. One of the validation efforts conducted later in this study determined how accuracy between Pseudo-Level 1 inputs compares to traditional Level 1 inputs.

The next-to-last page provides the Creep Compliance Curve. As shown in Fig. 3.11, this page shares many similarities with the Dynamic Modulus Mastercurve page. The primary difference is that the result on this page is only of Level 2 input for the MEPDG. An interconversion technique developed by Park and Kim [79] is used to create the D(t) curves corresponding to the backcalculated $|E^*|$ data. An internal study was performed by the research team to determine these inputs drastically improve PMED's predictions for the terminal IRI and AC thermal cracking performance criteria compared to using regional-averaged Level 3 inputs. Finally, Fig. 3.12 shows the last results page: Moduli Variation. This page plots the moduli resulting from the backcalculation at all road stations to identify the locations of the weakest and strongest points of the pavement section. Values used to plot the variation of $|E^*|$ curves are taken using the dynamic modulus estimated at a loading frequency of 1 Hz.

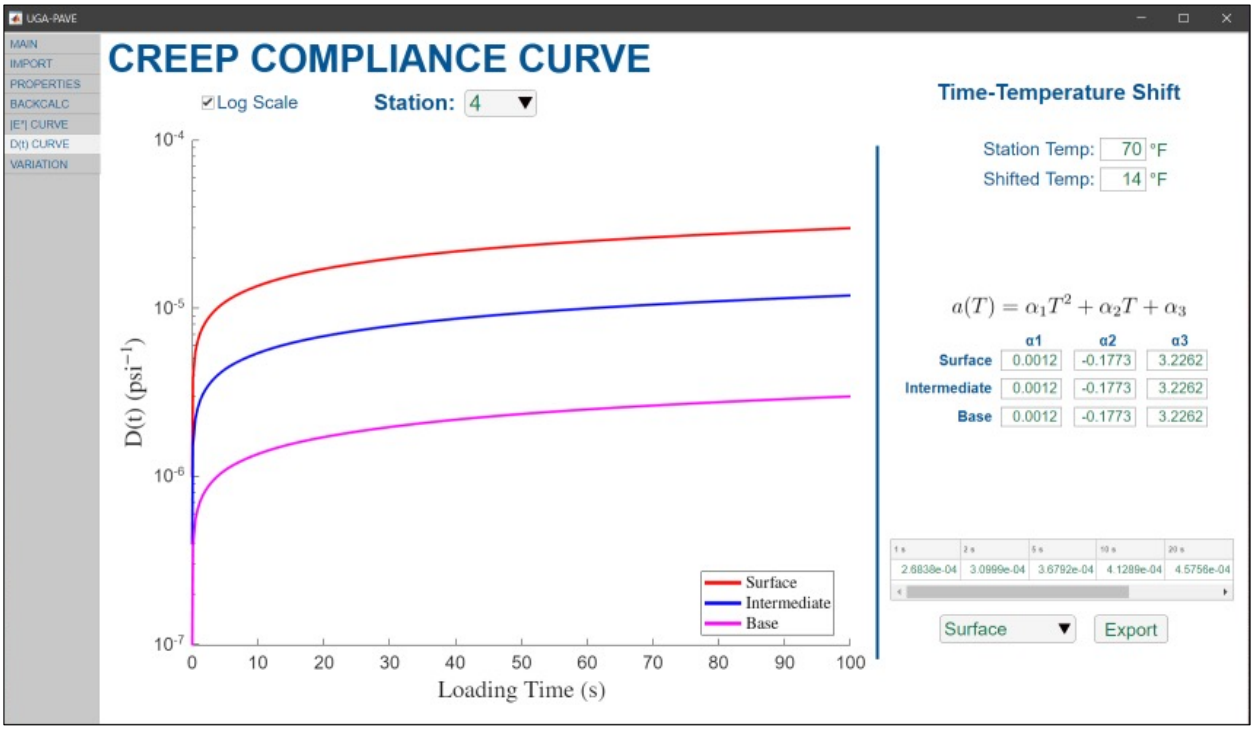

Figure 3.11. Example of the UGA-PAVE Creep Compliance Curve results screen.

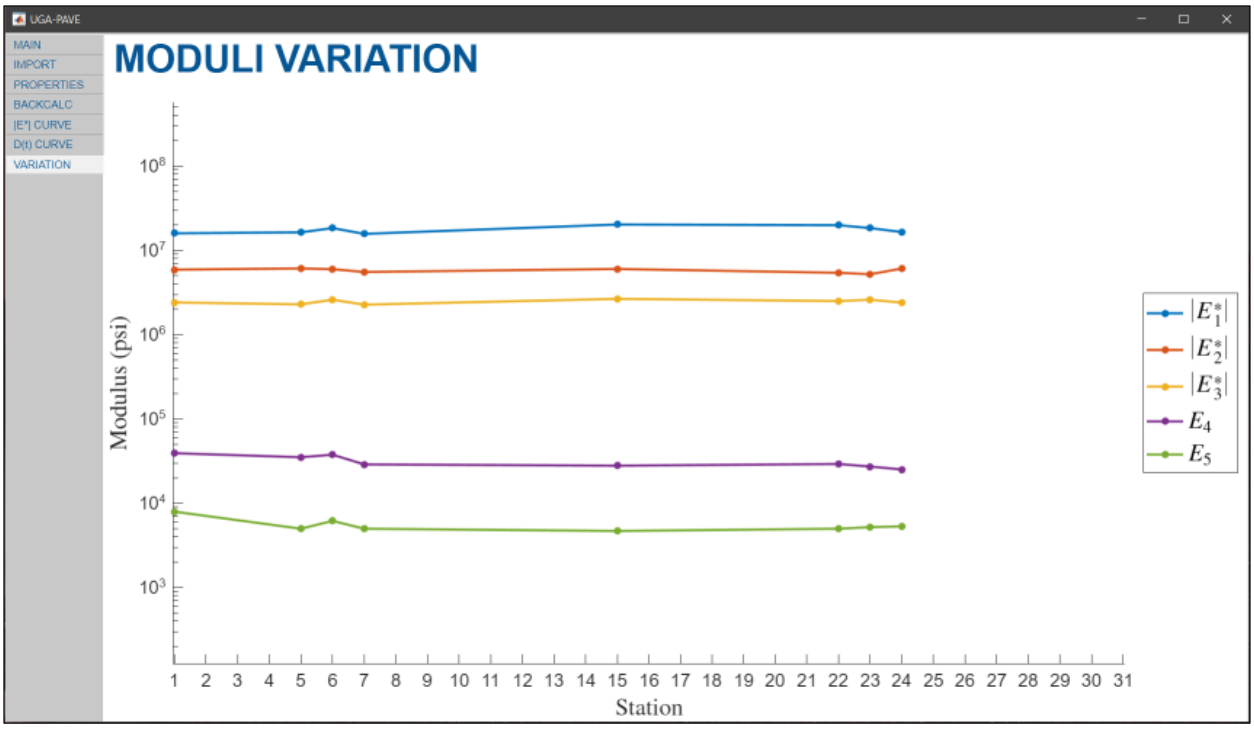

Figure 3.12. Example of the UGA-PAVE Moduli Variation results screen.

Chapter 4

UGA-PAVE Verification

4.1 Ill-Posed Backcalculation Demonstration

In this section, a demonstration of the issues caused by ill-posedness in FWD backcalculation is provided. First, a brief description of the relevant portions of the FWD backcalculation procedure is discussed in Section 4.1.1 to provide ample background. Then in Section 4.1.2, the demonstration is presented and the novel suitable minimum criterion is defined, which will be used in the performance tests in Section 4.3.

4.1.1 Summary of FWD Backcalculation Procedure

The primary goal of FWD backcalculation is to estimate the *in situ* stiffness of a flexible pavement section, which requires a theoretical representation of its material properties. Asphalt concrete is well-known to be viscoelastic; thus, the linearly elastic Young's modulus is insufficient for characterizing its stiffness. In pavement engineering, it is common practice to model the strength of asphalt concrete with the dynamic modulus, $|E^*(f)|$, which is a function of sinusoidal loading frequency, f. The nomenclature for dynamic modulus is often abbreviated to $|E^*|$ for convenience. One of the most popular approaches for modeling a dynamic modulus curve is to use a sigmoidal approximation of the form [72]

$$\log(|E^*(f)|) = d_1 + \frac{d_2}{1 + e^{d_3 + d_4 \log(f)}}, \tag{4.1}$$

where d_1 is the minimum modulus value in logarithmic scale, d_2 is the range of modulus values, and d_3 and d_4 are shape parameters corresponding to the slope and position of the sigmoid. Thus, by modeling the asphalt stiffness via Eq. (4.1), four sigmoidal parameters per AC layer need to be included in $\boldsymbol{x}$ for the optimization. An example dynamic modulus curve is given in Fig. 4.1.

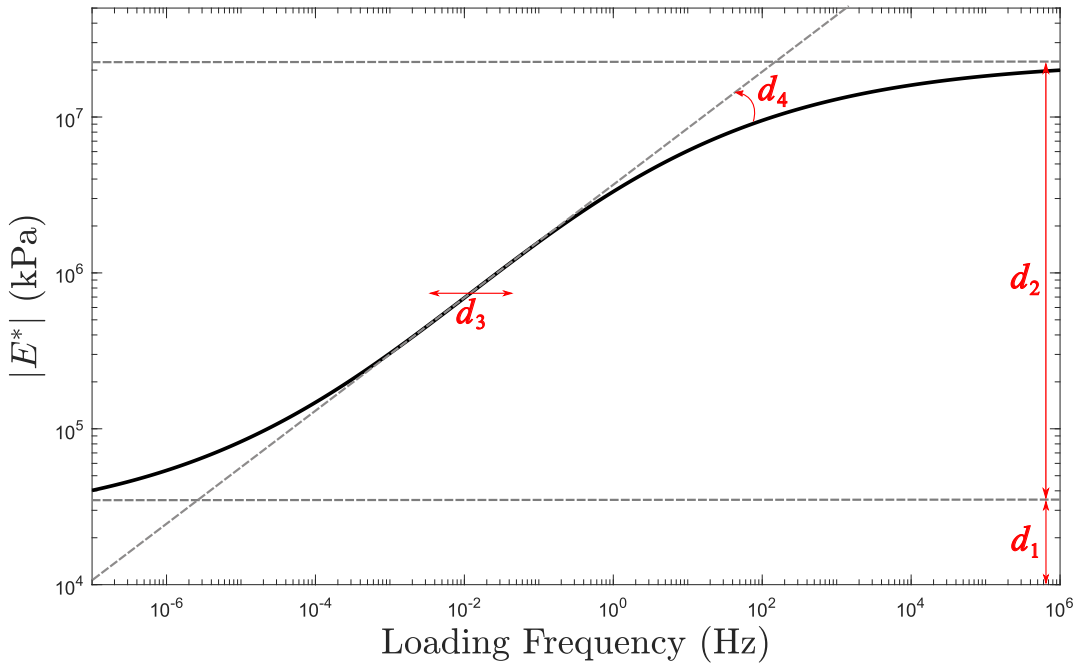

Figure 4.1. Example dynamic modulus sigmoidal approximation with labels for the sigmoidal coefficients, $d_1 - d_4$.

4.1.2 Ill-Posed Example

Once the optimization converges, an $|E^*|$ curve can be constructed directly from each set of sigmoidal parameters in $\boldsymbol{x}^*$. However, the optimization is ill-posed, and thus a given set of deflection curves are rarely unique with respect to the pavement layer moduli (*i.e.*, the sigmoidal coefficients of viscoelastic layers and the Young's moduli of linearly elastic layers). In other words, numerous distinct combinations of layer moduli values can lead the pavement model to produce nearly identical deflection time histories.

First a computational model of the hypothetical pavement structure with two distinct asphalt lifts is created, which serves as the forward model to determine $F(\boldsymbol{x})$ in Eq. (3.51). Then, a starting guess for the material properties, $\boldsymbol{x}_0$, is randomly generated, and the FWD backcalculation is

performed until a set of layer moduli are taken from an optimization run that terminates at an appreciably low magnitude of $f(\boldsymbol{x}^*)$. A low sum of squared errors means the predicted deflection time histories, $F(\boldsymbol{x}^*)$, are nearly identical to the set of observations, $\boldsymbol{y}$. Then, dynamic modulus curves are reconstructed using the optimized parameters and compared with the "truth" $|E^*|$ curves to illustrate their similarity, where the truth curves are generated from the parameters used to create the hypothetical pavement structure.

The deflections produced by both the truth and $\boldsymbol{x}^*$ sigmoidal moduli are plotted in Fig. 4.2a, and their corresponding dynamic modulus curves are plotted in Fig. 4.2b. It is evident from the figure that the backcalculated parameters predict a deflection response which is nearly equivalent to that from the truth parameters, only having a least-squares error of $f(\boldsymbol{x}^*) = 6.039 \cdot 10^{-4}$ mm^2; however, the values for the sigmoidal coefficients in $\boldsymbol{x}^*$ differ from their correspondents in the truth set by 30% on average. Hence, converging to a local minimum (*i.e.*, any $\boldsymbol{x}^*$) does not guarantee that the backcalculated dynamic moduli are near the truth values. Consequently, the concept of *suitable minimum* is introduced to classify a local minimum that is acceptably close to the global minimum, or truth minimum.

The criterion for quantifying a suitable minimum is based on how closely the $|E^*|$ curve of the backcalculated parameters matches one constructed from the truth values. However, yet another issue arises due to the dynamic modulus being a function of loading frequency. Taking a fast Fourier transform (FFT) of the force signal (see Fig. 4.3) reveals the $|E^*|$ curves backcalculated from experimental data are only accurate for a limited range of frequencies. Converting to the frequency domain reveals the FWD force signal hardly perturbs frequencies beyond 100 Hz. Furthermore, the lower bound of excited frequencies is limited to 16.67 Hz due to the narrow sampling window of 60 ms, indicated by the sharp drop-off below this frequency. The manifestation of this issue in FWD backcalculation is demonstrated in Fig. 4.2b, where the curves only match well in the frequency range of 1 to 100 Hz. This finding was recently investigated by Fu *et al.* [101], who dubbed it as the "effective frequency range" (EFR). In their investigation, they found the EFR was reasonably limited to an even narrower band between 5 and 65 Hz.

The backcalculation results are significantly less reliable outside of the EFR, because the optimization algorithms must extrapolate from trends within the range of excited frequencies. The suitable minimum definition is therefore designed to consider both ill-posedness and the EFR, which

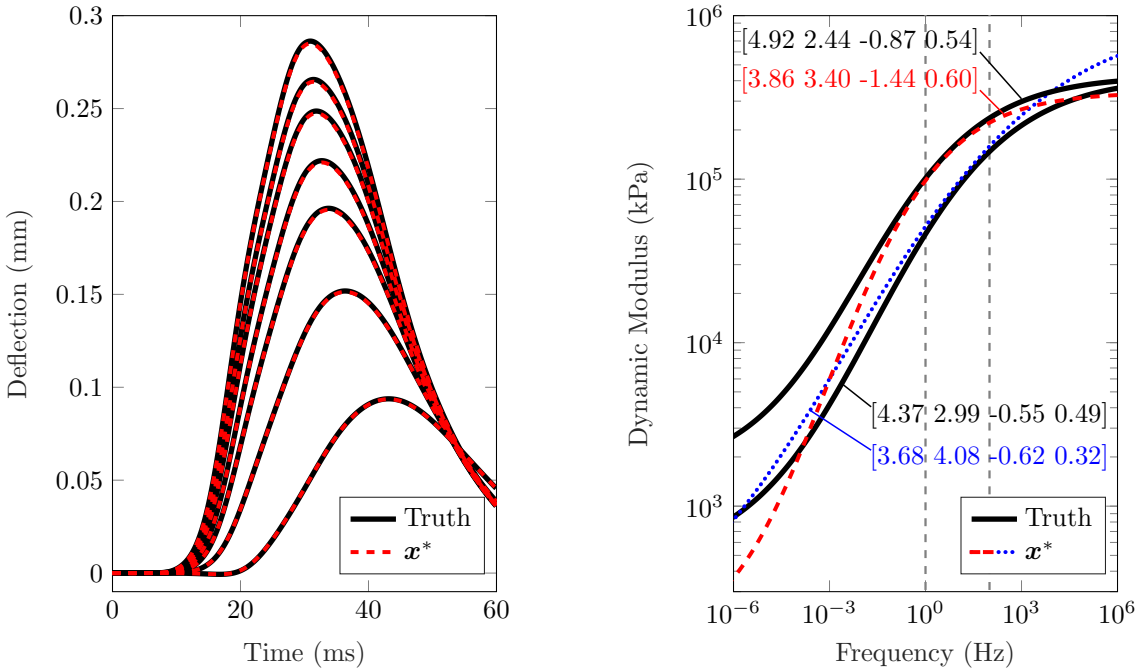

Figure 4.2. Comparison between the (a) FWD deflections and (b) dynamic modulus curves of the truth value parameters of Model A and a local minimum ($\boldsymbol{x}^*$) from a STIR run. In (b), two $|E^*|$ curves are generated from $\boldsymbol{x}^*$, one for the surface AC layer (dotted blue) and one for the base AC layer (dashed red), and annotated numbers provide the corresponding dynamic moduli (d_1, d_2, d_3, d_4). The dashed gray lines in (b) identify the range of frequencies where the dynamic modulus curves produced by $\boldsymbol{x}^*$ match well with those corresponding to the truth set.

for the force signals used in this chapter is 16.67 Hz $\leq f \leq$ 100 Hz. Henceforth, a suitable minimum is any such $\boldsymbol{x}^*$ that deviates from the truth curve by no more than an average 10% difference within the specified effective frequency range. This deviation is calculated by

$$\Psi = \frac{100\%}{N} \sum_{i=1}^{N} \left| \frac{|E_i^*|_{\boldsymbol{x}^*} - |E_i^*|_{truth}}{|E_i^*|_{truth}} \right|, \tag{4.2}$$

where Ψ is the average percent deviation, N is the number of discrete frequency points on the range 16.67 Hz $\leq f \leq$ 100 Hz, and $|E_i^*|$ is dynamic modulus value corresponding to the i^{th} discrete frequency. The limit of 10% was determined to be the highest reasonable difference before a backcalculated curve becomes appreciably dissimilar in magnitude from the truth curve within the EFR.

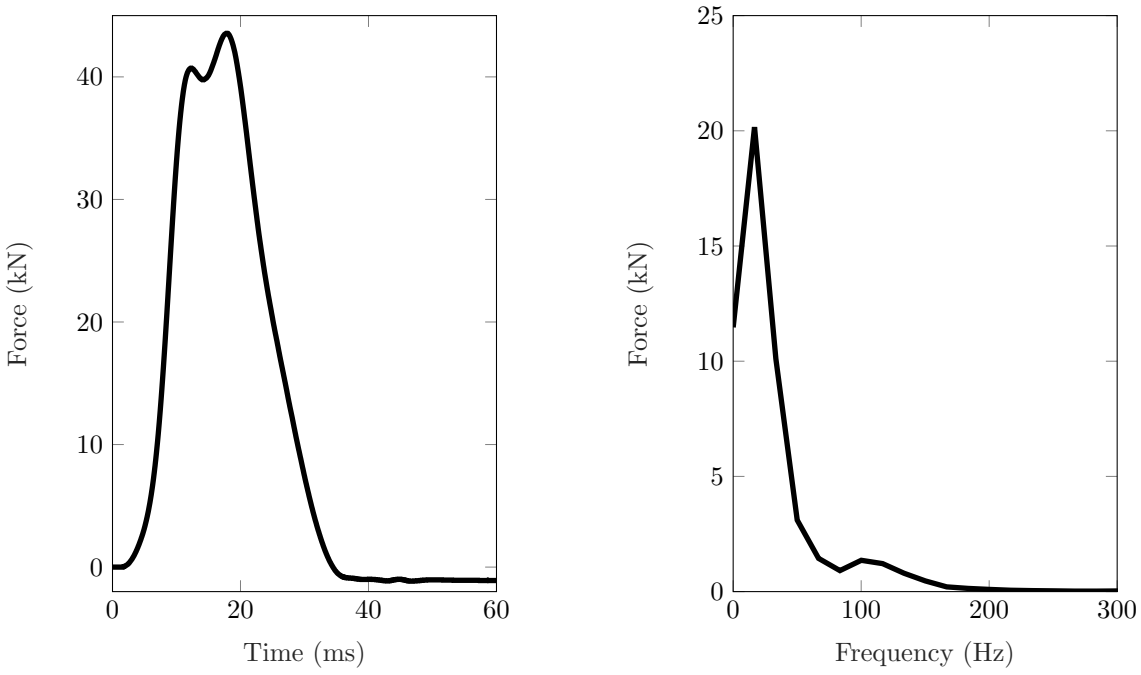

Figure 4.3. Plots of (a) an FWD force signal in the time domain and (b) the same signal converted to the frequency domain using the fast Fourier transform.

4.2 Verification Procedure

In this section, the procedure for simulating FWD backcalculation for the following numerical studies in Section 4.3 is detailed. Pavement backcalculation consists of two aspects—a forward model and an optimizer. The optimization scheme iteratively inputs a set of parameters into the forward model and adjusts the parameters based on the model output until some termination criterion is achieved. First, the forward problem model will be discussed in two parts, beginning with the approach used to characterize the viscoelastic stiffness of asphalt concrete and followed by the geometry and material properties of the simulated pavement structures. Then, the settings used to perform each optimization will be detailed. The entirety of the backcalculation procedure is conducted using MATLAB.

Table 4.1. Truth parameter values used to generate four ViscoWave models for the simulated FWD backcalculations. Sigmoidal coefficients (*i.e.*, d_1—d_4) are in units of log(kPa).

Model	Layer	d_1	d_2	d_3	d_4	E (MPa)	ρ ($^{kg}/_{m^3}$)	ν	h (cm)
A	AC1	4.3730	2.9887	-0.5495	0.4880	–	2242.6	0.35	5.715
	AC2	4.9160	2.4438	-0.8724	0.5420	–	2242.6	0.35	8.890
	GAB	-	-	-	-	153.0	1922.2	0.40	30.48
	Subgrade	-	-	-	-	26.92	1601.8	0.45	637.0
B	AC1	3.4410	3.9226	-0.9564	0.4130	–	2242.6	0.35	4.445
	AC2	4.5670	2.7909	-1.1085	0.4880	–	2242.6	0.35	6.985
	GAB	-	-	-	-	182.0	1922.2	0.40	30.48
	Subgrade	-	-	-	-	31.52	1601.8	0.45	1118.6
C	AC1	4.0630	2.9436	-0.4364	0.4580	–	2242.6	0.35	3.175
	AC2	4.9160	2.4438	-0.8724	0.5420	–	2242.6	0.35	9.525
	GAB	-	-	-	-	193.1	1922.2	0.40	30.48
	Subgrade	-	-	-	-	48.83	1601.8	0.45	1124.2
D	AC1	4.4200	2.9436	-0.4364	0.4580	–	2242.6	0.35	2.540
	AC2	4.2250	3.1424	-0.9206	0.4390	–	2242.6	0.35	3.810
	GAB	-	-	-	-	151.5	1922.2	0.40	30.48
	Subgrade	-	-	-	-	49.73	1601.8	0.45	826.0

4.2.1 Forward Models

Lee's ViscoWave (VW), outlined in Chapter 3, is used as the pavement model in all simulated backcalculations. Four different VW pavement models—denoted A, B, C, and D—are used in all studies. Each model consists of four axisymmetric material layers: two distinct asphalt concrete layers at the top, a graded aggregate base (GAB) layer (*i.e.*, crushed rock) in the middle, and a subgrade soil layer at the foundation. A visualization of the general layout used for all models is shown in Fig. 4.4, and the material properties and geometry of each are given in Table 4.1. The values for the dynamic moduli (d_1–d_4) are derived from various hot mix asphalt samples tested by Kim *et al.* [5], and an overall damping of 0.1% is assumed for all cases. The remaining material property and geometry values are chosen from ranges based on pavement configurations common in Georgia, USA.

The FWD load signals used to impact each model are obtained from force histories recorded by Dynatest FWD equipment. For all models, the load is applied perpendicularly to the pavement surface and distributed across a 15.24 cm length beginning at its upper-left corner, ($r = z = 0$),

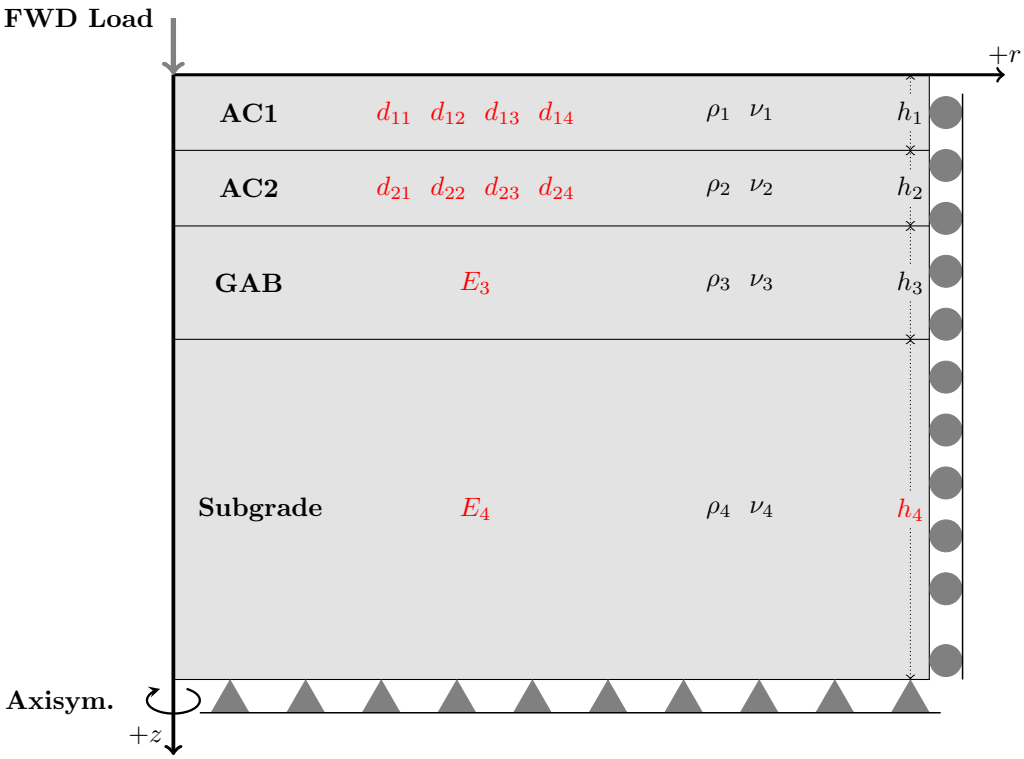

Figure 4.4. General layout of the four ViscoWave models. Parameters varied in the optimization (dynamic moduli and subgrade layer thickness) are highlighted in red; all others (densities, Poisson ratios, and non-subgrade layer thicknesses) remain constant and are in black. The first subscript of each sigmoidal parameter corresponds to the AC layer, and the second denotes the coefficient number from Eq. (4.1). All models are axisymmetric about the z-axis with pinned boundary conditions along their bottom edges (denoted by triangular markers) and roller boundary conditions along their right edges (denoted by circular markers).

to emulate the 30.48 cm diameter load plate of the FWD equipment. It is common practice to conduct multiple FWD tests of varying load magnitudes; in consideration of this, three force signals with different peak magnitudes are used for the excitation: 22.4, 33.6, and 43.6 kN. After one of the load signals is applied, the displacement sensor measurements are simulated by probing the displacements at locations $r = 0,\ 20.32,\ 30.48,\ 45.72,\ 60.96,\ 91.44$, and 152.4 cm along the r-axis of the ViscoWave model.

4.2.2 Optimization Routines

Four different optimization methods are used in the following studies. The first three are the custom-written STIR, LMA, and TTR algorithms, and the *lsqnonlin* solver from MATLAB's Optimization Toolbox is used for the fourth optimizer. Due to *lsqnonlin* being proprietary, the algorithm's

parameter values (*e.g.*, those governing trust-region radius updating) are not known beyond those given in the package's documentation (MATLAB Optimization Toolbox [117]). Thus, there is limited user control over the functionality of *lsqnonlin*, whereas full control is available for the custom STIR, LMA, and TTR optimizers. Any parameters able to be defined by the user in *lsqnonlin* but not specified below are set to their defaults as described in [117] (*e.g.*, the "Algorithm" option is set to "trust-region-reflective").

First, the parameters consistent across all four optimization routines will be discussed. The limits of the reduction quality parameter (used in Fig. 3.6 to update the TR radius) are $\eta_{\text{low}} = 0.25$ and $\eta_{\text{high}} = 0.75$. The total number of iterations allowed for a given optimization run, $k_{\max}$, is limited to 150, and the function and step tolerances, ε_f and ε_p, are set to 2^{-52} (machine precision) and 10^{-10}, respectively. Finally, a finite difference step size of 0.01 is used to calculate the finite difference derivatives in all algorithms.

Next, the optimization parameters that could be set in the custom scripts, but not in *lsqnonlin*, will be given. In general, the size of the trust-region should begin relatively large and become progressively smaller as $f(\boldsymbol{x}_k)$ decreases. The initial value of the TR radius for the STIR, LMA, and TTR implementations is $\Delta_0 = \max(\ ||\boldsymbol{b}^U - \boldsymbol{b}^L||\ ,\ \sqrt{10}\ )$, and the trust-region radius adjustment factors are set as $\xi_0 = 1/32$, $\xi_1 = 1/4$, and $\xi_2 = 2$. Note that the value of $\sqrt{10}$ in the definition of the initial trust-region radius serves as the minimum possible starting size and was determined to be the most effective overall out of a range of tested values.

To test the algorithms' effectiveness in backcalculation problems of varying sizes (*i.e.*, quantities of updating variables), six different optimization cases are considered. The details of each case are given in Table 4.2. There are effectively seven output variables for each model, each being a time history predicted by ViscoWave at the location of one of the deflection sensors. Therefore, the backcalculation becomes ill-posed when the size of the optimization problem is eight or higher. The subgrade thickness, h_4, is included in each case because it uniquely pertains to geometry (*i.e.*, by modifying the model's physical size), whereas all other parameters are representative of material properties.

Sets of initial guesses for the STIR, LMA, TTR, and *lsqnonlin* algorithms are created using a sampling approach. The Latin hypercube sampling (LHS) algorithm is chosen to generate all $\boldsymbol{x}_0$ samples in this chapter due to its reliability in producing an efficient sampling space and its

Table 4.2. The size of the optimization problem and list of updating variables corresponding to each optimization case. The first subscript of each sigmoidal parameter corresponds to the AC layer, and the second denotes the coefficient number from Eq. (4.1).

Case	Size	Optimized Variables
1	5	$d_{11},\ d_{12},\ d_{13},\ d_{14},\ h_4$
2	6	$d_{11},\ d_{12},\ d_{13},\ d_{14},\ E_3,\ h_4$
3	7	$d_{11},\ d_{12},\ d_{13},\ d_{14},\ E_3,\ E_4,\ h_4$
4	9	$d_{11},\ d_{12},\ d_{13},\ d_{14},\ d_{21},\ d_{22},\ d_{23},\ d_{24},\ h_4$
5	10	$d_{11},\ d_{12},\ d_{13},\ d_{14},\ d_{21},\ d_{22},\ d_{23},\ d_{24},\ E_3,\ h_4$
6	11	$d_{11},\ d_{12},\ d_{13},\ d_{14},\ d_{21},\ d_{22},\ d_{23},\ d_{24},\ E_3,\ E_4,\ h_4$

lack of restrictions on the number of samples. General formulations of LHS and other sampling methods are detailed by Giunta *et al.* [118]. To conduct LHS, the user first selects bounds to define a parameter space, and the method divides each axis of the space to form a number of bins. The user then specifies a quantity of samples to randomly generate according to a handful of rules such that all $\boldsymbol{x}_0$ points are distributed throughout the bounded domain in a manner which limits the amount of bias to any given sub-domain.

A total of 36,000 initial guesses were generated via LHS for the following numerical studies; the procedure for generating samples is as follows. First, a model-case-force combination is selected (*e.g.*, Model B, Optimization Case 4, Force 1). Then, 500 Latin hypercube samples are generated using the parameter bounds from Table 4.3. Next, the STIR, LMA, TTR, and *lsqnonlin* optimizers are employed 500 times each—once per $\boldsymbol{x}_0$ sample generated for the selected model-case-force combination. Once concluded, the next model-case-force combination is chosen (*e.g.*, Model B, Case 4, Force 2), and the procedure repeats, beginning with a new set of 500 samples generated by LHS. It is emphasized that for a given model-case-force combination, all four optimizers use the same set of 500 samples as the initial guesses for the simulated backcalculations.

Table 4.3. Bounds used to generate Latin Hypercube samples for all optimization cases.

Parameter	Units	Lower Bound	Upper Bound
d_1	log(kPa)	2.538	5.338
d_2	log(kPa)	2.838	5.838
d_3	—	-1.5	-0.35
d_4	—	0.3	0.6
E_3	MPa	68.95	275.8
E_4	MPa	13.79	55.16
h_4	m	0.9144	27.43

4.3 Performance Tests

In this section, the STIR, LMA, and TTR algorithms as outlined in Section 3.2 are used along with the MATLAB Optimization Toolbox's *lsqnonlin* package to simulate 36,000 dynamic FWD backcalculations, and the results are compared. First, the benefit of using a tandem step calculation is demonstrated in Section 4.3.1 through a comparison of the custom STIR, LMA, and TTR algorithms. Then, the TTR algorithm is compared with MATLAB's *lsqnonlin* solver in Section 4.3.2 to evaluate TTR in reference to an existing commercial option.

Two kinds of performance tests are used in both subsections. The first is a minimization test, whereby the particular algorithms are compared to see how effectively they reduce the magnitude of the objective function, $f(\boldsymbol{x})$, which corresponds to how similar the measured and predicted deflections are. A performance metric is devised to illustrate the relative likelihoods for the optimizers to converge to a particular error magnitude. First, all $\boldsymbol{x}^*$ found by the optimizers from LHS are grouped into bins according to the magnitudes of their final function values (*i.e.*, 10^{-10}, 10^{-9}, ... , 10^{4} mm^2). Then, the performance metric is calculated within each error bin (*e.g.*, $10^{-8} \leq f(\boldsymbol{x}^*) \leq 10^{-7}$) by

$$P_{\mathrm{TTR}} = 100\% \cdot \frac{n_{\mathrm{TTR}}}{n_{\mathrm{TTR}} + n_{\mathrm{rival}}}. \tag{4.3}$$

where n_{TTR} and n_{rival} are the number of $\boldsymbol{x}^*$ found by TTR and the "rival" optimizers within the given error bin, and P_{TTR} is the percent of the total $\boldsymbol{x}^*$ found by TTR within the error bin. Thus,

values of $P_{\text{TTR}} > 50\%$ indicate TTR found more minima within a particular error bin than the rival solver (*e.g.*, STIR), whereas the converse is true for values of $P_{\text{TTR}} < 50\%$.

The second performance test evaluates the effectiveness of each optimizer for dynamic modulus backcalculation. For each model-case combination, the percentage of suitable minima found by each optimizer out of the number of LHS samples is calculated. For each data point, the percentage corresponds to 1500 LHS samples (one model, one optimization case, all three forces).

4.3.1 Effectiveness of Tandem Step Calculation

In this section, the custom STIR, LMA, and TTR scripts are compared to demonstrate the effectiveness of the tandem step calculation of the TTR optimizer detailed in Section 3.2. These comparisons are intended to provide insight into the improvements that a tandem approach offers for optimization performance in dynamic FWD backcalculation. The studies in this subsection pertain to the three custom algorithms: STIR, LMA, and TTR. The TTR algorithm is a combination of the individual STIR and LMA methods shown; therefore, the following results demonstrate the general benefit of the tandem step calculation.

4.3.1.1 Minimization

First, the optimizers' capabilities for objective function minimization is discussed. The custom STIR method demonstrated a similar performance as the custom LMA; therefore, it is sufficient to compare TTR with either the STIR or LMA optimizers to demonstrate the benefits of the tandem step implementation. For this performance test, the custom STIR is selected over LMA, because it is more similar to MATLAB's *lsqnonlin* as used in Section 4.3.2.

Gradient bar plots are created to illustrate the minimization performance of the STIR and TTR optimizers for the well-posed cases in Fig. 4.5. For Models A, C, and D, TTR facilitated better minimization overall by both converging to low-error magnitudes more often and high-error magnitudes less often than STIR. For Model B, TTR is considered to only slightly outperform STIR. Although STIR shows a slight advantage at the lowest error bin ranging from $10^{-10} \leq f(\boldsymbol{x}^*) \leq 10^{-9}$, the dominance of blue hues for $f(\boldsymbol{x}^*) \geq 10^{-2}$ mm^2 indicates STIR converged to high-error minima notably more often. Furthermore, TTR had a significant concentration of minima found between

the 10^{-9} and 10^{-8} error bounds. Thus, the TTR method offers improved minimization capability compared to its individual STIR component in well-posed FWD backcalculation.

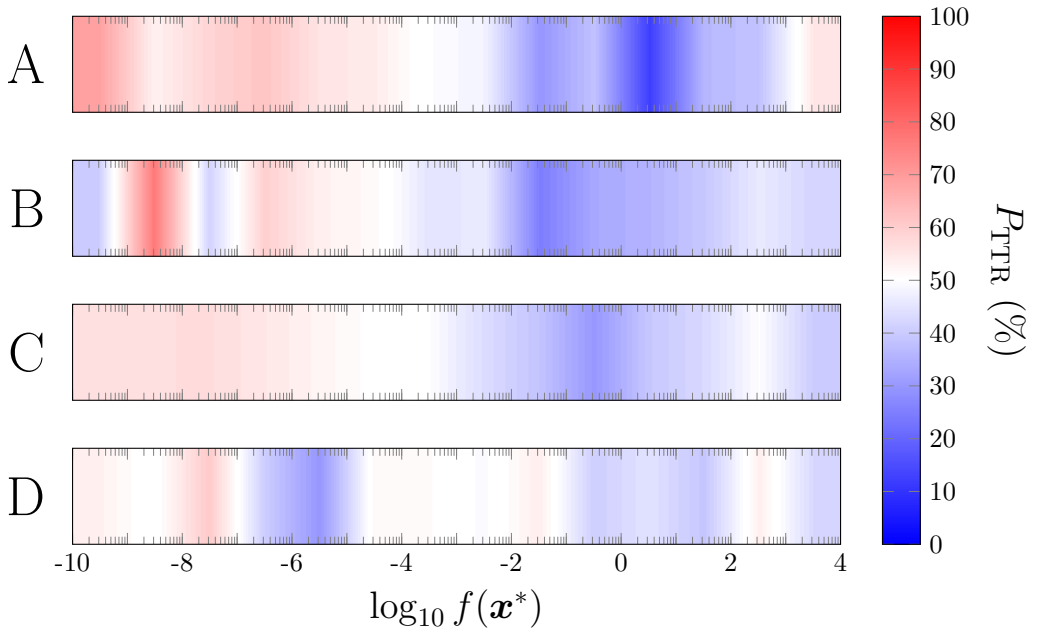

Figure 4.5. Comparison between STIR and TTR for the well-posed cases (1, 2, and 3) from the LHS testing. All local minima found are grouped into bins based on the magnitude of their corresponding sum of squares error. The color bar corresponds to the percent of the minima found by TTR for a given error bin. Red hues indicate TTR dominates the bin, blue hues indicate STIR dominates, and white represents a tie.

Fig. 4.6 contains the Latin hypercube sampled minimization results of STIR and TTR for the ill-posed cases. The gradient bar plots for all models are primarily red-dominated on their left halves and blue-dominated on their right halves; therefore, TTR outperforms STIR in general for the ill-posed cases. The most notable difference is associated with Model B, where TTR found 100% of the local minima at the lowest error range and had a dominant performance overall in the left half of the bar plot. TTR also had an impressive showing in the sampling results for Models A and C, where the left halves of the plots are almost entirely red, and the right halves are mostly blue. The results for Model D were slightly less dominant for TTR. The STIR solver had a strong presence in the left half of the plot near $f(\boldsymbol{x}^*) = 10^{-6}$ mm^2; however, TTR converged to a notably higher concentration of minima in the error range $10^{-9} \leq f(\boldsymbol{x}^*) \leq 10^{-7}$ mm^2.

For Models A and B, TTR converged to a greater number of minima within the highest error bin. For these models, the high-error minima found by TTR were concentrated between 10^3 and

10^4 mm^2, whereas with STIR they were spread among the bins ranging from 10^{-2} to 10^3 mm^2. Despite this, TTR is still considered to perform better than STIR for these models. Aside from TTR being more prevalent in the low error ranges, the practical difference in quality between two minima corresponding to $f(\boldsymbol{x}^*) = 10^{-1}$ and 10^4 mm^2 is often negligible because neither are likely to be suitable minima.

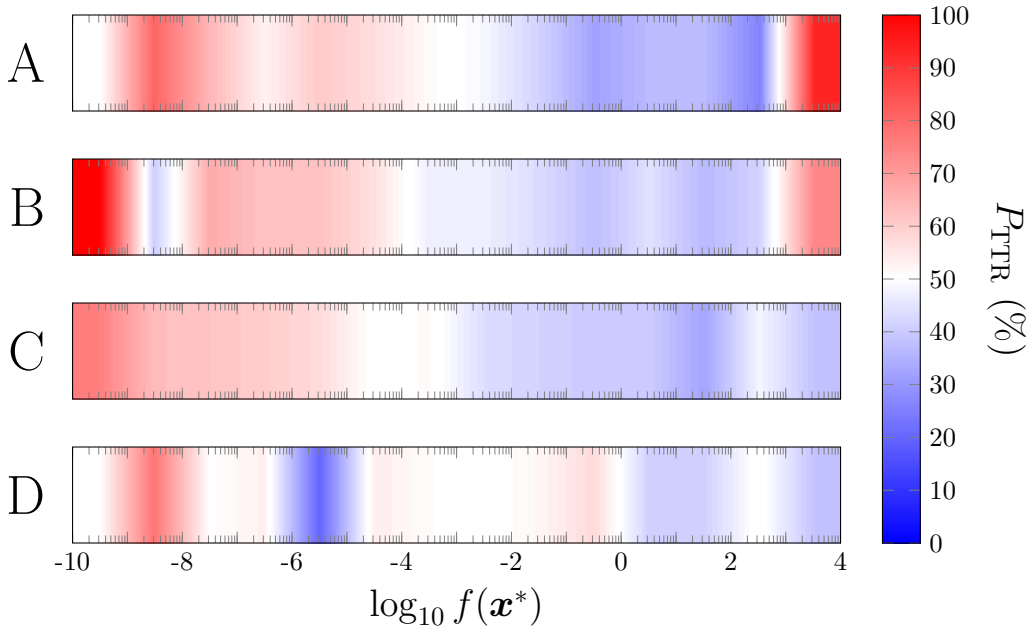

Figure 4.6. Comparison between STIR and TTR for the ill-posed cases (4, 5, and 6) from the LHS testing. All local minima found are grouped into bins based on the magnitude of their corresponding sum of squares error. The color bar corresponds to the percent of the minima found by TTR for a given error bin. Red hues indicate TTR dominates the bin, blue hues indicate STIR dominates, and white represents a tie.

4.3.1.2 Dynamic Modulus Reconstruction

Although TTR does provide benefits in general for minimizing the objective function, the degree of minimization has little bearing on whether or not the given minimum from an ill-posed optimization is useful (see Section 4.1). A practical backcalculation is typically ill-posed in nature; therefore, the optimizers' performances are more accurately expressed by comparing their ability to converge to suitable minima rather than their capability to minimize the objective function's value.

The percentage of suitable $\boldsymbol{x}^*$ found by STIR, LMA, and TTR is plotted versus the optimization size (which is controlled by the case; see Table 4.2) in Fig. 4.7. Each data point in a line plot represents a percentage of 1500 LHS samples (one model, one case, and three load signals as

described in Section 4.2.2). For each model-case combination, TTR outperformed both of its component methods in obtaining suitable minima. In the well-posed regime (*i.e.*, seven or fewer variables) for Models A, B, and D, the three optimizers had appreciably similar results overall, commonly finding suitable minima for more than 90% of the LHS samples. In the ill-posed regime, the reliability of each optimizer decreases dramatically; however, TTR begins to outperform its counterparts—significantly for Models A and B, and moderately for D.

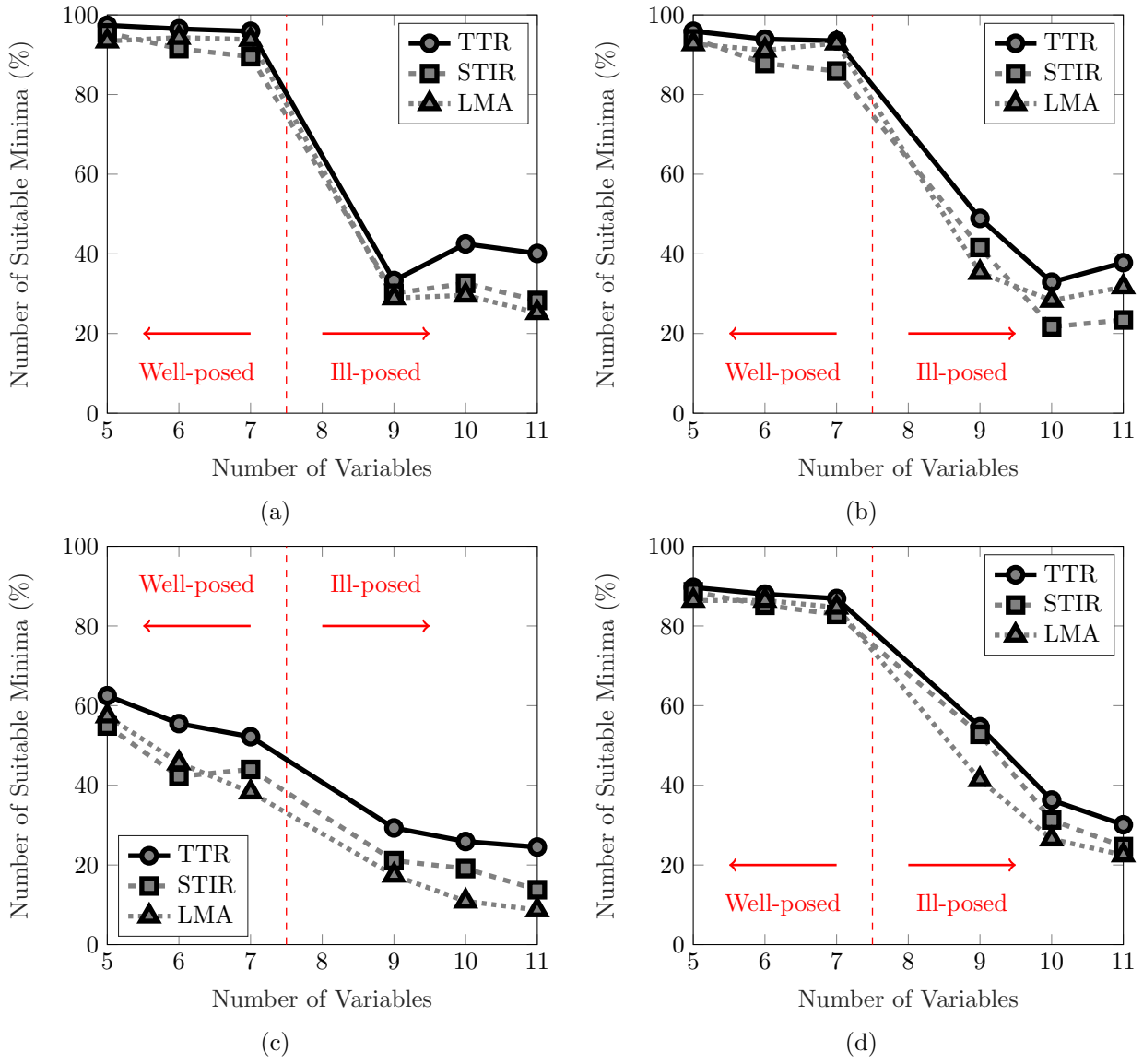

Figure 4.7. The percentage of $\boldsymbol{x}^*$ classified as suitable minima at different optimization sizes for Models (a) A, (b) B, (c) C, and (d) D. Results are shown for the custom STIR, LMA, and TTR algorithms. Each data point reflects a percentage of 1500 data points. For example, a value of 90% means 1350 of the 1500 LHS samples led to suitable minima.

The backcalculation for Model C stands out compared to the other three models, where the optimizers had the worst average performance in well-posed cases but the best overall in ill-posed cases. Interestingly, the STIR optimizer demonstrated considerable difficulty finding suitable minima even in the well-posed cases and had a nearly linear decrease in reliability with increasing optimization size. One notable result is TTR demonstrated the most significant performance margin over STIR and LMA in the ill-posed regime. Reviewing the truth properties in Table 4.1, Model C stands out in two ways: (1) having the largest thickness ratio between AC2 and AC1, and (2) having the strongest combined GAB and Subgrade elastic moduli. Based on the poor relative performance in the well-posed cases, FWD backcalculation of pavements with these characteristics may be a difficult scenario. However, for such a situation, TTR demonstrated a clear improvement regarding dynamic modulus estimation. Across all models, the tandem approach demonstrated relative improvements of 33.9% and 56.9% compared to the STIR and LMA methods, respectively, for ill-posed dynamic modulus backcalculation.

4.3.2 Comparison of TTR with Commercial Option

The previous section demonstrates the benefits of implementing the tandem trust-region approach relative to its component STIR and LMA optimizers. Here, the custom TTR algorithm is compared to MATLAB's *lsqnonlin* package to compare the developed technique's effectiveness in FWD backcalculation versus a robust commercial option. The *lsqnonlin* optimizer is effectively a more refined version of the custom STIR, as both packages operate on the same fundamental principles. This section is intended to further demonstrate that TTR is a superior choice for FWD backcalculation despite its constituents being outperformed by *lsqnonlin*.

4.3.2.1 Minimization

The minimization performances of both *lsqnonlin* and TTR for the well-posed optimization cases are compared in Fig 4.8. For Models A and D, TTR minimizes moderately better overall, having a higher tendency to find minima corresponding to lower magnitudes of error. However, with Models B and C *lsqnonlin* performs slightly better because it found more minima in the lowest error bin of $10^{-10} \leq f(\boldsymbol{x}^*) \leq 10^{-9}$ mm^2. Despite these discrepancies, both optimizers performed quite similarly

overall as noted by a lack of dark red or blue regions, which indicates P_{TTR} generally stays between 35% and 65% for the well-posed cases.

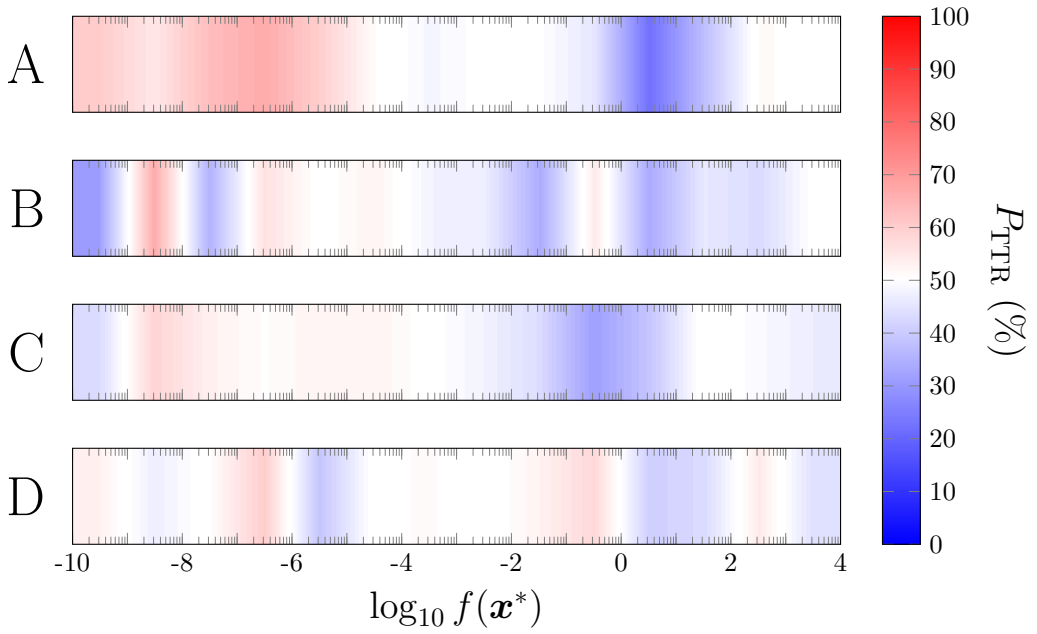

Figure 4.8. Comparison between *lsqnonlin* and TTR for the well-posed cases (1, 2, and 3) from the LHS testing. All local minima found are grouped into bins based on the magnitude of their corresponding sum of squares error. The color bar corresponds to the percent of the minima found by TTR for a given error bin. Red hues indicate TTR dominates the bin, blue hues indicate *lsqnonlin* dominates, and white represents a tie.

TTR and *lsqnonlin* are compared for the ill-posed cases in Fig. 4.9. The tandem trust-region solver performed better with Model A seeing as TTR considerably dominates the left half of the plot in addition to finding 100% of the minima in the leftmost error bin. One observation in the results for Model A is TTR exhibited a tendency to converge to minima corresponding to the highest error bin between 10^3 and 10^4 mm^2. However, the corresponding high-error minima found by *lsqnonlin* were concentrated in the range $10^2 \leq f(\boldsymbol{x}^*) \leq 10^3$, which are as unlikely to be suitable minima as those in the highest error bin.

The tandem optimizer also triumphed over *lsqnonlin* in Models C and D, where the left halves of the plots are red-dominated and the right halves are blue-dominated. For Model B, however, *lsqnonlin* has a notable advantage, as similar to the corresponding results for the well-posed cases. Not only did *lsqnonlin* find a greater number of high-error minima, but it was less likely to converge to minima in the highest error bin than TTR.

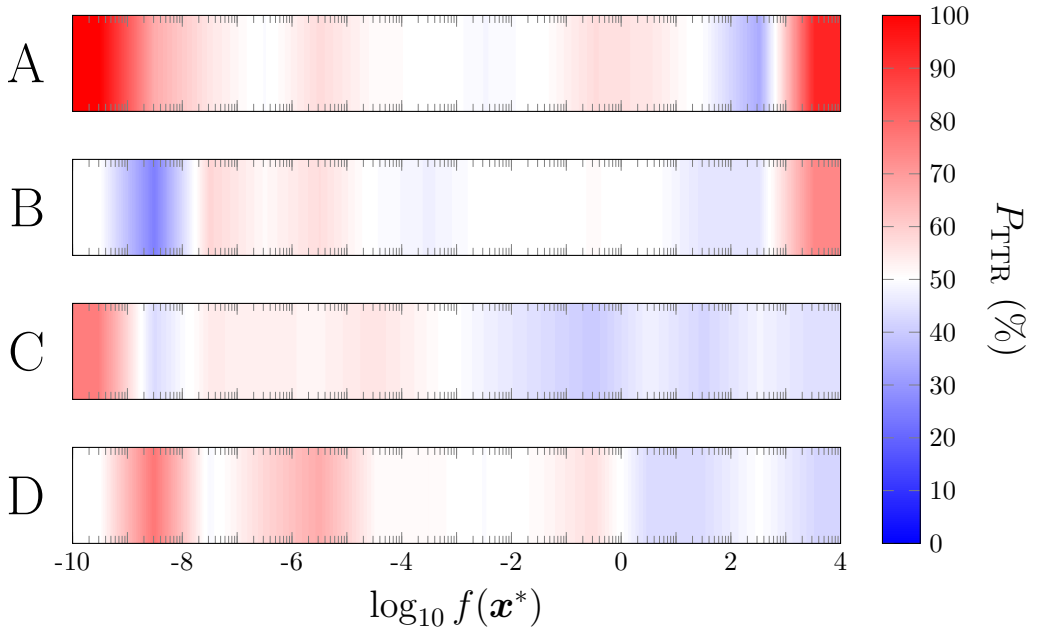

Figure 4.9. Comparison between *lsqnonlin* and TTR for the ill-posed cases (4, 5, and 6) from the LHS testing. All local minima found are grouped into bins based on the magnitude of their corresponding sum of squares error. The color bar corresponds to the percent of the minima found by TTR for a given error bin. Red hues indicate TTR dominates the bin, blue hues indicate *lsqnonlin* dominates, and white represents to a tie.

Regarding minimization effectiveness, TTR has favorable performance for the well and ill-posed optimization cases in general. Though *lsqnonlin* demonstrated better minimization capability with Model B, the tandem trust-region optimizer demonstrated superior performance for Models A, C, and D, especially in the ill-posed cases. Therefore, TTR has shown to be more effective than *lsqnonlin* at minimizing the sum of squared errors in dynamic FWD backcalculation problems.

4.3.2.2 Dynamic Modulus Reconstruction

Again, an optimizer with the ability to reduce Eq. (3.51) to low magnitudes does not necessarily guarantee the minima found are practical in the context of FWD backcalculation. Thus, TTR is compared here with *lsqnonlin* to assess which is better for reconstructing dynamic modulus curves. The number of suitable minima found by both optimizers for each optimization case is given in Fig. 4.10. In the well-posed cases, TTR tends to have better performance than *lsqnonlin*, with moderate advantages for Models A and D, and significant advantages for Model B and C.

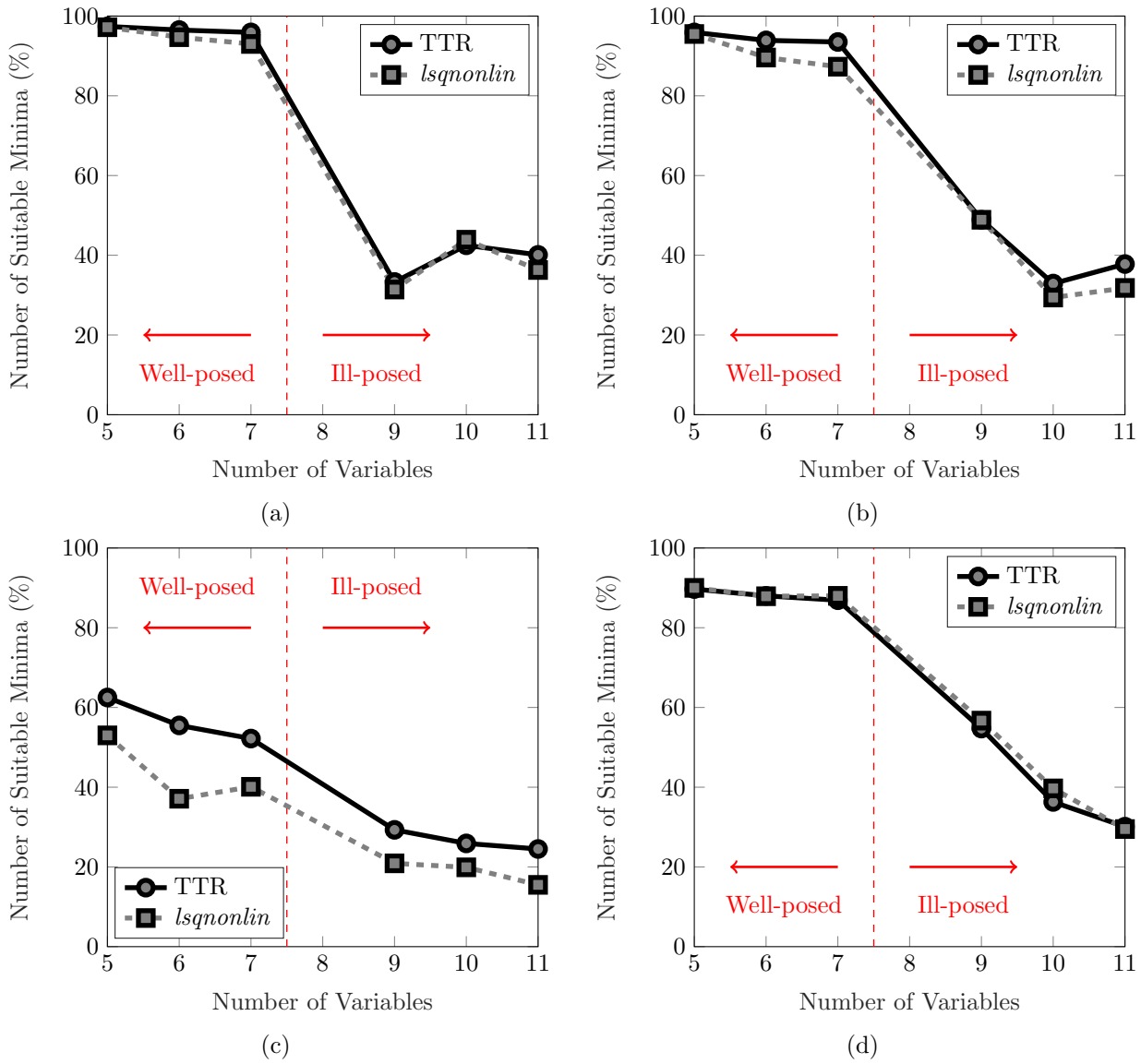

Figure 4.10. The percentage of $\boldsymbol{x}^*$ that were suitable minima at various optimization sizes for Models (a) A, (b) B, (c) C, and (d) D. Results are shown for the TTR and *lsqnonlin* algorithms. Each data point reflects a percentage of 1500 data points. For example, a value of 90% means 1350 of the 1500 LHS samples led to suitable minima.

In the ill-posed cases, however, the relative performance becomes closer. Beginning with Model A, the optimizers are effectively tied as neither convincingly outperforms the other, although TTR did obtain a slightly greater number of suitable minima for sizes 9 and 11. For Model B, TTR demonstrates a moderate advantage for converging to suitable minima over *lsqnonlin* for problem sizes of 10 and 11 variables. Furthermore, following the trend from the well-posed cases, TTR continues to outperform *lsqnonlin* in ill-posed optimization for Model C via consistently higher

numbers of suitable minima found. Finally for Model D, TTR ties *lsqnonlin* for optimization sizes of 9 and 10 variables, but notably outperforms it for the largest size of 11 variables. With the exception of Model A Case 5 (size 10), the tandem-trust region optimizer either tied or outperformed *lsqnonlin* overall for the simulated FWD backcalculation configurations. Overall, the TTR algorithm demonstrated a 13.5% higher reliability in ill-posed $|E^*|$ backcalculation than *lsqnonlin*.

4.4 Conclusions

4.4.1 Summary

The TTR optimization algorithm is developed, and its performance in dynamic FWD backcalculation is compared to that of custom STIR and LMA opimizers as well as a commercial alternative (MATLAB's *lsqnonlin*). Using a total of 36,000 initial guesses generated via Latin hypercube sampling, the optimization techniques are used to simulate six different backcalculation cases (corresponding to optimization sizes) across four different ViscoWave pavement models and three different Dynatest FWD load signals. The optimization sizes are strategically chosen to investigate the ill-posed nature of the optimization typical for modern FWD backcalculations. Additionally, a detailed demonstration of ill-posed backcalculation is presented, and a suitable minimum criterion is proposed based on the results to provide a practical assessment of the backcalculation quality.

In comparisons with its constituent STIR and LMA techniques, the TTR method is shown to consistently improve the performance in both minimizing the objective function and converging to suitable minima, demonstrating the benefits of a TTR step calculation approach. Compared to using the STIR or LMA methods alone, the tandem approach improved the reliability of ill-posed dynamic modulus backcalculation by 33.9% and 56.9%, respectively. Furthermore, the TTR optimizer demonstrated a 13.5% improvement over *lsqnonlin* in ill-posed backcalculation. Of all optimization methods tested, the TTR algorithm is the best to use for backcalculation of pavements with multiple viscoelastic layers.

The studies here are the first to deeply investigate the ill-posed nature of the nonlinear least-squares optimization in the context of dynamic FWD backcalculation. Modern flexible pavements typically comprise multiple sub-layers (or lifts) of distinct asphalt mixes; however, contemporary backcalculations are performed by aggregating them into a single layer in the computer model.

This approach circumvents the problems induced by the ill-posed optimization since it reduces the number of updating variables, but it precludes the ability to determine the *in situ* strength of the individual AC lifts. The TTR optimizer developed herein can be immediately used in FWD backcalculation techniques that use nonlinear least-squares minimization, and it is particularly useful in ill-posed backcalculation, which is common when the asphalt layer is modeled with multiple lifts. Additionally, TTR can potentially be used in TSDD backcalculation techniques due to their inherent similarity to FWD-based approaches.

4.4.2 Limitations

The material properties used for the pavement models in the performance tests were extrapolated from values common for Georgia, USA, which are not representative of the wide variety of flexible pavement materials used globally. Furthermore, the TTR algorithm has not been compared to other optimizers in applications other than FWD backcalculation. It is important to note the computational cost of using TTR is approximately double that of using either STIR or LMA. Therefore, it is intended to be used for situations where the computational expense attributed to the finite difference derivatives is significantly greater than that of the optimization.

Chapter 5

UGA-PAVE Validation

This chapter concerns the procedures and results of the UGA-PAVE validation. The data collection strategy is detailed first, after which two different validation studies are presented. The first study revolves around a traditional pavement design approach using layer coefficients. The second validation study employs a more modern approach which involves the dynamic modulus curve.

5.1 Data Collection

The methods of collecting the data for validating UGA-PAVE are discussed herein. Two sets of data were collected for the validation studies: a validation set and an experimental set. The validation set consists of lab-measured data that are considered the "truth" values, and the experimental set consists of the data output by UGA-PAVE to be appraised.

5.1.1 Validation Set

Asphalt coring was used to create the validation data set, whereby cylindrical samples, called asphalt cores, are extracted from the candidate pavement section. A list of the cores used for the validation studies is given in Table 5.1. All core samples were extracted from a state route in Georgia, USA, denoted by the number in the core name. An Asphalt Mixture Performance Tester (AMPT) device was used to determine the truth dynamic moduli of the pavement sections. Each pavement core contains a sample from the entire asphalt layer, which comprises multiple distinct lifts (*i.e.*, sub-layers) of different mixtures of asphalt concrete. To represent the asphalt layer with

high fidelity, a dynamic modulus curve should be determined for each lift. Apropos, the AMPT device determines the truth dynamic modulus of each distinct asphalt lift in an extracted core via cyclic loading tests conducted at different frequencies and temperatures.

Table 5.1. List of cores used for validation data set, including the total thickness and number of lifts in the asphalt concrete (AC) layer.

Core	AC Thickness (cm)	No. AC Lifts
GA-10A	27.62	3
GA-10B	29.84	2
GA-11	38.10	2
GA-22	34.92	5
GA-26	11.43	1
GA-57	19.05	2
GA-82A	21.59	2
GA-82B	22.22	2
GA-129	16.51	2

The AMPT procedure for determining dynamic modulus follows American Association of State Highway and Transportation Officials (AASHTO) testing protocol 107-18. First, two 38 mm diameter specimens are extracted from each distinct lift of the asphalt layer within the core. Then, each test specimen taken from the core is cyclically loaded at six different forcing frequencies: 0.1, 0.5, 1, 5, 10, and 25 Hz. These cyclic loading tests are conducted at three different temperatures for each specimen: 4, 20, and 40°C. Then, all measured data for the specimens from a given lift are shifted to a standard reference temperature of 21.1°C via time-temperature superposition shifting, which is detailed later in Section 5.2.1. Once shifted, a sigmoidal fitting function is applied, thereby producing the $|E^*|$ master curve for the asphalt lift. An example of AMPT-measured $|E^*|$ data is given in Fig. 5.1.

5.1.2 Experimental Set

The FWD test data were collected from the same locations where the pavement samples were extracted for AMPT testing. First the nondestructive FWD testing was performed, after which the asphalt core would be taken from the location and then transported for AMPT testing later.

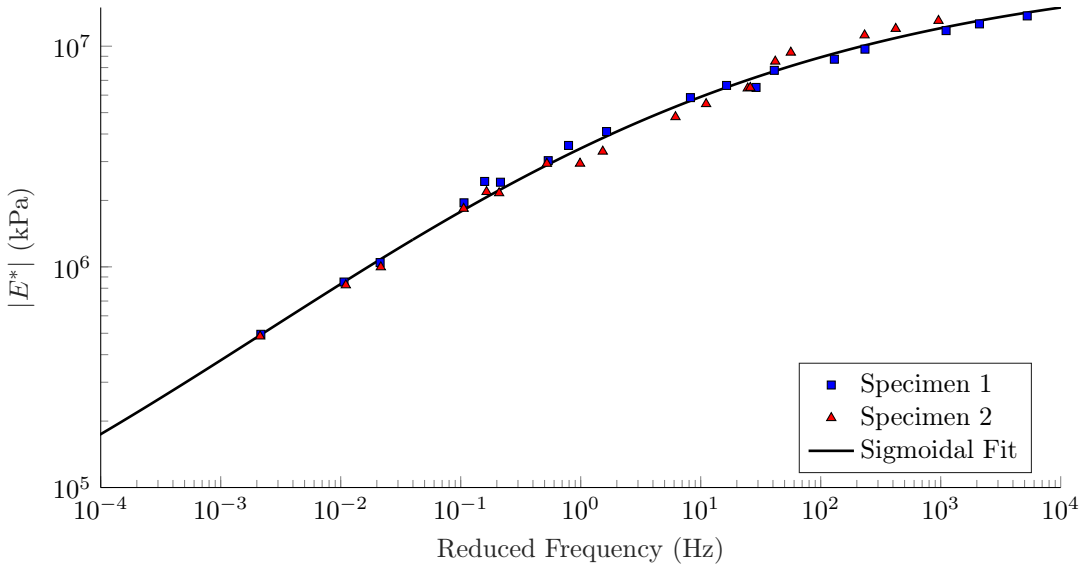

Figure 5.1. AMPT-measured dynamic modulus data for Specimen 1 (blue squares) and Specimen 2 (red triangles) from the first lift of Core GA-11. The sigmoidal fit (black line) is the dynamic modulus master curve.

The FWD experimentation used herein was conducted by the Georgia Department of Transportation (GDOT) using their standard operating procedure with a Dynatest FWD. Six FWD tests were conducted at each location, whereby three peak loads—27, 40, and 53 kN—are applied twice each. As the pavement is impacted, the surface deflections are measured by displacement sensors in a 60 ms time window at seven locations: 0, 20.32, 30.48, 45.72, 60.96, 91.44, and 152.4 cm from the load.

The backcalculations were conducted slightly differently in each validation study. For the first study involving layer coefficients, the pavement models comprise four layers: two asphalt at the top, an unbound aggregate base (UAB) layer in the middle, and a finite subgrade layer at the bottom. Following GDOT's standard procedure, two layer coefficients should be determined: one for the top 11.43 cm (4.5 inches) of asphalt, and the other for the remaining asphalt below 11.43 cm of depth. Concordantly, the asphalt layer in the pavement model is subdivided into two layers, thereby resulting in two backcalculated $|E^*|$ curves—one for each subdivision. The layer coefficients for both portions are then determined from the backcalculated $|E^*|$ curves and compared to the layer coefficients determined via AMPT testing. For the second study involving direct comparison of $|E^*|$ curves, the backcalculation models comprise three layers: one asphalt on top of an unbound aggregate base and a finite subgrade. Because the asphalt layer is modeled as a whole, each

backcalculation produces one $|E^*|$ curve. Consequently, an average of the $|E^*|$ curves obtained from the AMPT testing is calculated for comparison.

The general procedure for each backcalculation begins with setting initial guesses for the optimization variables, called the seed moduli. The variables in each optimization are as follows: the $|E^*|$ sigmoidal coefficients ($d_1 - d_4$), the elastic modulus of the UAB layer (E_{UAB}), and the elastic modulus (E_{sub}) thickness (h_{sub}) of the finite subgrade layer. Additionally, constant values for remaining pertinent material properties and geometry must also be set. The material property parameters include the densities of the asphalt, UAB, and subgrade layers (ρ_{AC}, ρ_{UAB}, ρ_{sub}) as well as their Poisson ratios (ν_{AC}, ν_{UAB}, ν_{sub}). The geometry constants for each model are the thicknesses of the asphalt and UAB layers (h_{AC} and h_{UAB}). The seed moduli and constant parameters values used in each backcalculation are given in Tables 5.2 and 5.3.

Slight variations were made to the sets of seed moduli and constants depending on the road. Two roads stand out as the most unique: GA-26 and GA-57. For GA-26, the UAB layer was assigned a starting modulus value several orders of magnitude higher than the other roads. This is because the pavement section consists of asphalt on top of a layer of Portland cement concrete (PCC) with subgrade below. Thus, E_{UAB} and ρ_{UAB} in the pavement model of GA-26 are set to typical values of PCC. Additionally, GA-57 was observed to consist of asphalt directly on top of subgrade soil; consequently, it was modeled without an unbound aggregate base layer between the asphalt and subgrade.

Table 5.2. Values used for the seed moduli (initial guesses) in the optimizations for each pavement section backcalculation.

Core	d_1	d_2	d_3	d_4	E_{UAB}	E_{sub}	h_{sub}
GA-10A	4.338	4.338	-1.5	0.5	0.1379	34.47	3.048
GA-10B	4.338	4.338	-1.5	0.5	0.1379	34.47	3.048
GA-11	4.338	4.338	-1	0.4	0.1379	34.47	1.524
GA-22	4.338	4.338	-1	0.4	0.1379	34.47	3.048
GA-26	4.338	4.338	-1	0.4	27.58	34.47	3.048
GA-57	4.338	4.338	-1	0.4	—	44.82	3.048
GA-82A	4.338	4.338	-1.5	0.5	0.1379	34.47	3.048
GA-82B	4.338	4.338	-1.5	0.5	0.1379	34.47	3.048
GA-129	4.338	4.338	-1.5	0.5	0.1379	34.47	3.048
Unit:	log(kPa)		—	—	GPa	MPa	m

Table 5.3. Values of the parameters kept constant during optimization for each pavement section backcalculation.

Core	h_{AC}	h_{UAB}	ρ_{AC}	ρ_{UAB}	ρ_{sub}	ν_{AC}	ν_{UAB}	ν_{sub}
GA-10A	27.62	25.4	2242	1922	1602	0.3	0.35	0.4
GA-10B	29.84	25.4	2242	1922	1602	0.3	0.35	0.4
GA-11	38.10	30.48	2242	1922	1121	0.3	0.35	0.35
GA-22	34.92	—	2242	—	1201	0.3	—	0.4
GA-26	11.43	15.24	2242	2322	1602	0.3	0.2	0.4
GA-57	19.05	—	2242	—	1201	0.3	—	0.4
GA-82A	21.59	25.4	2242	1922	1201	0.3	0.35	0.4
GA-82B	22.22	25.4	2242	1922	1201	0.3	0.35	0.4
GA-129	16.51	30.48	2242	1922	1602	0.3	0.35	0.4
Unit:	cm	cm	kg/m^3	kg/m^3	kg/m^3	—	—	—

5.2 Validation with Layer Coefficients

The first method for validating UGA-PAVE involves generating layer coefficients from the back-calculated dynamic moduli and compare with lab-tested values. The layer coefficients approach originates from the AASHTO 1972 pavement design guide [119] and involves assigning each type of material a value that reflects its strength per unit thickness. The coefficients are used to determine a pavement section's structural number (SN), which represents its overall strength. The SN of a pavement section is calculated by

$$SN = \sum_{i=1}^{n} a_i D_i, \tag{5.1}$$

where a_i and D_i are the layer coefficient and thickness of the i^{th} layer, respectively, and n is the number of pavement layers above the subgrade (*i.e.*, the natural earth layer).

5.2.1 Procedure

The layer coefficients approach used herein is based on the procedure used by GDOT, whereby two coefficients are used to describe the strength of the asphalt layer. The reasoning for this approach is that the pavement experiences different types of distresses at its surface and base. The first coefficient, a_+, relates to the uppermost 11.43 cm of asphalt, and the second, a_-, corresponds to the remaining asphalt below a depth of 11.43 cm. To clarify, the subscripts are used to identify which portion of the asphalt the coefficient corresponds to, with $\circ_+$ denoting "above" the 11.43 cm division and $\circ_-$ denoting "below" it.

Inspired by the procedures from other state departments of transportation (DOTs) in the USA [120–123], a third coefficient, a_*, is also calculated for the validation study, which is used to represent the entire asphalt layer. This coefficient is calculated by taking a thickness-weighted average of the subdivision coefficients, given by

$$a_* = \frac{a_+ h_+ + a_-(h_{\text{AC}} - h_+)}{h_{\text{AC}}}, \tag{5.2}$$

where h_+ is the thickness associated with a_+ (*i.e.*, the depth of the subdivision). When using GDOT's typical operating procedure, $h_+ = 11.43$ cm (4.5 inches). However, in the pavement

cores used for the present study, there was not always a division between distinct asphalt mixes at precisely a depth of 11.43 cm. Thus, the subdivision depths used to calculate a_+ and a_- slightly varied depending on the core. The values for h_+ were instead determined from the subdivision between two distinct asphalt lifts nearest to a depth of 11.43 cm.

A procedure from the 1993 AASHTO pavement design guide [124,125] is used to calculate layer coefficients from both lab-measured and backcalculated $|E^*|$ curves. In the approach, the layer coefficient can be calculated from a given a dynamic modulus value by

$$a = 0.171 \ln |E^*(f)| - 1.784, \tag{5.3}$$

where a is the layer coefficient, and $|E^*(f)|$ is the dynamic modulus (measured in psi) for a single loading frequency, f. One point that is not specified in the procedure is which loading frequency to use for the $|E^*|$ input. The dynamic modulus is a continuous function that varies with frequency; however, Eq. (5.3) is designed to consider the value at one frequency. Consequently, a single $|E^*|$ value must be determined which best represents the overall traffic loading. For the present study, a loading frequency of $f = 1$ Hz is used, which is approximately at the center of the typical range of frequencies on logarithmic scale (*i.e.*, 0.1 Hz to 25 Hz) used to represent dynamic modulus in MEPDG techniques.

The dynamic modulus value input to Eq. (5.3) should be from the master curve, which is typically created at a reference temperature of 21.1°C. The AMPT procedure automatically generates the $|E^*|$ master curve at a specified reference temperature; however, the FWD backcalculated dynamic modulus curves must be converted to the "reduced frequency" space, which corresponds to the master curve. This process is known as time-temperature superposition (TTS) shifting, whereby the $|E^*|$ curve corresponding to a given temperature can be shifted in the frequency domain, after which it represents the modulus at a different temperature. The TTS shift is based on the relationship

$$f_R = \beta(T) f_{\text{FWD}}, \tag{5.4}$$

where f_{FWD} is the frequency of a dynamic modulus data point measured at given temperature T, f_R is the corresponding reduced frequency of the dynamic modulus data point at the reference

temperature. The parameter $\beta(T)$ is the TTS shift factor, which depends on the temperature of the pre-shift $|E^*|$ curve, T. For example, if a dynamic modulus is backcalculated from a pavement at a temperature of 30°C during FWD testing, the frequency domain of the backcalculated $|E^*|$ curve should be multiplied by a factor of $\beta(T = 30°\text{C})$ to shift the curve to reduced frequency at the reference temperature. This procedure manifests as a horizontal shift to the curve. The most common approach for determining the shift factor is to create a TTS model for the specific type of asphalt concrete mixture being studied. In this study, the TTS models are all of the same form as in Eq. (3.82). The coefficients—α_1, α_2, and α_3—were determined individually for each pavement section as part of the the lab testing procedure, and are given in Table 5.4.

Table 5.4. Time-temperature superposition model coefficients determined via AMPT for the asphalt samples for the tested pavement sections. Coefficient values should be used in Eq. (3.82) with temperature, T, in degrees Celsius.

Road	α_1	α_2	α_3
GA-10A	0.0027	-0.2689	4.455
GA-10B	0.0046	-0.3721	4.918
GA-11	0.0037	-0.3125	4.920
GA-22	0.0030	-0.2789	4.575
GA-26	0.0021	-0.2172	3.653
GA-57	0.0047	-0.3807	5.936
GA-82A	0.0021	-0.2452	4.230
GA-82B	0.0023	-0.2282	3.793
GA-129	0.0020	-0.1304	2.669

5.2.2 Results

The layer coefficients determined from the AMPT-measured dynamic moduli are given in Table 5.5. Cores GA-82A and GA-82B are excluded from the results because they did not include distinct asphalt divisions near to a depth of 11.43 cm (5.72 cm and 6.35 cm, respectively); however, each of the remaining cores contained a division within 1.27 cm (0.5 inches) of the target depth of $h_+ = 11.43$ cm and are therefore included. Furthermore, layer coefficient a_- (and consequently a_*) was indeterminable for cores GA-26 and GA-129. In the case of GA-26, the pavement section comprised a single, 11.43 cm layer of asphalt on top of 17.78 cm of PCC, and thus only the a_+

coefficient could be calculated. On the other hand, the pavement layer of GA-129 was composed of two distinct asphalt lifts: 11.43 cm and 5.08 cm. However, both specimens extracted from the lower 5.08 cm layer experienced structural failure before they could be tested by AMPT, and no $|E^*|$ curve could be measured for lower asphalt lift.

Table 5.5. Layer coefficients and subdivision depths determined from AMPT-measured dynamic modulus.

Core	a_+	a_-	a_*	h_+ (cm)
GA-10A	0.49	0.58	0.54	12.70
GA-10B	0.54	0.55	0.55	10.16
GA-11	0.46	0.47	0.47	11.43
GA-22	0.51	0.45	0.47	12.70
GA-26	0.48	—	—	11.43
GA-57	0.54	0.54	0.54	10.16
GA-129	0.53	—	—	11.43

A statistical analysis of the AMPT-derived layer coefficients was conducted, and the results are provided in Table 5.6. From the analysis, it was determined that the average layer coefficient value was consistent for all three coefficient types, approximately between 0.51 and 0.52. However, there was variance in the coefficients among the individual mixes, with the most notable being a_-. To consider this variation, multiples of the standard deviation, σ, were subtracted from the mean, μ, to estimate the coefficients with a higher statistical reliability. For example, assuming the values of a_- are part of a normal distribution, subtracting two standard deviations ($\sigma = 0.0575$) from its mean ($\mu = 0.5203$) yields a value of $a_- = 0.4063$ with 97.8% confidence. In other words, it can be expected that $a_- \geq 0.41$ for 97.8% of *in situ* asphalt pavements in Georgia, USA. For reference, GDOT currently uses $a_+ = 0.44$ and $a_- = 0.33$ for its layer coefficients.

Additionally, results for the coefficient representing the entire asphalt layer agree well with similar studies conducted by other state DOTs. In 2009, a study conducted by the Alabama DOT [122] recommended a value of $a_* = 0.54$ for hot mix asphalt, and in 2019, a study sponsored by the Florida DOT [123] determined $a_* = 0.54$ is satisfactory for modern high polymer asphalt mixtures. Most recently, a study by the New Hampshire DOT [126] concluded that $a_* = 0.41$ is

Table 5.6. Statistics of AMPT-derived layer coefficients. Values are rounded based on industry practice.

Statistic	a_+	a_-	a_*	Reliability
σ (Std. Dev.)	0.032	0.057	0.041	—
μ (Mean)	0.51	0.52	0.51	50%
$\mu - \sigma$	0.48	0.46	0.47	84.2%
$\mu - 2\sigma$	0.44	0.41	0.43	97.8%

satisfactory for hot mix asphalt, increased from the department's previous values ranging between 0.34–0.38.

Table 5.7 contains the layer coefficients determined from the FWD data collected from the locations where the cores were extracted for AMPT testing. Backcalculation results which correspond to cores GA-82B and GA-129 are excluded because they failed to reach an acceptable error tolerance of 0.129 mm^2 (200 $mils^2$). The errors of each backcalculation were calculated as the sum of squared errors between the seven measured (by FWD) and predicted (by UGA-PAVE) across 300 time points in the time window, and the tolerance value was determined by manual visual inspection to be the threshold where the two sets of deflections become too dissimilar. Note that the values of h_+ from Table 5.5 are used to subdivide the asphalt layer in each of the forward models for backcalculation.

Table 5.7. Layer coefficients determined from FWD-backcalculated dynamic modulus.

Core	a_+	a_-	a_*
GA-10A	0.68	0.32	0.50
GA-10B	0.53	0.45	0.49
GA-11	0.48	0.43	0.46
GA-22	0.59	0.44	0.52
GA-26	0.83	0.47	0.65
GA-57	0.21	1.03	0.62
GA-82A	0.16	0.84	0.50
Mean:	0.50	0.57	0.53
Std. Dev.:	0.24	0.26	0.07

Large standard deviations are seen in the FWD backcalculated values of a_+ and a_-; however, the variance of the full-depth coefficient, a_*, is significantly lower. This outcome can be explained by the compensating layer effect (CLE) [127], whereby the individual contributions of the moduli of various layers are erroneous yet lead to a feasible stiffness when aggregated. The results for GA-82A demonstrate the CLE well, where both a_+ and a_- are impractical. The value for a_+ is unusually low, being in the range of a pavements with considerable distresses at the surface; however, no such damage was observed by the field engineers when collecting the FWD data and pavement core from the location. Furthermore, a_- is remarkably high, beyond a feasible value for the asphalt mixtures typically used by GDOT. However, the resulting a_* yields a practical value because the weighted average aggregates the stiffnesses of both asphalt layers in the forward model, thereby mitigating CSE. Other notable examples are GA-10A, GA-26, and GA-57.

Because of the compensating layer effect, comparison of the AMPT-measured and FWD-backcalculated layer coefficients is limited to the averaged coefficient, a_*. The coefficients determined from the experimental and validation data sets are compared in Table 5.8. Note that a_* values could not be calculated from the AMPT measurements for cores GA-26, GA-82A, GA-82B, and GA-129; similarly, FWD backcalculated results for GA-82B and GA-129 are excluded because their backcalculations failed to converge below an error of 0.129 mm^2.

Table 5.8. Comparison of thickness-weighted average layer coefficients determined from AMPT-measured and FWD-backcalculated dynamic modulus. AMPT results for cores GA-26, GA-82A, GA-82B, and GA-129 are excluded because a_* values could not be calculated for them. Additionally, FWD results are excluded for cores GA-82B and GA-129 because their backcalculations failed to reach a satisfactory error threshold.

Core	a_* (AMPT)	a_* (FWD)	Rel. Diff.
GA-10A	0.54	0.50	7.7%
GA-10B	0.55	0.49	11.5%
GA-11	0.47	0.46	2.2%
GA-22	0.47	0.52	10.1%
GA-26	—	0.65	—
GA-57	0.54	0.62	13.8%
GA-82A	—	0.50	—
Mean:	0.51	0.53	9.06%
Std. Dev.:	0.041	0.072	4.43%

General agreement can be seen between the AMPT and FWD methods, which have similar mean values of 0.51 and 0.53, respectively. The average relative difference among each testing method was 9.06%, with the smallest being GA-11 at 2.2% relative difference and the largest occurring with GA-57 at a 13.8% relative difference. These results show promising agreement between the FWD and AMPT methodologies, suggesting that FWD backcalculation may be a suitable replacement to coring/AMPT testing in layer-coefficient-based approaches for flexible pavements. However, the FWD backcalculated results had a notably higher standard deviation, which suggests the approach is more likely to over- or under-approximate layer coefficients compared to AMPT. Additionally, the compensating layer effect introduces issues for determining a_+ and a_-; thus, FWD backcalculation is only suitable for calculation of the full-depth layer coefficient, a_*.

5.3 Validation with Dynamic Modulus

In this study, the dynamic modulus curves determined from AMPT testing and FWD backcalculation are directly compared. Pertinent aspects of the procedure used for the analysis are first covered, followed by the results of the comparisons for each pavement section.

5.3.1 Procedure

As discussed in Section 4.1.2, falling weight deflectometers cannot impart a perfect impulse load on the pavement. Consequently, only a limited range of frequencies are excited in an FWD test, referred to as the effective frequency range (EFR) [101]. During the backcalculation process, contributions from frequencies outside the EFR are extrapolated from trends within the EFR; apropos, the analysis here is constrained to comparing the dynamic modulus curves within the EFR, and content outside the range is ignored.

The EFR bounds are calculated individually for each FWD test. First, the time history of the FWD load is converted to the frequency domain using the fast Fourier transform (FFT). The resolution of the resulting frequency signal is used as the lower bound, which is equal to the inverse of the time window. For example, if the time history window is 60 ms, then the lower bound is taken as 16.7 Hz. Then, the upper bound is determined from the lowest frequency to the right of the peak where the signal is less than or equal to 1% of its maximum (typically between 100 and

200 Hz). Once the bounds of the EFR are identified for the FWD test, they are converted to the reduced frequency domain at a reference temperature of 21.1°C via time-temperature superposition (see Sections 3.3 and 5.2.1). The TTS models used to shift the frequencies of each FWD test are taken from the AMPT-measured values in Table 5.4.

5.3.2 Results

First, the $|E^*|$ curves are determined for the validation data set. Recall that specimens from multiple lifts of asphalt were tested via AMPT for each core, with the exception of GA-26 (one axphalt lift overlaying PCC), as well as GA-82A and GA-129 (failure in specimens taken from lower asphalt lifts). Thus, more than one $|E^*|$ curve will be determined for each core with multiple asphalt lifts. For this validation study, the average of these $|E^*|$ curves will be used to compare to the FWD backcalculated results. The $|E^*|$ sigmoidal coefficients for each core obtained from AMPT testing are given in Table 5.9. Because each core comprises multiple lifts of distinct asphalt mixtures, the tabulated coefficients are the averages of all measured $|E^*|$ from the given core.

Table 5.9. Average dynamic modulus sigmoidal coefficient values of all asphalt lifts for each core determined from AMPT testing.

Core	d_1	d_2	d_3	d_4
GA-10A	4.038	4.190	-1.5	-0.4131
GA-10B	4.038	4.326	-1.281	-0.3937
GA-11	4.038	4.288	-0.9906	-0.4051
GA-22	4.126	4.042	-1.172	-0.4043
GA-26	4.038	4.106	-1.274	-0.3463
GA-57	4.038	4.274	-1.305	-0.3936
GA-82A	4.038	4.102	-1.423	-0.3256
GA-82B	4.038	4.140	-1.226	-0.3227
GA-129	4.038	3.984	-1.769	-0.5071
Unit:	log(kPa)		—	—

Note that for most cores $d_1 = 4.038$ log(kPa), which corresponds to the minimum value of $|E^*|$ as $f_R \to 0$ (see Figure 4.1). This common value is due to the sigmoidal fitting strategy used. The AMPT device tests each specimen over a limited range of frequencies, with the lowest being 0.1 Hz. After all the test data at different temperatures are shifted to reduced frequency at the reference

temperature, the lowest frequency data points are typically near $f_R = 10^{-3}$ Hz; however, the lower asymptote of the sigmoid is often observed at frequencies several orders of magnitude lower (*e.g.*, $f_R \leq 10^{-6}$ Hz). This is demonstrated in Fig. 5.1, where the lowest data point is between 10^{-3} and 10^{-2} Hz, but the lower asymptote of the sigmoid occurs below 10^{-4} Hz. The regression procedure to fit the sigmoidal function to the test data is performed via an optimization routine with bounds on each coefficient; because there is a lack of data points in the extremely low frequency regime, the routine frequently converges to a solution where d_1 is equal to its lower bound in the optimization. Despite this phenomenon, the value of d_1 rarely has significant effect on the shape of the sigmoid within the EFR, which is the regime used for the following comparisons.

The dynamic modulus curves obtained from AMPT testing and FWD backcalculation are plotted for each core/location in Figs. 5.2–5.10. In each figure, the backcalculated $|E^*|$ from FWD data is plotted in blue, and the individual $|E^*|$ curves determined for each lift via AMPT (when applicable) are plotted with dotted lines and their averages in red. Additionally, the bounds of the EFR are denoted by dashed green lines. The backcalculated $|E^*|$ curves for GA-10A, GA-10B, GA-11, and GA-22 agreed well with their corresponding AMPT averages, having percent differences within the EFR of 4.33%, 8.27%, 10.75%, and 9.54%, respectively. However, the results for the remaining cores (GA-26, GA-57, GA-82A, GA-82B, and GA-129) exhibited poor matching, with percent differences of 49.46%, 49.97%, 75.5%, 66.61%, and 62.17%.

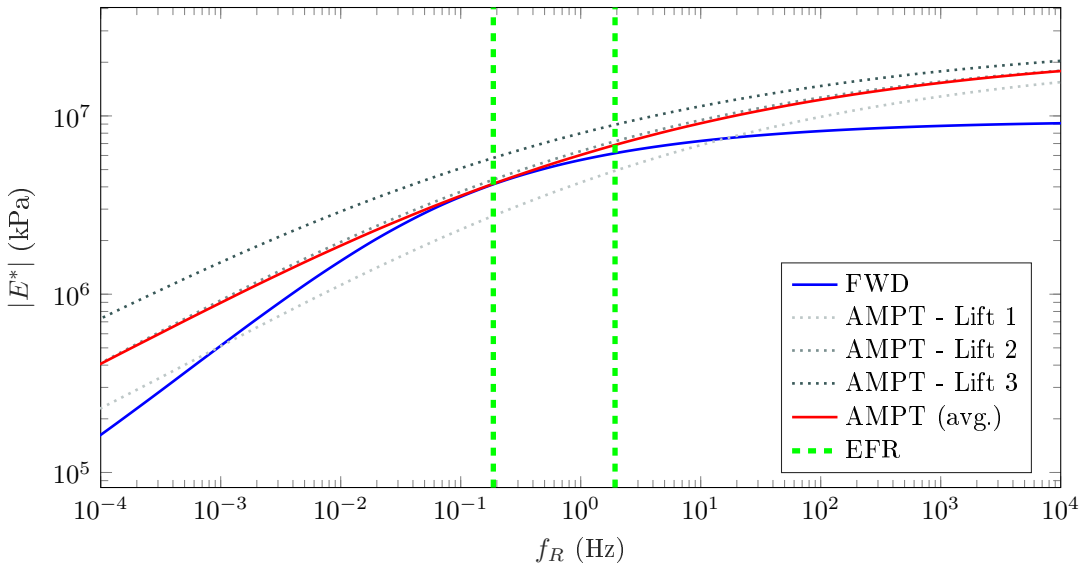

Figure 5.2. Comparison of AMPT-measured and FWD-backcalculated dynamic modulus curves for Core GA-10A. The region between the dashed green lines denotes the effective frequency range (EFR) for the backcalculated result, which is based on the pavement temperature during FWD testing.

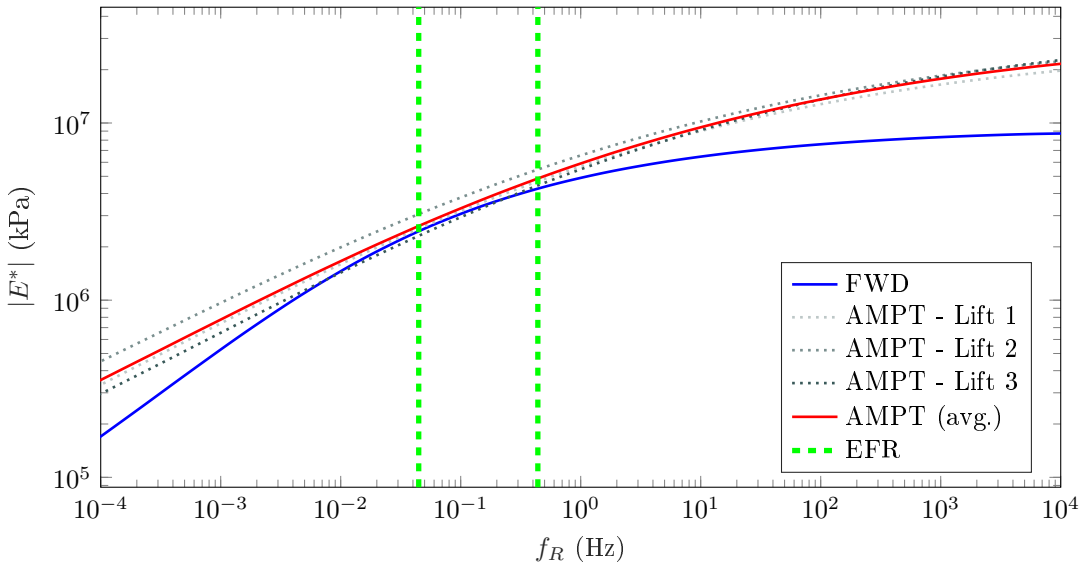

Figure 5.3. Comparison of AMPT-measured and FWD-backcalculated dynamic modulus curves for Core GA-10B. The region between the dashed green lines denotes the effective frequency range (EFR) for the backcalculated result.

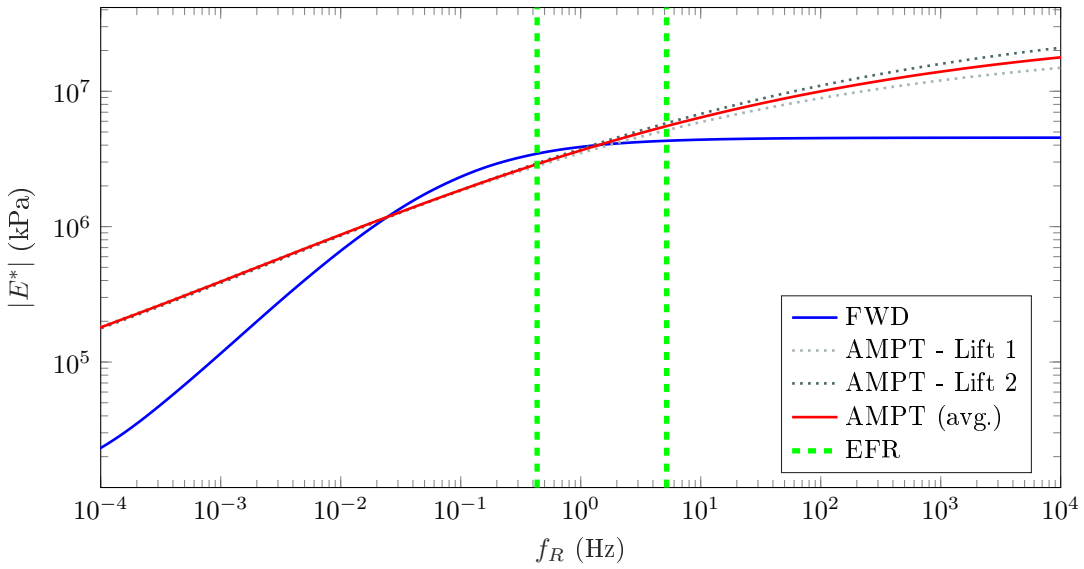

Figure 5.4. Comparison of AMPT-measured and FWD-backcalculated dynamic modulus curves for Core GA-11. The region between the dashed green lines denotes the effective frequency range (EFR) for the backcalculated result.

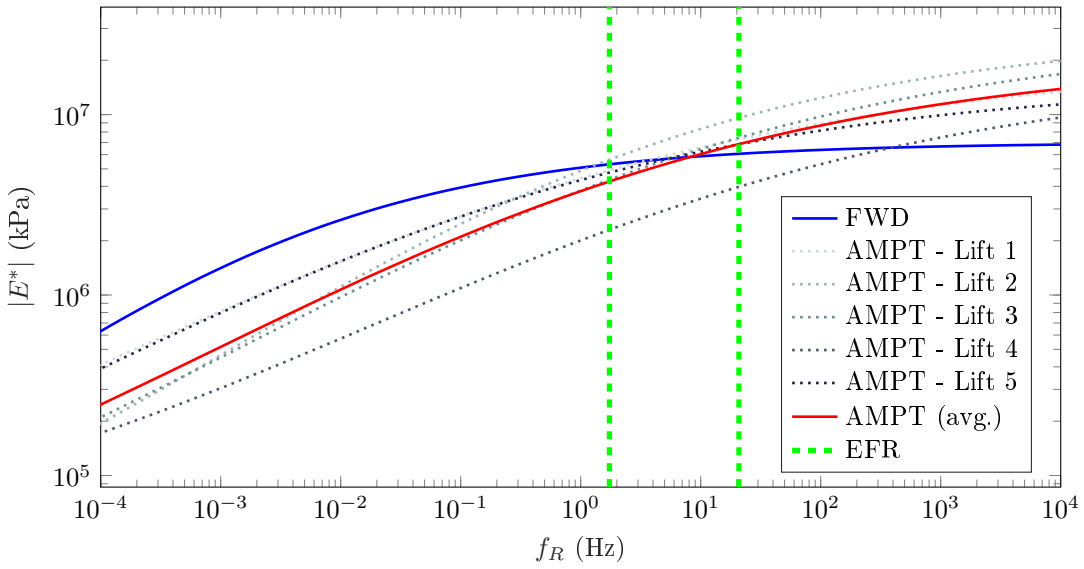

Figure 5.5. Comparison of AMPT-measured and FWD-backcalculated dynamic modulus curves for Core GA-22. The region between the dashed green lines denotes the effective frequency range (EFR) for the backcalculated result.

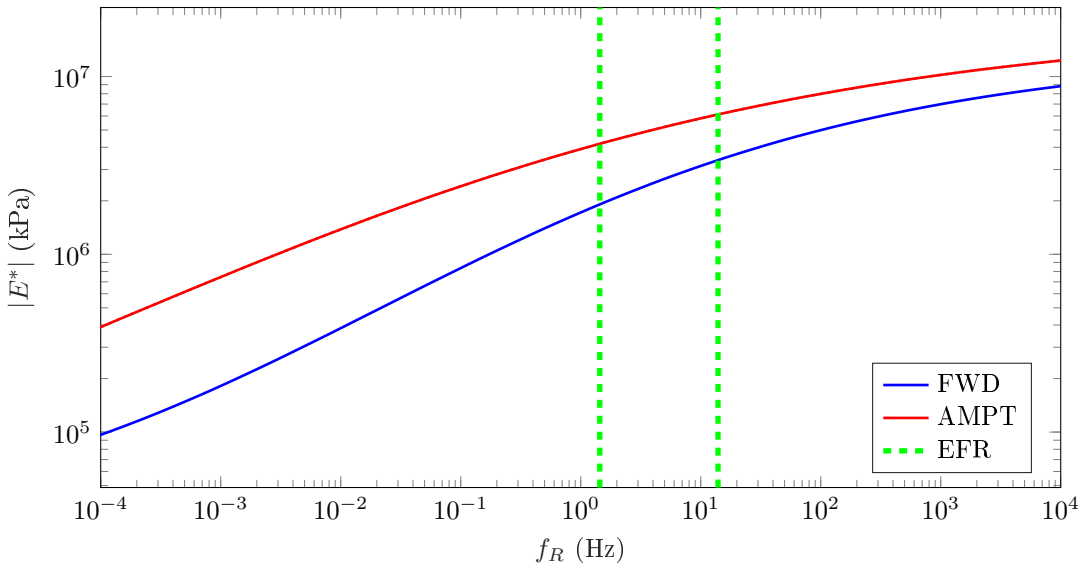

Figure 5.6. Comparison of AMPT-measured and FWD-backcalculated dynamic modulus curves for Core GA-26. The region between the dashed green lines denotes the effective frequency range (EFR) for the backcalculated result.

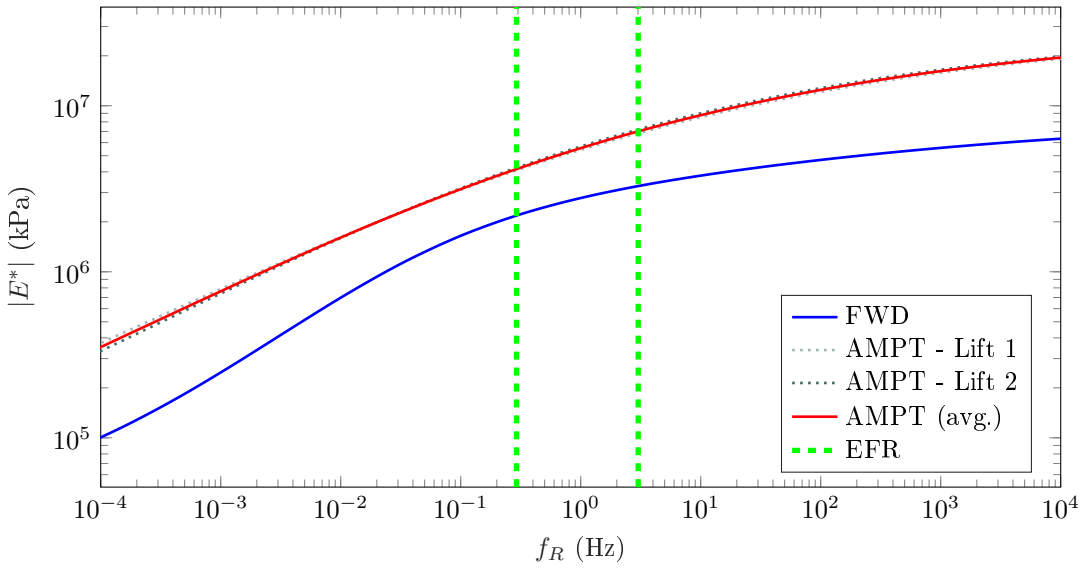

Figure 5.7. Comparison of AMPT-measured and FWD-backcalculated dynamic modulus curves for Core GA-57. The region between the dashed green lines denotes the effective frequency range (EFR) for the backcalculated result.

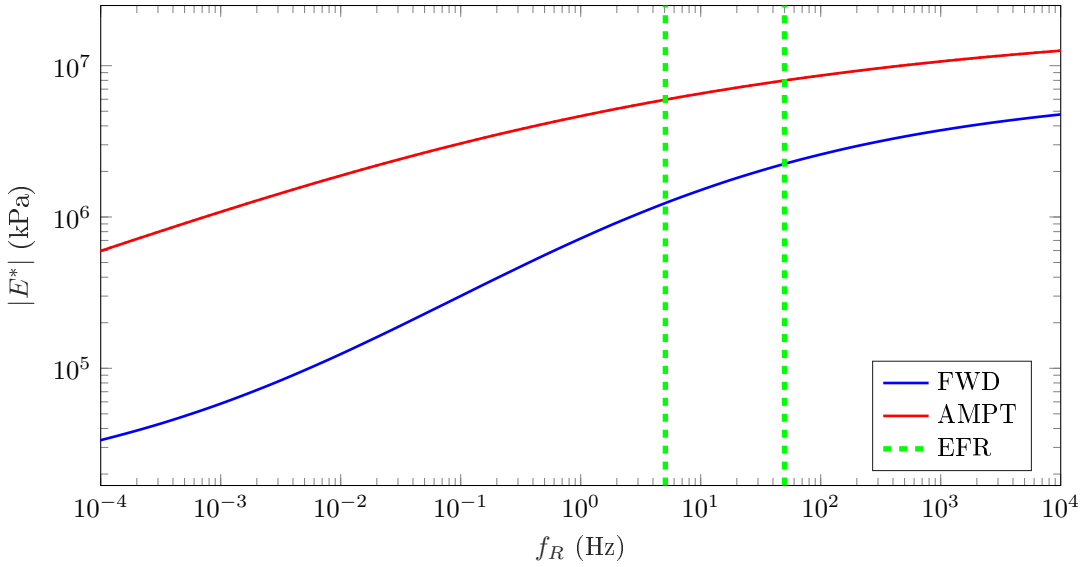

Figure 5.8. Comparison of AMPT-measured and FWD-backcalculated dynamic modulus curves for Core GA-82A. The region between the dashed green lines denotes the effective frequency range (EFR) for the backcalculated result.

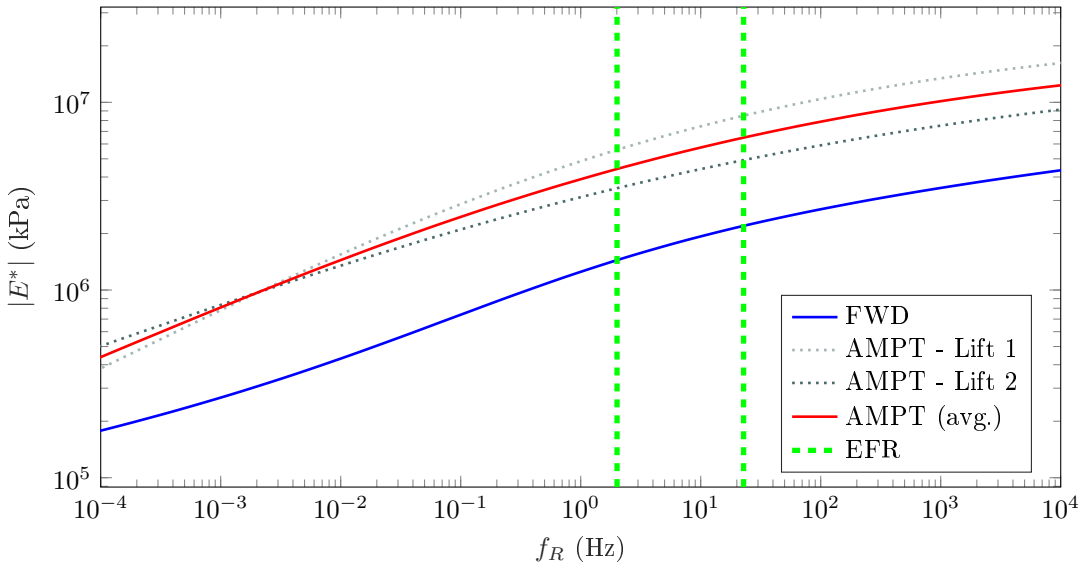

Figure 5.9. Comparison of AMPT-measured and FWD-backcalculated dynamic modulus curves for Core GA-82B. The region between the dashed green lines denotes the effective frequency range (EFR) for the backcalculated result.

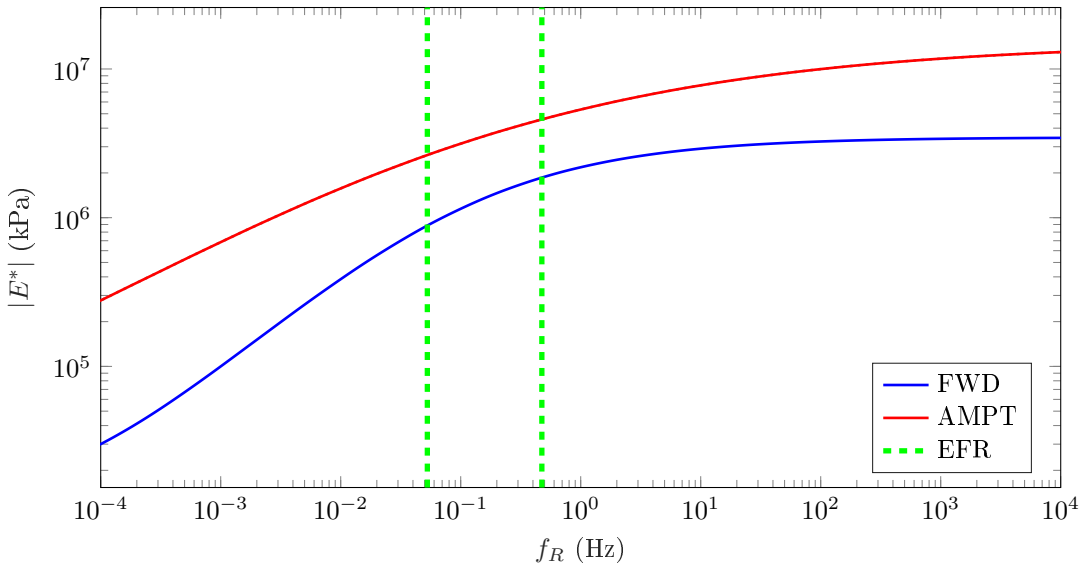

Figure 5.10. Comparison of AMPT-measured and FWD-backcalculated dynamic modulus curves for Core GA-129. The region between the dashed green lines denotes the effective frequency range (EFR) for the backcalculated result.

The backcalculation effectiveness varied considerably among the tested pavements, and they are attributed to two primary root causes. First, it is possible that certain types of distresses were present which can affect the structure's response during an FWD test (*e.g.*, bottom-up fatigue cracking, erosion of the aggregate base layer, subgrade damage) but do not affect the structural integrity of the specimens extracted for AMPT testing. In such a scenario, the dynamic modulus obtained from AMPT data is likely to be significantly higher than that obtained via FWD backcalculation, because the distress(es) will reduce the pavement section's stiffness in aggregate, but it will not not necessarily affect the integrity of the specimens extracted from the core for AMPT testing.

The second possible cause is a lack of sufficient knowledge pertaining to the foundation layer properties—namely the densities, Poisson ratios, and elastic moduli of the UAB and subgrade layers. For instance, if during FWD backcalculation the foundation layers are modeled with density and/or elastic modulus values that are significantly higher than in actuality, the backcalculated dynamic modulus of the asphalt layer will likely be erroneously lower due to the compensating layer effect.

5.4 Conclusions

5.4.1 Summary of Layer Coefficients Analysis

A layer coefficients analysis was conducted using dynamic modulus data of nine hot mix asphalt cores extracted from pavements in Georgia, USA. Three types of layer coefficients were considered. The first two, a_+ and a_-, are inspired by standard procedures of GDOT and correspond to asphalt lifts above and below a target depth of 11.43 cm, whereas the third type, a_*, represents the asphalt layer as a whole.

A statistical analysis of layer coefficients derived from AMPT testing was conducted to identify three reliability levels: 50%, 84.2%, and 97.8%. Afterward, layer coefficients were calculated from FWD backcalculated dynamic modulus data collected at the same locations where cores were extracted for AMPT testing, and the FWD-derived layer coefficients were compared to the results from AMPT. On average, there was good agreement between the layer coefficients derived between AMPT and FWD methodologies, having mean a_* values of 0.51 and 0.53, respectively. Additionally, the AMPT and FWD a_* values were compared on a per-core basis and exhibited an average relative difference of 9.06%.

Results suggest FWD backcalculation may be a suitable replacement for AMPT testing for design analyses based on layer coefficients. However, FWD backcalculation was observed to have erroneous results for a_+ and a_- due to an issue known as the compensating layer effect. Consequently, only a_* should be considered when performing a layer-coefficient-based design using FWD backcalculated data.

5.4.2 Summary of Dynamic Modulus Analysis

In a separate study, the dynamic modulus results from FWD backcalculation and AMPT testing were directly compared for the nine hot mix asphalt samples. The dynamic modulus mastercurve was computed from both approaches; however, the mastercurves derived from FWD backcalculation were approximated from time-temperature superposition models obtained from a database of HMA materials collected from a previous internal research study (see [5]). The dynamic modulus comparisons were limited to the effective frequency range, which is a limitation of the FWD

methodology arising from the fact that the force pulse only excites a narrow range of frequencies (approx. 10 to 100 Hz). The EFR of the dynamic modulus mastercurve is different for each comparison because the FWD tests were conducted at different temperatures; the shifted position can be calculated from the time-temperature superposition model used to construct the mastercurve.

Good agreement was observed for four of the pavement samples, with all being below 11% average difference between the dynamic moduli obtained from AMPT and FWD within the EFR. However, in each case the backcalculated $|E^*|$ significantly deviated from AMPT-derived modulus. The results serve as strong supporting evidence that the FWD backcalculation is only reliable for a narrow range of frequencies. Specifically, to compute $|E^*|$ outside the EFR, the backcalculation algorithm extrapolates from results within the EFR, which is often erroneous.

For the remaining five cores, poor agreement was observed between the AMPt and FWD methodologies, and two potential root causes were identified. The first is the possibility of unknown distresses being present underneath location of the FWD testing. In each case of poor agreement, the FWD-backcalculated modulus was significantly lower than its AMPT-measured counterpart. Thus, the presence of pavement distresses can act to decrease the dynamic modulus backcalculated from FWD. Second, there was a lack of knowledge of the material types underneath the asphalt layer in the pavement sections with poor agreement. The lack of knowledge precludes accurate estimation of material properties in the aggregate base and subgrade soil layers, such as elastic modulus, density, and Poisson ratio. Thus, properties and thicknesses were assumed for the problematic backcalculation analyses that likely differ from the actual pavement configurations.

Chapter 6

Improvements to FWD Testing Methodology

The falling weight deflectometer has been used for nondestructive pavement evaluation for more than half a century. Significant effort has been applied toward improving the backcalculation methodology, but the FWD test procedure has remained largely unchanged since its introduction. As a result, issues arising from the test configuration, such as ill-posedness and effective frequency range, continue to hinder backcalculation accuracy.

In this chapter, results from 720,000 unique simulated backcalculations are analyzed to investigate variations in the fundamental characteristics of the FWD test setup, namely the load shape, magnitude, and duration as well as the number of displacement sensors. The procedure for simulating FWD backcalculation is outlined in Section 6.1, results from the simulations are discussed in Section 6.2, and conclusions and limitations of the investigations are given in Section 6.3. This study is presented from a theoretical backcalculation perspective, meaning that practical issues arising in practice (*e.g.*, noise, measurement error) are not considered during analysis. The aim of the investigations conducted here is to deduce general trends that can be referenced in the future design of FWD testing equipment.

6.1 Simulation Procedure

6.1.1 Load Characteristics

Two types of impact load shapes are generated for the simulations. The first type is denoted as Typical and reflects the usual shape of an FWD impact, whereas the second is classified as Simple and is more akin to the standard impulse shape as used in the context of experimental modal analysis. The Typical type is characterized by a double-peak shape, whereas the Simple type has only a single peak.

Additionally, five different load magnitudes are considered: 26.7, 40, 53.4, 66.7, and 80.1 kN. In the ViscoWave models, the simulated deflections are linearly proportional to the load magnitude via a 1:1 relationship; for example, doubling the load magnitude results in a twofold increase in the peak deflection response. Thus, the different magnitudes used here are not intended to study differences in the pavement's dynamic response to different magnitudes. Instead, they are used to investigate the backcalculation algorithm's sensitivity to load magnitude.

Every force signal used hereon has a 5 ms onset delay and is generated for a 60 ms time window and a sampling rate of 20 kHz (1200 time points per signal). Three pulse durations, or pulse widths, are tested: 20, 30, and 40 ms. The width of the pulse load has a significant effect on the spectrum of excited frequencies. Generally, narrower pulses excite a larger range of loading frequencies. Of the force characteristics examined, the pulse width is perhaps the most pertinent because it directly affects the effective frequency range.

The force signals used in the simulated backcalculations were created synthetically to guarantee similarity between the various characteristics. Pulses are generated with the Typical and Simple shapes via the expressions

$$\begin{aligned} F(t) = {} & 0.457P\left(1-\cos\left(\frac{2\pi}{T}(t-t_i)\right)\right)\Big(H(t-t_i)-H(t-t_i-T)\Big) \\ & + 0.1693P\left(0.91-\cos\left(\frac{4\pi}{T}(t-t_i)+\frac{\pi}{7.9}\right)\right)\Big(H(t-t_i)-H(t-t_i-T)\Big), \end{aligned} \tag{6.1}$$

$$F(t) = 0.5P\left(1-\cos\left(\frac{2\pi}{T}(t-t_i)\right)\right)\Big(H(t-t_i)-H(t-t_i-T)\Big), \tag{6.2}$$

where P is the magnitude of the pulse, T is the duration, t_i is the onset time, and $H(t)$ is the Heaviside step function. Example Typical and Simple pulses are plotted in the time and frequency domains in Fig. 6.1 for $P = 40$ kN and $T = 30$ ms.

6.1.2 Pavement Models

Four ViscoWave models are synthesized for the studies. They are denoted A, B, C and D, and they have the same general structure as outlined in Fig. 4.4. The material properties of each model are detailed in Table 6.1. The overall percent material damping, ζ, is varied slightly between models. The sigmoidal coefficients for $|E^*|$ are taken from the database of hot mix asphalt samples measured by Kim *et al.* [5], and the remaining material properties reflect typical values found in Georgia, USA. Example deflections are plotted in Fig. 6.2 for each model in response to a Typical pulse shape with $P = 40$ kN and $T = 30$ ms.

6.1.3 Optimization Bounds and Samples

The parameter bounds are the same for all backcalculation simulations and are given in Table 6.2. One set of seed moduli (*i.e.*, initial guesses for the optimization) is used across all studies. The set comprises $2,000$ points generated via Latin Hypercube sampling (LHS) based on the parameter space enclosed by the optimization bounds. The LHS algorithm is outlined by Giunta *et al.* [118] and produces a near-uniformly distributed sampling of values for each variable. Each optimization involves 11 updating variables: two sets of d_1, d_2, d_3, and d_4 (one per asphalt layer), E_3 to represent an aggregate base layer, and E_4 and h_4 to represent a finite-thickness subgrade layer.

6.1.4 Testing Groups

Six Testing Groups are devised to investigate different backcalculation configurations via different quantities of sensors and different pulse shapes; the details of each Testing Group are given in Table 6.3. A backcalculation is performed for every combination of model, load magnitude, pulse width, LHS sample, and Testing Group configuration, totaling 720,000 unique backcalculation simulations (120,000 per Testing Group). All backcalculations are conducted with the UGA-PAVE software described in Chapter 3. Up to 12 deflection sensors are simulated for each Testing Group. For Group 6, which uses all 12, the sensors are located at 0, 20.3, 30.5, 45.7, 61.0, 91.4, 121.9, 152.4,

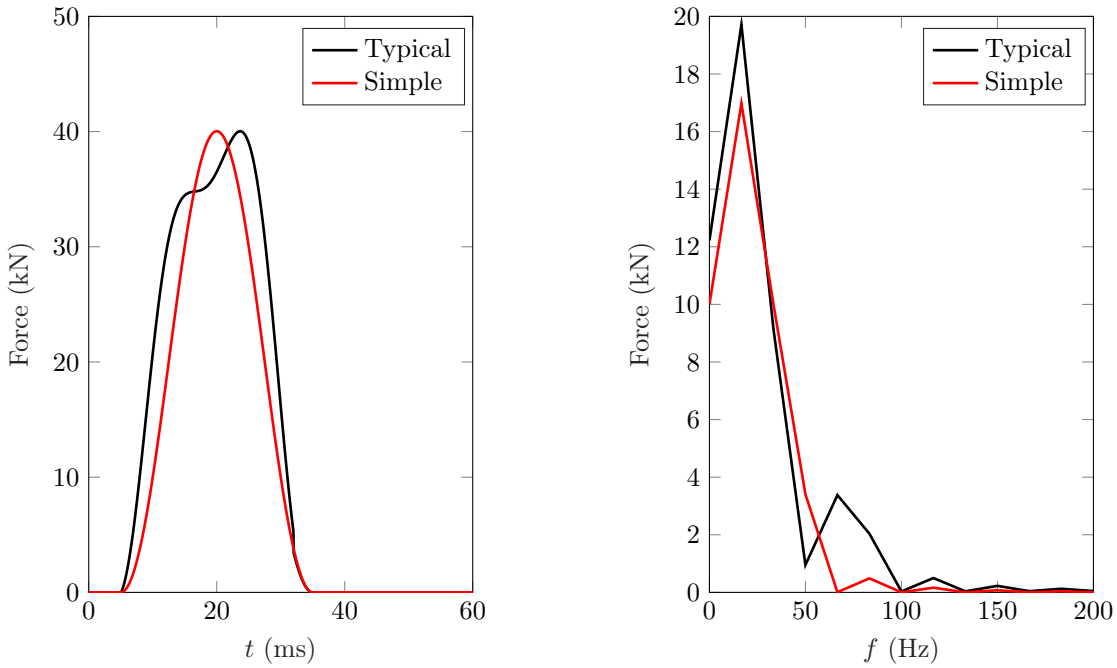

Figure 6.1. Plots of (a) Typical (black) and Simple (red) pulses in the time domain for $P = 40$ kN and $T = 30$ ms and (b) the signals converted to the frequency domain via the fast Fourier transform.

Table 6.1. Pavement layer moduli values used to generate the four ViscoWave models for the simulated FWD backcalculations. Sigmoidal coefficients (*i.e.*, d_1—d_4) are in units of log(kPa).

Model	Layer	d_1	d_2	d_3	d_4	E (MPa)	ρ (kg/m^3)	ν	h (cm)	ζ (%)
A	AC1	4.3730	2.9887	-0.5495	0.4880	–	2082.6	0.35	3.175	0.3
	AC2	4.9160	2.4438	-0.8724	0.5420	–	2082.6	0.35	8.890	
	GAB	-	-	-	-	132.3	1842.3	0.40	30.48	
	Subgrade	-	-	-	-	32.89	1441.8	0.45	967.2	
B	AC1	4.2430	3.1281	-0.5336	0.4640	–	2082.6	0.35	10.80	0.18
	AC2	4.7340	2.6371	-0.8207	0.5090	–	2082.6	0.35	20.00	
	GAB	-	-	-	-	157.7	1842.3	0.40	30.48	
	Subgrade	-	-	-	-	57.46	1441.8	0.45	656.8	
C	AC1	4.0630	3.3025	-0.7119	0.4800	–	2082.6	0.35	6.985	0.07
	AC2	4.2250	3.1424	-0.9206	0.4390	–	2082.6	0.35	13.34	
	GAB	-	-	-	-	224.0	1842.3	0.40	30.48	
	Subgrade	-	-	-	-	65.64	1441.8	0.45	801.1	
D	AC1	4.3730	2.9887	-0.5495	0.4880	–	2082.6	0.35	13.97	0.13
	AC2	4.5670	2.7909	-1.1085	0.4880	–	2082.6	0.35	21.59	
	GAB	-	-	-	-	199.8	1842.3	0.40	30.48	
	Subgrade	-	-	-	-	85.63	1441.8	0.45	751.8	

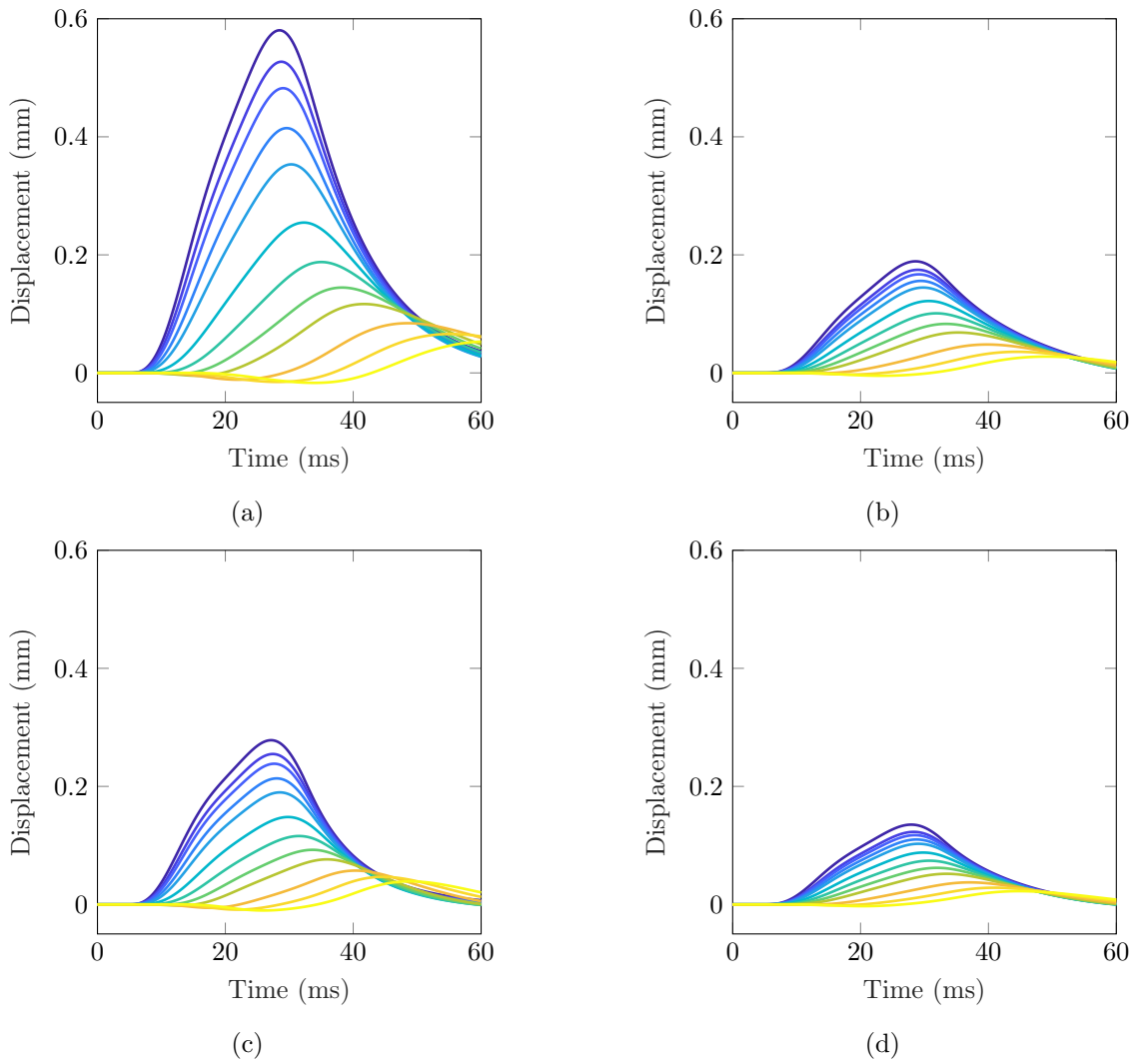

Figure 6.2. Deflection responses of ViscoWave Models (a) A, (b) B, (c) C, and (d) D when excited by a Typical pulse shape with a magnitude of $P = 40$ kN a pulse duration of $T = 30$ ms. Twelve deflection sensors are simulated; dark blue lines represent the sensor at the load point, and yellow lines denote the farthest sensor located 365.8 cm from the load point.

Table 6.2. Latin Hypercube sampling bounds for seed moduli.

Parameter	Units	Lower Bound	Upper Bound
d_1	log(kPa)	2.3385	4.8385
d_2	log(kPa)	1.5	5
d_3	—	-2	-0.1
d_4	—	0.1	1
E_3	MPa	68.95	517.1
E_4	MPa	6.895	137.9
h_4	m	0.9144	30.48

182.9, 243.8, 304.8, and 365.8 cm radially from the load point; for the five other Testing Groups, the first n_s sensor locations are used, where n_s is the number of sensors given in Table 6.3.

Table 6.3. Testing Group configurations for backcalculation simulations. In each group, backcalculations are conducted for all combinations of models, load magnitudes, and pulse widths.

Testing Group	Pulse Shape	Number of Sensors (n_s)	Optimization Structure
1	Typical	7	Ill-posed
2	Simple	7	Ill-posed
3	Typical	9	Ill-posed
4	Simple	9	Ill-posed
5	Typical	11	Well-posed
6	Typical	12	Well-posed

6.2 Numerical Studies

6.2.1 Performance Metrics

Four performance metrics are devised to compare results based the suitable minimum criterion from Eq. (4.2). Suitable minima are identified on the condition that the backcalculated $|E^*|$ curves deviate no more than 10% from their corresponding truth curves within the EFR. More specifically, two $|E^*|$ curves are constructed per simulated backcalculation, and both must achieve the 10% difference criterion. The present study employs loads with different EFR's; consequently, one EFR is used for all suitable minimum calculations to provide a consistent basis for comparison across all results. The EFR is selected from the Typical pulse shape with $T = 40$ ms, which is visually inspected to span $16.67 \leq f \leq 100$ Hz. The interested reader is encouraged to replicate the signal using Eq. 6.1, noting that the choice of P is trivial for determining the EFR in the present case.

The performance metrics are devised to compare the differences in backcalculation accuracy due to different pulse shapes, widths, and magnitudes as well as the optimization posedness (via the number of sensors with respect to the number of updating variables). The metrics are called relative effectiveness, and one is defined for each quality: η_T corresponds to the relative performance associated with different pulse widths, η_P is for load magnitudes, η_S is for the load shapes, and η_N is for the number of sensors. The general calculation of the relative effectiveness metrics is

conducted as

$$\eta = \frac{n_{\text{sm}}}{n_{\text{sm,ref}}}, \tag{6.3}$$

where n_{sm} is the number of suitable minima obtained from all LHS samples for the particular configuration, and $n_{\text{sm,ref}}$ is the number of suitable minima corresponding to a reference configuration. In essence, $\eta < 1$ corresponds to worse performance than the reference configuration, and $\eta > 1$ represents superior performance compared to the reference. Different reference configurations are chosen for each model, and they are indicated by a value of $\eta = 1$ with respect to a given model. Furthermore, differences between metric values can be easily converted to percentage; for example, $\eta = 1.2$ denotes a 20% higher effectiveness relative to the reference configuration.

6.2.2 Results

The results for the width-based relative effectiveness, η_T, are given for the ill-posed Testing Groups in Table 6.4a and for the well-posed Testing Groups in Table 6.4b. The number of suitable minima used to calculate η_T reflects results across all combinations of load shape and magnitude for the given model, and the reference configuration reflects $T = 20$ ms. In general, backcalculations using the 20 ms pulse width converged to suitable minima more often than the broader widths for both ill- and well-posed configurations.

Interestingly, Model D served as an exception to the overall trend regarding pulse width, for which $T = 30$ ms resulted in slightly better performance than $T = 20$ ms and $T = 40$ ms in both ill- and well-posed backcalculation. The underlying root cause is likely related to the signal shapes in the frequency domain, such as the examples given for $P = 40$ kN, $T = 30$ ms in Fig. 6.1b. When the Typical shape is converted to the frequency domain, the signal exhibits one large peak at the low bound of the EFR of 16.67 Hz, a second smaller peak at 66.67 Hz, and a trough at 50 Hz. Each of the Typical loads exhibit these qualities in the frequency domain; however the locations of the trough and second peak vary depending on the pulse's time duration. Hence, $T = 30$ ms likely contains a greater force content than the other two pulse widths at a frequency that is significant to the dynamics of Model D. The same reasoning can also be applied to the discrepancy between the ill- and well-posed results for $T = 40$ ms with Model D. Specifically, the 40 ms pulse was marginally better than the 20 ms pulse by approximately 0.59% for ill-posed backcalculation; however, it was

Table 6.4. Average width-based relative effectiveness, η_T, calculated from the (a) ill-posed Testing Groups 1–4 and (b) well-posed Testing Groups 5–6. The reference configurations for each η_T correspond to the $T = 20$ ms results averaged across the corresponding model and Testing Groups.

Model	T	η_T
A	20 ms	1
	30 ms	0.9716
	40 ms	0.9698
B	20 ms	1
	30 ms	0.8900
	40 ms	0.8067
C	20 ms	1
	30 ms	0.7645
	40 ms	0.6710
D	20 ms	1
	30 ms	1.0243
	40 ms	1.0059

(a)

Model	T	η_T
A	20 ms	1
	30 ms	0.9649
	40 ms	0.9401
B	20 ms	1
	30 ms	0.9058
	40 ms	0.9261
C	20 ms	1
	30 ms	0.8762
	40 ms	0.9833
D	20 ms	1
	30 ms	1.0249
	40 ms	0.8502

(b)

significantly worse for well-posed backcalculation, being approximately 85% as effective as the 20 ms pulse for backcalculating suitable minima. There is likely a frequency that becomes significant when transitioning from ill-posed to well-posed backcalculation with Model D, which the 40 ms pulse does not sufficiently excite.

The relative effectiveness of the pulse shapes, η_S, is given in Table 6.5 for the ill-posed Testing Groups 1–4. Results from Testing Groups 5 and 6 are excluded because no Testing Groups were created which involve well-posed backcalculations with Simple shape loads. Both the Typical and Simple shape types produced similar performance in backcalculating suitable minima for Models A, B, and D, being within a 3% difference of each other overall. However, the Simple shape had slightly better performance in Models A and B, which was unexpected because the shape generally excites a smaller range of frequencies than comparable Typical shapes (see, *e.g.*, Fig. 6.1b), and may be due to a more effective distribution of force magnitude in the frequency domain.

There was a significant discrepancy in backcalculations with Model C, where the Simple shape only converged to 91.53% of the number of suitable minima found via the Typical shape. The reason is likely that the Typical shape has a "double-hit" signature, denoted by two peaks in the

Table 6.5. Average width-based relative effectiveness, η_S, calculated from Testing Groups 1–4. The reference configuration for each η_S correspond to the Typical shape results averaged across Testing Groups 1 and 3 for each model.

Model	Shape	η_S
A	Typical	1
	Simple	1.0272
B	Typical	1
	Simple	1.0276
C	Typical	1
	Simple	0.9153
D	Typical	1
	Simple	0.9834

time domain as in Fig. 6.1a. In the frequency domain, this manifests as the second, smaller peak, such as the one at 66.67 Hz in Fig. 6.1b. Consequently, the dynamics of Model C relevant in backcalculation may be sensitive to a particular frequency that is not adequately excited by the Simple shape. This is supported by the results for η_T in Table 6.4a, where the largest overall difference between $T = 20$ ms (wider range of excited frequencies) and $T = 40$ ms (narrower range of excited frequencies) loads was observed in the ill-posed backcalculations with model C.

The magnitude-based relative effectiveness, η_P, is presented for the results from Testing Groups 1–6 in Fig. 6.3. Curves are plotted for each pulse width individually to provide insight on the relationship between pulse width and magnitude, and the average is plotted to compare overall performance. The reference configuration for each model is selected as $P = 40$ kN (9 kips), which is the standard magnitude used for FWD testing by many state agencies such as GDOT. Backcalculation with Models A and B were fairly insensitive to magnitude for each pulse width, whereby none of the magnitudes promoted suitable minimum convergence significantly more than the others. However, very slight upward trends can be seen in the average curves, indicating that higher magnitudes provided slightly better backcalculation performance. Curiously, the most notable variation between pulse widths for these two models can be seen with $P = 26.7$ kN for Model A and $P = 66.7$ kN for Model B. Investigation into the individual results reveals this trend occurs within each Testing Group, meaning the root cause is not due to optimization posedness or pulse shape. Thus, these variations are likely a result of some subtle computational phenomenon.

For example, these configurations may be more prone to rounding errors that reduce the optimizer's ability to converge to suitable minima.

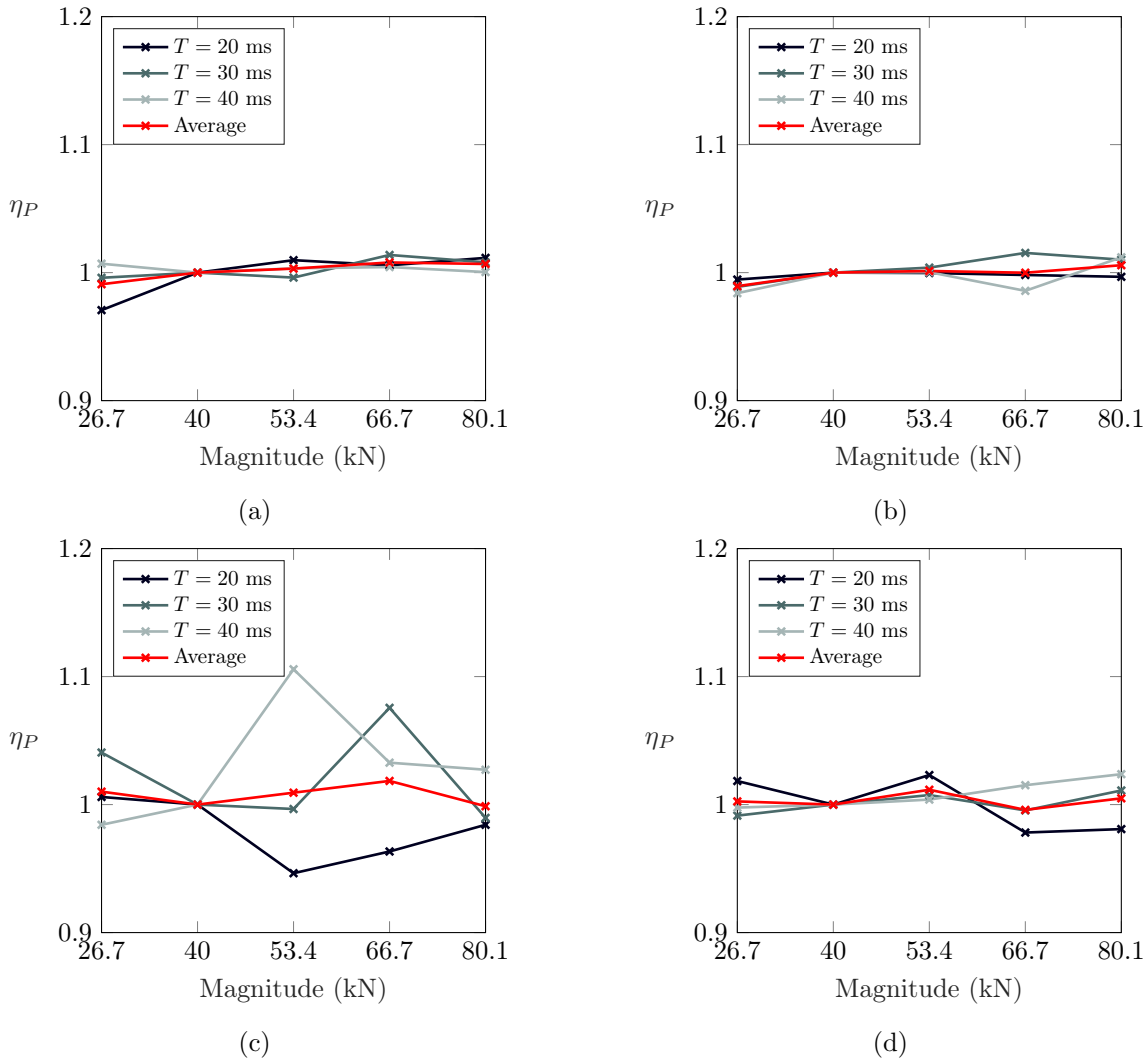

Figure 6.3. Magnitude-based relative effectiveness, η_P, calculated from Testing Groups 1–6 for each pulse width for Models (a) A, (b) B, (c) C, and (d) D. Red lines denote the average η_P with respect to pulse width. The reference configurations used for each η_P correspond to $P = 40$ kN.

The η_P results for Models C and D exhibit more variation among the different pulse widths. Examining Table 6.1, two general quality differences can be identified between the material properties of Models C and D and that of Models A and B; specifically, they have foundation layers with significantly stiffer elastic moduli (E_3, E_4), and they have less overall viscous damping (ζ). Investigation into the individual results reveals these variations among pulse widths are present for all Testing Groups with Models C and D, and are therefore not likely a result of differences in

the optimization structure or pulse shape. Rather, they likely stem from differences in pavement dynamics due to stiffer foundation layers and/or lower damping, thereby causing the backcalculations to be more sensitive to changes in pulse width. However, the average η_P trend exhibits low sensitivity to pulse magnitude for Models C and D, similar as with Models A and B. Consequently, the most plausible root cause for the variations observed among η_P is likely a result of the subtle changes to the EFR resulting from interplay between magnitude and pulse width, as opposed to arising from the value of the pulse magnitude itself.

Results for the relative effectiveness with respect to the number of sensors, η_N, are given in Fig. 6.4. Individual and average results are plotted with respect to pulse width, which has the most significant effect on the EFR. Additionally, only results for Testing Groups 1, 3, 5, and 6 are considered because they use the Typical load shape. The reference configuration for each figure is chosen from the results corresponding to $n_s = 7$ sensors, which is a common number of sensors used for FWD testing. Based on the average trends, the well-posed optimization structures ($n_s = 11,\ 12$) always resulted in better backcalculation performance than the ill-posed cases ($n_s = 7,\ 9$) for all models. Increasing the number of sensors from seven to eleven improved the average η_N of Models A and D by 13.3% and 15.8%, respectively; however, a negligible change in relative effectiveness was observed with Model B. Most notably, the same change dramatically improved backcalculation with Model C, increasing the number of suitable minima found by 58.4%. Increasing the number of sensors to from eleven to twelve further improved backcalculation performance among all models, with the exception of Model D wherefore η_N slightly decreased from 1.158 to 1.150.

Among the ill-posed configurations, it can be seen that backcalculation performance generally improves from $n_s = 7$ to $n_s = 9$. However, the results for Model B are an exception, where the average η_N decreased from when transitioning from seven to nine sensors. Examining the individual results among pulse widths, it can be seen the relative effectiveness for $T = 20$ ms was nearly identical for these two sensor quantities, but η_N exhibited notable decreases for both $T = 30$ ms and $T = 40$ ms. This means the addition of two sensors while remaining ill-posed resulted in a more arduous optimization space for Model B despite having more observations available. Considering this was only significant with the broader pulse widths, it is possible the deflection of Model B at the two additional locations is sensitive to frequencies near the upper bound of the EFR, thereby increasing the difficulty of identifying a suitable minimum. Nonetheless, all other pulse width and

pavement model configurations demonstrated improved ill-posed backcalculation performance with additional sensors.

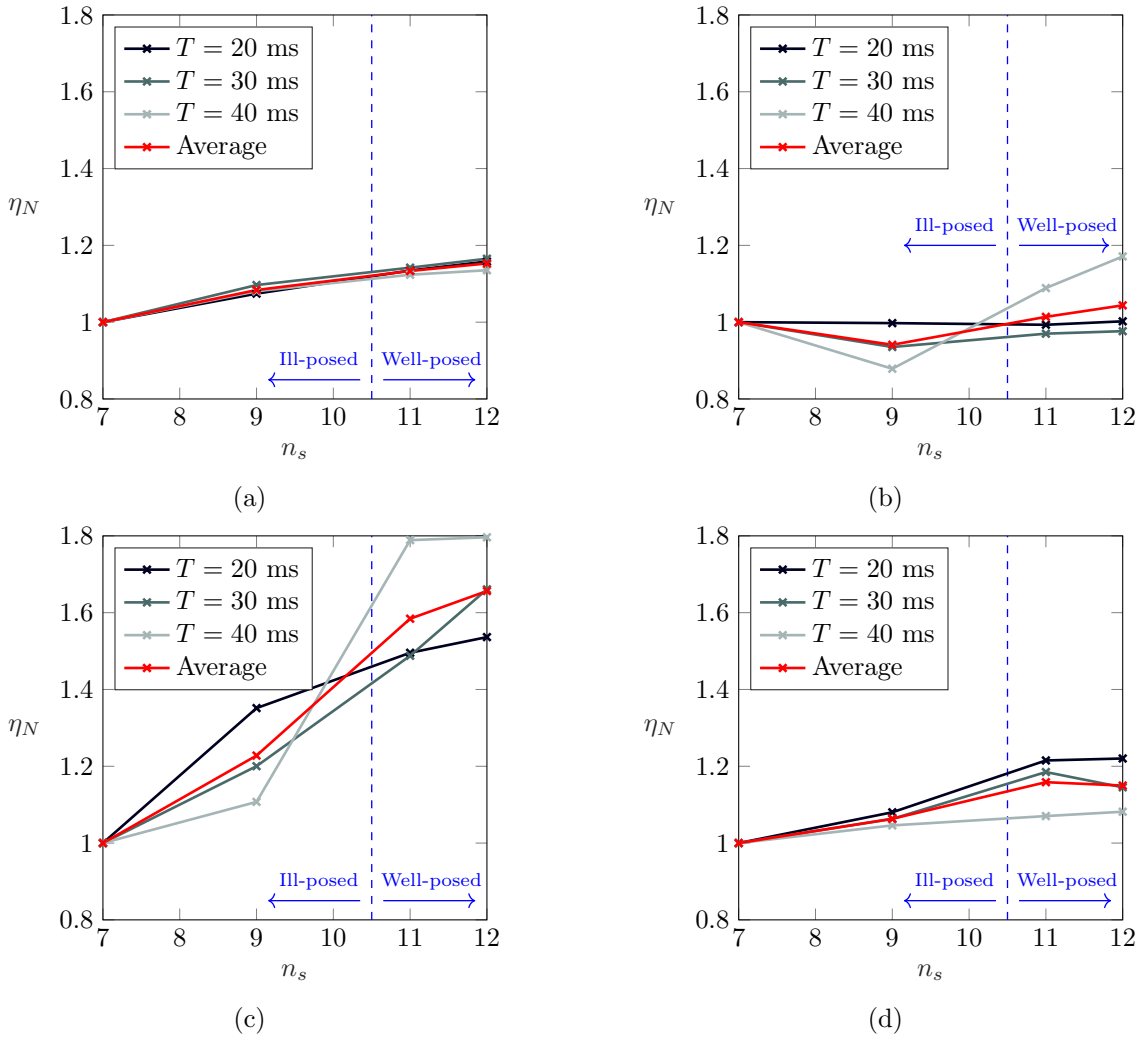

Figure 6.4. Relative effectiveness based on number of sensors, η_N, calculated from Testing Groups 1, 3, 5, and 6 for each pulse width for Models (a) A, (b), B, (c) C, and (d) D. Red lines denote the average η_N with respect to pulse width. The reference configurations used for each η_N correspond to $n_s = 7$ sensors.

6.3 Conclusions

6.3.1 Summary

The study conducted here examines the structure of current FWD testing methodology from a backcalculation analyst's perspective, and they are motivated by two key ideas. The first includes

altering characteristics (magnitude, duration, and shape) of the FWD load pulse to expand the effective frequency range associated with FWD testing, and the second involves increasing the number of deflection sensors to achieve a well-posed optimization structure in the backcalculation. Results are analyzed from 720,000 unique simulated backcalculations spanning four pavement models, five pulse magnitudes, three pulse durations, two pulse shapes, four sensor quantities, and 2,000 sets of seed moduli.

Based on the results, narrow load pulses (*i.e.*, short impact durations) are more conducive to backcalculating suitable minima than broad pulses, because the former excites a wider range of frequencies in the pavement response. In general, the particular shape of the force signal appears to have little effect on overall backcalculation performance; however, pulse shape affects the distribution of force in the frequency domain, which was relevant in some backcalculation configurations. Therefore, it is important to verify that the FWD load does not preclude excitation of frequencies relevant in the pavement's dynamic response.

Backcalculation performance was observed to be relatively insensitive to variation in load magnitude, although higher magnitudes performed marginally better overall. Thus, it may be ideal to conduct FWD testing with the highest possible magnitudes in practice, which also helps reduce the influence of measurement noise. Additionally, the number of suitable minima backcalculated for well-posed optimization structures was higher than ill-posed cases across all models, it is therefore recommended to perform FWD testing with as many displacement sensors as possible. The availability of more displacement measurements allows for the inclusion of more variables in the optimization without suffering penalties to suitable minimum backcalculation.

6.3.2 Limitations

The conclusions presented here are aimed toward modifying the design of FWD equipment to improve backcalculation performance. However, the modern development and fabrication of FWD equipment is entirely handled by for-profit businesses, which must maintain a certain degree of privacy for their intellectual property. As a result, it is difficult to ascertain the feasibility of this research study due to the lack of information publicly available.

Furthermore, the EFR can be expanded through two means, and only one of them is explored here. The present study only consider shifting the upper bound of the EFR via changing the pulse

width. It would be insightful to also examine the effects of shifting the lower bound, which is affected by changing the length of time that measurements are recorded. In the present study, all forces and deflections were simulated in a 60 ms time window. It would be beneficial to perform similar tests with different measurement time windows, which can decrease the lower bound of the EFR and improve frequency resolution.

Chapter 7

Approximate Interconversion Between Dynamic and Relaxation Moduli

Asphalt concrete is well known to be viscoelastic, meaning its stiffness changes depending on the material's temperature as well as the rate at which it is loaded. Here, two of the most common approaches used to represent the viscoelastic stiffness of asphalt are examined. The first is dynamic modulus, $|E^*|$, which is a function of loading frequency, f, and the second is relaxation modulus, $E(t)$, which is a function of loading time, t. Because these material response functions represent the modulus in different domains (*i.e.*, either time or frequency), choosing between them typically depends on the usage scenario. For example, dynamic modulus is favorable for describing viscoelastic materials under periodic excitation, whereas relaxation modulus is more suitable for static load cases. In practice, it is common for pavement engineers to have asphalt stiffness represented by one function but not the other. Then, when a situation arises in which it is more favorable to use the other stiffness function, they require some way to convert between them. This general concept is referred to as interconversion, and it is useful in the context of FWD backcalculation because the developed methods typically output either $|E^*|$ or $E(t)$, but not both.

In this chapter, interconversion between $|E^*|$ and $E(t)$ is studied to improve the accuracy of a widely used approach to approximate interconversion. The technique essentially involves using a single parameter, β, to interrelate the stiffness moduli. First, formulations of the viscoelastic stiffness function models and their interrelationships are presented in Section 7.1. Then, a novel

numerical approach for determining the optimal β value for approximate $|E^*| \leftrightarrow E(t)$ interconversion is detailed in Section 7.2. Finally, the novel approach is compared to existing methods across 30 samples of hot mix asphalt in Section 7.3, and concluding remarks are given in Section 7.4.

7.1 Viscoelastic Stiffness Models

Relaxation modulus is defined as a viscoelastic material's stress response, $\sigma(t)$, normalized by a constant strain loading, ϵ_0, given by

$$E(t) = \frac{\sigma(t)}{\epsilon_0}. \tag{7.1}$$

A viscoelastic material's response to a harmonic load can be determined by taking the Carson transform (*i.e.*, the s-multiplied Laplace transform) of the relaxation modulus and substituting $s \rightarrow i\omega$, yielding

$$E^*(\omega) = i\omega\hat{E}(s)|_{s \rightarrow i\omega}, \tag{7.2}$$

where $i = \sqrt{-1}$ is the imaginary constant, ω is angular loading frequency in units of radians per second, E^* is the complex modulus, and $\hat{\circ}$ denotes a Laplace transformed entity, given by $\hat{f}(s) = \mathcal{L}\{f(t)\} = \int_0^\infty f(t)e^{-st}\,dt$. The complex modulus can be decomposed into a real part of $E^{'}$ and an imaginary part of $E^{''}$, which are known as the storage and loss moduli, respectively. The storage modulus represents the amount of elastic energy in the material, whereas the loss modulus corresponds to the amount of energy viscously dissipated from the material. Finally, the dynamic modulus is defined as the magnitude of complex modulus, given by

$$|E^*(\omega)| = \sqrt{E^{'}(\omega)^2 + E^{''}(\omega)^2}. \tag{7.3}$$

Note the domain of $|E^*|$ is often converted in practice from circular frequency (units of radians per second) to cyclic frequency (units of Hz) via $\omega = 2\pi f$.

The material response functions are typically determined from experimental testing and subsequently applying a curve fit to the measured data. The two most commonly used curve fitting techniques in pavement engineering are the Prony series and sigmoidal function approximations. The Prony series is capable of more accurate matching; however, it often requires a significantly

greater number of terms than a comparable sigmoidal fit. Both manners of approximation are detailed for $E(t)$ and $|E^*|$ in the following subsections.

7.1.1 Prony Series

The relaxation response of a viscoelastic material is commonly described using the generalized Maxwell model, which is comprised of one linearly elastic spring in parallel with M viscoelastic Maxwell elements, which are each composed of a spring and dashpot in series. The aggregate stiffness of the generalized Maxwell model is relaxation modulus, and it can be expressed via Prony series as

$$E(t) = E_0 + \sum_{j=1}^{M} E_j e^{-t/\rho_j}, \tag{7.4}$$

where E_0 is the stiffness of the linearly elastic spring, and E_j and ρ_j are the stiffness and relaxation time of the j^{th} viscoelastic Maxwell element. Prony series expressions for the storage and loss moduli are obtained by combining Eqs. (7.2) and (7.4) and isolating the real and imaginary parts of E^*, yielding

$$E^{'}(\omega) = E_0 + \sum_{j=1}^{M} \frac{\omega^2 \rho_j^2 E_j}{1 + \omega^2 \rho_j^2}, \tag{7.5}$$

$$E^{''}(\omega) = \sum_{j=1}^{M} \frac{\omega \rho_j E_j}{1 + \omega^2 \rho_j^2}. \tag{7.6}$$

Finally, the Prony series for dynamic modulus is determined by substituting Eqs. (7.5) and (7.6) into (7.3), which gives

$$|E^*(\omega)| = \sqrt{\left(E_0 + \sum_{j=1}^{M} \frac{\omega^2 \rho_j^2 E_j}{1 + \omega^2 \rho_j^2}\right)^2 + \left(\sum_{j=1}^{M} \frac{\omega \rho_j E_j}{1 + \omega^2 \rho_j^2}\right)^2}. \tag{7.7}$$

7.1.2 Sigmoidal Functions

The sigmoidal curve fit is derived from the observation that the general forms of $E(t)$ and $|E^*|$ vary monotonically and are bounded by two horizontal asymptotes. When plotted on logarithmic scale, they appear as smoothly varying S-shaped functions. Functions with such characteristics are

referred to as sigmoids, and there exists a variety of different forms of sigmoidal fitting functions. Curve fits applied to $E(t)$ and $|E^*|$ commonly have the forms

$$\log\big(E(t)\big) = c_1 + \frac{c_2}{1 + e^{c_3 + c_4 \log(t)}}, \tag{7.8}$$

$$\log\big(|E^*|\big) = d_1 + \frac{d_2}{1 + e^{d_3 + d_4 \log(f)}}, \tag{7.9}$$

where c_i and d_i are the sigmoidal coefficients used to define the shapes of the sigmoid fits for their respective stiffness moduli. An example plot of dynamic modulus with annotations to visualize its sigmoidal coefficients is given in Fig. 4.1. In words, d_1 is the minimum modulus value in logarithmic scale, d_2 is the range of modulus values, and d_3 and d_4 are shape parameters relating to the midpoint position and slope of the sigmoid. The corresponding coefficients for a relaxation modulus sigmoid, c_1–c_4, control the same aspects.

7.1.3 Interrelationships

Now that mathematical expressions are defined for the material response functions, interrelationships can be determined between them. First, consider conversion between the Prony series for $E(t)$ and $|E^*|$ given in Eqs. (7.4) and (7.7). With the exception of the different domain parameters of t and ω, the same terms (E_0, E_j, and ρ_j) are used to construct both Prony series expressions. This is possible because the Laplace transforms of Eqs. (7.4) and (7.7) exist in closed form. Thus, exact interconversion is feasible between $E(t)$ and $|E^*|$ if a Prony series is known for either quantity [79].

Next, consider converting between the sigmoidal expressions for $E(t)$ and $|E^*|$ in Eqs. (7.8) and (7.9). Despite having high similarity, an exact analytical interrelationship cannot be determined between them because Laplace transforms of the equations do not exist in closed form. Consequently, approximate interrelationships must be used when working with sigmoidal functions of the moduli. This is commonly handled by directly relating the time and frequency domains by

$$f \approx \frac{\beta}{t}, \tag{7.10}$$

where β is the time-frequency equivalency factor. A commonly used value for the conversion factor originates from an approximate relationship derived by Christensen [77]. Using an exact

relationship between $E(t)$ and $E^{'}$, the factor was determined to be $\beta = 1/\pi^2 \approx 0.1$. However, because it was derived without consideration for $E^{''}$, this value is prone to erroneous approximation when converting between $E(t)$ and $|E^*|$. This was noted by Daniel and Kim [86], who determined that $\beta = 1/4\pi \approx 0.08$ offers better conversion accuracy when both the real and imaginary parts of complex modulus are of interest. However, the details of their approach for determining this value are sparse.

An analytical expression for β can be derived for conversion between the two sigmoidal functions. First, it is assumed that $c_1 = d_1$ and $c_2 = d_2$; in words, this means the minimum and maximum modulus values are equivalent in the time and frequency domains. Afterward, by inserting Eqs. (7.8) and (7.9) into the interrelationship $E(t) = |E^*(\beta/t)|$, the formula for the time-frequency equivalency factor is obtained as

$$\beta = 10^{(\frac{c_3 - d_3}{d4})} t^{(1+\frac{c_4}{d_4})}. \tag{7.11}$$

Alternatively, inserting the sigmoidal functions into the interrelationship $E(\beta/f) = |E^*(f)|$ yields

$$\beta = 10^{(\frac{d_3 - c_3}{c_4})} f^{(1+\frac{d_4}{c_4})}. \tag{7.12}$$

Inspection of Eqs. (7.11) and (7.12) reveals the value of β changes with respect to time or frequency depending on which sigmoid is being treated as the basis function in the interrelationship. It is also apparent that β depends on the sigmoidal shape parameters from both moduli c_3, c_4, d_3, and d_4. Consequently, Eqs. (7.11) and (7.12) can generally not be used to determine β because only the sigmoidal coefficients for either $E(t)$ or $|E^*|$ are typically known.

7.2 Method for Determining Time-Frequency Equivalency Factor

Previous recommendations for β values have involved factors of π [77, 86–88], presumably because of the relationship between time and ordinary frequency, *i.e.*, $t = 1/2\pi f$. However, Eqs. (7.11) and (7.12) indicate that β does not explicitly involve π, and is instead a function of the sigmoidal coefficients of a given pavement. Here, a novel procedure is presented for determining a generally appropriate β for approximate $|E^*| \leftrightarrow E(t)$ interconversion. First, descriptions of the experimental data sets used for the study are given. Afterward, a robust numerical method for determining β

from the experimental data is detailed. The method is designed to identify a value of β that is consistent with typical values of the shape parameters for hot mix asphalt, and is thereby generally applicable across different pavement configurations.

Some steps of the method involve nonlinear least-squares minimization; in each case, the optimization is conducted with the tandem trust-region (TTR) algorithm developed in Chapter 3. The scope of the method is focused on converting between the sigmoidal functions in Eqs. (7.8) and (7.9), because the alternative mathematical model for viscoelastic modulus, the Prony series, is capable of exact interconversion between $E(t)$ and $|E^*|$. However, it can be reasoned that the results of this approach are generally applicable to any model for the moduli due to the similarity of their shapes.

7.2.1 Description of Test Data

Two distinct sets of hot mix asphalt $|E^*|$ data measured by an Asphalt Mixture Performance Tester (AMPT) are used to determine the optimal value of β. Each data entry corresponds to the dynamic modulus master curve at a reference temperature of 21.1°C. The first data set is taken from a study by Kim *et al.* [5] wherein samples of asphalt were prepared in a lab setting specifically for AMPT testing. Details of each asphalt mixture in the lab data set are given in Table 7.1, including their performance grades (PG) and nominal maximum aggregate sizes (NMAS). Note the data set is primarily comprised of surface mixes, or those used for the uppermost lift of the asphalt layer, which are indicated by NMAS of 9.5 and 12.5 mm.

Table 7.1. List of hot mix asphalt samples in the lab data set from Kim *et al.* [5].

Identifier	Mix Grade	NMAS
PG-64A	PG64	9.5 mm
PG-64B		12.5 mm
PG-64C		12.5 mm
PG-64D		19 mm
PG-64E		25 mm
PG-67A	PG67	9.5 mm
PG-67B		9.5 mm
PG-67C		12.5 mm
PG-67D		12.5 mm
PG-76A	PG76	12.5 mm
PG-76B		12.5 mm

The second set is constituted by pavement data used in Chapter 5. In contrast to the first data set, these samples were extracted from *in situ* pavements across Georgia, USA and have unknown ages and distresses. Furthermore, the *in situ* set contains a larger variety of intermediate and base mixes (*i.e.*, additional layers of asphalt below the surface layer), and the specific performance grades of each sample are unknown. It comprises the following entries: three lifts from sample GA-10A, three lifts from sample GA-10B, two lifts from sample GA-11, five lifts from sample GA-22, one lift from sample GA-26, two lifts from sample GA-57, one lift from GA-82A, one lift from GA-82B, and one lift from GA-129.

The two data sets used herein differ in that one reflects pavements manufactured in a lab setting whereas the other represents pavements constructed and partially deteriorated in the field. Additionally, one primarily comprises surface mixes while the other contains a higher portion of samples from intermediate and base mixes. These distinctions between the lab and *in situ* sets are intended to support the applicability of results from the following study to determine β.

7.2.2 Outline of Numerical Method

For its input, the method takes an $|E^*|$ sigmoid derived from AMPT test data in the same form as Eq. (7.9). The first step is to determine an equivalent Prony series formulation for $|E^*|$ using the input dynamic modulus sigmoid. This is accomplished here via constrained nonlinear least-squares minimization of the form

$$\begin{aligned} \min_{\boldsymbol{E}} g(\boldsymbol{E}) &= \left\| 1 - \frac{|\boldsymbol{E}^*_{\mathbf{P}}(\boldsymbol{E}, \boldsymbol{f})|}{|\boldsymbol{E}^*_{\mathbf{S}}(\boldsymbol{f})|} \right\|_2^2, \\ &\text{s.t. } \boldsymbol{E} > \mathbf{0}, \end{aligned} \tag{7.13}$$

where $|\boldsymbol{E}^*_{\mathbf{S}}|$ is the dynamic modulus sigmoidal function discretized by a vector of frequency points $\boldsymbol{f}$, $||\circ||_2$ denotes the L2 norm operation, and

$$|\boldsymbol{E}^*_{\mathbf{P}}(\boldsymbol{E}, \boldsymbol{f})| = \left[\left(E_0 + \sum_{j=1}^{M} \frac{4\pi^2 \boldsymbol{f}^2 \rho_j^2 E_j}{1 + 4\pi^2 \boldsymbol{f}^2 \rho_j^2} \right)^2 + \left(\sum_{j=1}^{M} \frac{2\pi \boldsymbol{f} \rho_j E_j}{1 + 4\pi^2 \boldsymbol{f}^2 \rho_j^2} \right)^2 \right]^{\frac{1}{2}}, \tag{7.14}$$

$$\boldsymbol{E} = \{E_0, E_1,\ E_2,\ ...,\ E_M\}. \tag{7.15}$$

The objective function in Eq. (7.13) is normalized by $|\boldsymbol{E}^*_{\mathbf{S}}|$ (as opposed to taking the difference between $|\boldsymbol{E}^*_{\mathbf{S}}|$ and $|\boldsymbol{E}^*_{\mathbf{P}}|$) to promote consistent error magnitudes across the entire domain. Additionally, the dynamic modulus Prony series, $|\boldsymbol{E}^*_{\mathbf{P}}|$, is modified from Eq. (7.7) to be in terms of cyclic frequency using the relationship $\omega = 2\pi f$. The set of relaxation times, $\boldsymbol{\rho}$, is defined using bilogarithmically spaced time points as $\rho_1 = 10^{-10}$ s, $\rho_2 = 10^{-9.5}$ s, $\rho_3 = 10^{-9}$ s, ... , $\rho_{41} = 10^{10}$ s. The corresponding Prony series order is $M = 41$, which produces a near-exact fit to the sigmoidal function.

Once the elastic coefficients, $\boldsymbol{E}$, are computed from the $|E^*|$ optimization, an $E(t)$ Prony series expression can be constructed using Eq. (7.4). After which, the optimal value of β is determined between the input $|E^*|$ sigmoid and the near-exactly converted $E(t)$ Prony series via nonlinear least-squares optimization as

$$\min_{\beta} h(\beta) = \left\| 1 - \frac{|\boldsymbol{E}^*_{\mathbf{S}}(\beta/\boldsymbol{t})|}{\boldsymbol{E}_{\mathbf{P}}(\boldsymbol{t})} \right\|_2^2, \tag{7.16}$$

where $\boldsymbol{E}_{\mathbf{P}}(\boldsymbol{t})$ is the relaxation modulus Prony series function discretized by a vector of time points $\boldsymbol{t}$. An outline of the numerical procedure for determining β for a given asphalt sample is given in Fig. 7.1.

The discrete domains used in the optimizations from Eqs. (7.13) and (7.16) span different orders of magnitude. The first optimization involves a Prony series fit across the frequency domain defined by $\boldsymbol{f}$. The optimization is conducted using 1,000 logarithmically spaced points spanning $10^{-10} \leq f \leq 10^{10}$ Hz, which are chosen such that the asymptotes of the functions are sufficiently considered while computing the Prony series fit, thereby facilitating a near-exact conversion. However, the time-frequency equivalency factor is intended for approximate interconversion in practical applications. Consequently, the time domain used for β optimization, $\boldsymbol{t}$, is defined by a narrower domain of 1,000 logarithmically spaced points across $10^{-4} \leq t \leq 10^4$ s, which reflects the range of times typically used to plot pavement moduli in practice.

Procedure for Determining $\boldsymbol{\beta}$
Given d_1, d_2, d_3, d_4;
$\boldsymbol{\rho} = 10^{-10},\ 10^{-9.5},\ 10^{-9},\ \ldots,\ 10^{10}$ s;
$\boldsymbol{f}$ = 1,000 logarithmically spaced points on $[10^{-10},\ 10^{10}]$ Hz; and
$\boldsymbol{t}$ = 1,000 logarithmically spaced points on $[10^{-4},\ 10^{4}]$ s.

1. Obtain $|\boldsymbol{E}^*_{\mathbf{S}}|$ using Eq. (7.9) discretized by $\boldsymbol{f}$.
2. Determine Prony coefficients $(E_0,\ E_1,\ \ldots,\ E_{41})$ using Eq. (7.13) discretized by $\boldsymbol{f}$.
3. Compute β using Eq. (7.16) discretized by $\boldsymbol{t}$.

Figure 7.1. Outline of numerical procedure for determining time-frequency equivalency factor, β.

7.3 Results

Approximate $|E^*| \rightarrow E(t)$ conversions are conducted in the following studies. First, optimal β values are individually calculated for the lab and *in situ* data sets described using the numerical procedure from Fig. 7.1. Afterward, conversions using the average optimal β are compared to three alternative approximate techniques: the Daniel-Kim (DK) [86], Park-Schapery (PS) [82], and Ninomiya-Ferry (NF) methods [80]. The DK method employs the time-frequency equivalency approach in Eq. (7.10) with $\beta = 0.08$, whereas the PS and NF methods involve more sophisticated conversion procedures. Although other methods involving β conversion have been proposed in the literature, the DK method was determined by the authors to have the best accuracy among them. In the following studies, the error of each approximate conversion is quantified by their similarity to the near-exactly converted relaxation modulus, $\boldsymbol{E}_{\mathbf{P}}(\boldsymbol{t})$, via

$$\zeta = \frac{100\%}{N} \sum_{k=1}^{N} \left| 1 - \frac{\tilde{E}(t_k)}{E_{\mathrm{P}}(t_k)} \right|, \tag{7.17}$$

where ζ is the percent error, t_k is the k^{th} point in $\boldsymbol{t}$, and N=1,000 is the total number of points. The approximated relaxation modulus, $\tilde{\boldsymbol{E}}(\boldsymbol{t})$, changes depending on which method is used for conversion.

7.3.1 Optimal Value of β

The optimal time-frequency equivalency factors, β_{opt}, and corresponding conversion errors, ζ, computed for the asphalt samples from the lab data set are given in Table 7.2. The average β_{opt} value

calculated among the samples is 0.0662 with a standard deviation of $2.8{\cdot}10^{-3}$ and an average conversion error of 1.39%. The set of five PG-64 mixtures and set of four PG-67 mixtures comprise errors ranging from approximately 1% to 3% while both PG-76 mixtures are near 1%. No apparent trends were identified with respect to NMAS or performance grades 64 and 67; however, the two samples of PG-76 produced nearly identical β_{opt} and similar conversion errors. The worst conversion occurred with PG-64B, having a relative average error of 2.91% between $|\boldsymbol{E}^*_{\mathbf{S}}(\beta/\boldsymbol{t})|$ and $\boldsymbol{E}_{\mathbf{P}}(\boldsymbol{t})$, whereas the best conversion was observed from PG-67B with $\zeta = 0.96\%$.

Table 7.2. Optimal values of the time-frequency equivalency factor, β_{opt}, and conversion errors, ζ, determined for the lab pavement data set from from Kim *et al.* [5].

Mixture	β_{opt}	ζ
PG-64A	0.0665	1.32%
PG-64B	0.0598	2.91%
PG-64C	0.0642	1.65%
PG-64D	0.0678	1.04%
PG-64E	0.0689	0.97%
PG-67A	0.0631	1.90%
PG-67B	0.0685	0.96%
PG-67C	0.0677	1.05%
PG-67D	0.0657	1.37%
PG-76A	0.0680	1.03%
PG-76B	0.0681	1.07%
Mean:	0.0662	1.39%
Std. Dev.:	0.0028	0.59%

The β_{opt} values and conversion errors calculated for the *in situ* data set are given in Table 7.3. The average optimal β is 0.0679 with a standard deviation of $2.2{\cdot}10^{-3}$ and a mean error of 1.12%. No trends with respect to the lift number (analogous to NMAS) are apparent among the samples. The best conversion was observed from the sample corresponding to the fourth lift of GA-22, which had an error of 0.65% between $|\boldsymbol{E}^*_{\mathbf{S}}(\beta/\boldsymbol{t})|$ and $\boldsymbol{E}_{\mathbf{P}}(\boldsymbol{t})$, and the worst conversion occurred for the sample from GA-129 with an error of 1.73%. The best and worst β-converted moduli of the *in situ* set are plotted alongside their near-exactly converted counterparts in Fig. 7.4.

There is close agreement in the average optimal β values calculated among the two data sets, which have a relative difference of 2.54%. To determine the generally appropriate value of β, the lab and *in situ* data sets are combined, and a normal distribution is fit to the merged set using the `fitdist` function from MATLAB [128]. The mean β_{opt} of the combined set is 0.0673 with a

Table 7.3. Optimal values of the time-frequency equivalency factor, β_{opt}, and conversion errors, ζ, determined for the *in situ* pavement data set from Kim *et al.* [6].

Core	Lift	β_{opt}	ζ
GA-10A	1	0.0667	1.23%
	2	0.0665	1.38%
	3	0.0685	1.16%
GA-10B	1	0.0668	1.27%
	2	0.0678	1.16%
	3	0.0668	1.20%
GA-11	1	0.0670	1.15%
	2	0.0665	1.15%
GA-22	1	0.0701	0.87%
	2	0.0646	1.56%
	3	0.0674	1.07%
	4	0.0714	0.65%
	5	0.0692	1.02%
GA-26	1	0.0709	0.75%
GA-57	1	0.0681	1.08%
	2	0.0668	1.27%
GA-82A	1	0.0723	0.67%
GA-82B	1	0.0691	0.97%
GA-129	1	0.0641	1.73%
	Mean:	0.0679	1.12%
	Std. Dev.:	0.0022	0.27%

standard deviation of $2.5{\cdot}10^{-3}$ and an average error of $\zeta = 1.22\%$. From the distribution fit, the 95% confidence interval of the time-frequency equivalency factor is obtained as $\beta_{\text{opt}} = 0.0673 \pm 0.0009$.

Mean conversion error is plotted against β in Fig. 7.2 for the combined data set. Plots of mean ζ versus β for the lab and *in situ* sets are also included for comparison. The mean conversion errors correspond to the average of the ζ values calculated for each entry in the data set using the given β. Annotations of the statistically calculated results are included in Fig. 7.2 for visual comparison with the mean ζ analysis. The lowest average ζ is observed when $\beta = 0.0674$ for the combined set, which is very close to the average β_{opt} determined from normal distribution fit. Therefore, results from the mean ζ analysis further supports that $\beta_{\text{opt}} = 0.0673 \pm 0.0009$ is a generally appropriate range of values for the equivalency factor.

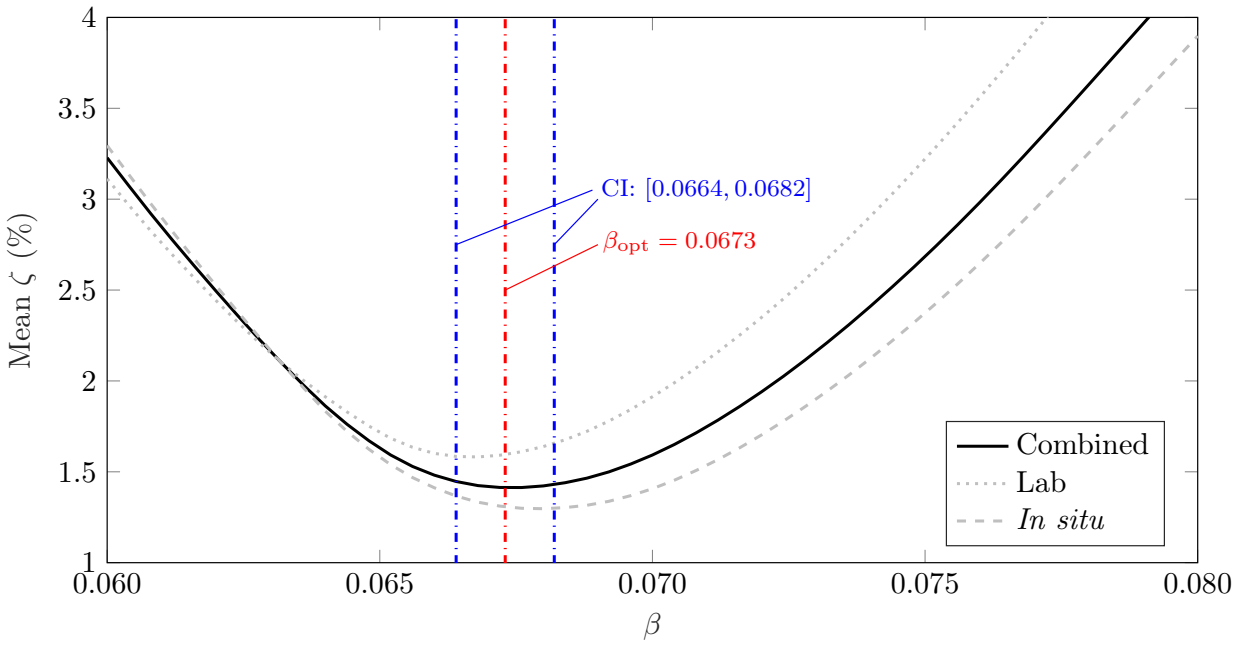

Figure 7.2. Mean conversion error, ζ, versus time-frequency equivalency factor, β, for the combined (solid black), lab (dotted gray), and *in situ* (dashed gray) data sets. The average optimal factor (β_{opt}) and 95% confidence interval (CI) bounds are annotated for the combined data set.

7.3.2 Comparison with Other Interconversion Methods

Here, the conversion accuracy of using the average β_{opt} determined in Section 7.3.1 is compared against the DK, PS, and NF methods. For convenience, the proposed approach involving the average optimal factor, $\beta_{\text{opt}} = 0.0673$, is referred to as the optimal β (OB) method. The $|E^*|$ sigmoids from each pavement sample are approximately converted to $E(t)$ using each method, and the conversion errors, ζ, are determined relative to the near-exactly converted relaxation modulus, $\boldsymbol{E_P(t)}$. The errors calculated for the lab data set are given in Table 7.4, and those for the *in situ* set are contained in Table 7.5. Errors corresponding to the average optimal factor, $\beta = 0.0673$, are denoted by ζ_{OB}. Conversion errors calculated from the three alternative methods are denoted using DK, PS, and NF subscripts. Note ζ_{OB} and ζ_{DK} correspond the time-frequency equivalency approach but with different values for β, whereas the PS and NF methods employ more sophisticated conversion approaches.

Combining both the lab and *in situ* data sets from Tables 7.4 and 7.5 together, the average conversion errors from each method are $\zeta_{\text{OB}} = 1.41\%$, $\zeta_{\text{DK}} = 4.3\%$, $\zeta_{\text{PS}} = 0.51\%$, and $\zeta_{\text{NF}} = 0.55\%$. These results indicate using $\beta = 0.0673$, as proposed in this chapter, leads to more accurate

Table 7.4. $|E^*| \rightarrow E(t)$ conversion errors, ζ_{OB}, calculated for the lab pavement data set with $\beta = 0.0673$. Conversion errors are also given for the Daniel-Kim (ζ_{DK}), Park-Schapery (ζ_{PS}), and Ninomiya-Ferry (ζ_{NF}) methods.

Identifier	ζ_{OB}	ζ_{DK}	ζ_{PS}	ζ_{NF}
PG-64A	1.34%	4.89%	0.60%	0.57%
PG-64B	4.00%	8.76%	0.54%	0.63%
PG-64C	1.95%	6.28%	0.62%	0.60%
PG-64D	1.07%	3.66%	0.64%	0.52%
PG-64E	1.03%	3.24%	0.68%	0.51%
PG-67A	2.53%	6.94%	0.50%	0.61%
PG-67B	0.99%	3.67%	0.52%	0.54%
PG-67C	1.05%	4.18%	0.50%	0.56%
PG-67D	1.47%	5.24%	0.56%	0.58%
PG-76A	1.04%	4.05%	0.52%	0.55%
PG-76B	1.08%	4.08%	0.53%	0.55%
Mean:	1.60%	5.00%	0.56%	0.56%

Table 7.5. $|E^*| \rightarrow E(t)$ conversion errors, ζ_{OB}, calculated for the *in situ* pavement data set with $\beta = 0.0673$. Conversion errors are also given for the Daniel-Kim (ζ_{DK}), Park-Schapery (ζ_{PS}), and Ninomiya-Ferry (ζ_{NF}) methods.

Core	Lift	ζ_{OB}	ζ_{DK}	ζ_{PS}	ζ_{NF}
GA-10A	1	1.26%	4.58%	0.50%	0.56%
	2	1.41%	4.24%	0.53%	0.54%
	3	1.19%	3.09%	0.46%	0.51%
GA-10B	1	1.30%	4.41%	0.48%	0.56%
	2	1.14%	3.83%	0.43%	0.55%
	3	1.24%	4.66%	0.45%	0.57%
GA-11	1	1.16%	4.62%	0.48%	0.57%
	2	1.18%	5.13%	0.47%	0.59%
GA-22	1	1.16%	2.70%	0.39%	0.51%
	2	1.86%	5.94%	0.62%	0.59%
	3	1.07%	4.43%	0.44%	0.57%
	4	1.48%	2.55%	0.42%	0.51%
	5	1.06%	2.91%	0.46%	0.50%
GA-26	1	1.34%	2.42%	0.36%	0.50%
GA-57	1	1.06%	3.76%	0.42%	0.55%
	2	1.30%	4.41%	0.48%	0.56%
GA-82A	1	1.57%	1.79%	0.34%	0.46%
GA-82B	1	1.01%	3.24%	0.41%	0.53%
GA-129	1	2.04%	5.34%	0.89%	0.55%
Mean:		1.31%	3.90%	0.48%	0.54%

conversions overall compared to $\beta = 0.08$, as used by Daniel and Kim [86]. The DK method produced $|E^*| \rightarrow E(t)$ conversion errors threefold greater than OB on average. Conversely, the PS

and NF methods consistently produced more accurate $E(t)$ approximations than OB, although the difference in error magnitudes was smaller than that between DK and OB.

The best (PG-67B) and worst (PG-64B) OB conversions of the lab set are plotted alongside their corresponding $\boldsymbol{E_P(t)}$ curves in Figs. 7.3a and 7.3b. Similarly, the best (GA-82B) and worst (GA-129) OB conversions from the *in situ* data set are presented in Figs. 7.4a and 7.4b. The approximately converted relaxation moduli obtained from the PS, NF, and DK methods are also included for comparison. It is difficult to ascertain the differences among the curves from visual inspection due to the logarithmic scale; consequently, the percent errors of the approximately converted moduli relative to their respective near-exactly converted moduli are given in Figs. 7.3c, 7.3d, 7.4c, and 7.4d. A wavelike pattern can be seen in the percent difference comparisons, especially for the PS and NF curves. The pattern arises due to the shape of the Prony series, which contains small waves between the relaxation times, ρ_j. The waves are virtually imperceptible on logarithmic scale as in Figs. 7.3a and 7.3b; however, they become visible on linear vertical scale as in Figs. 7.3c and 7.3d.

The percent error of the DK method is significantly greater overall compared to that of the other three methods on the domain spanning $10^{-4} \leq t \leq 10^4$ s. The PS and NF methods result in the lowest overall percent difference from the near-exact relaxation modulus, which is likely due to having more complicated conversion procedures than the OB and DK methods. Most notably, the OB method demonstrates significantly lower error than the DK method despite using the same conversion approach.

Although the PS and NF methods produced more accurate $|E^*| \rightarrow E(t)$ conversions than OB, they have greater restrictions to their applicability. The NF approach requires a combination of any two of $E^{'}$, $E^{''}$, and $E(t)$ to approximate the third, which effectively limits it to one-way conversion from $|E^*|$ to $E(t)$ in practice. The PS method does not share this limitation; however, it requires determining the slope of the known modulus on logarithmic scale at all time/frequency points, which can be difficult depending on smoothness of the data. Compared to these methods, the OB approach is both quicker and easier to implement in practice with minor cost to accuracy. Furthermore, OB is capable of interconverting $|E^*|$ and $E(t)$ measurements without using a modeling function such as a sigmoid or Prony series—which is infeasible for NF and impossible for PS.

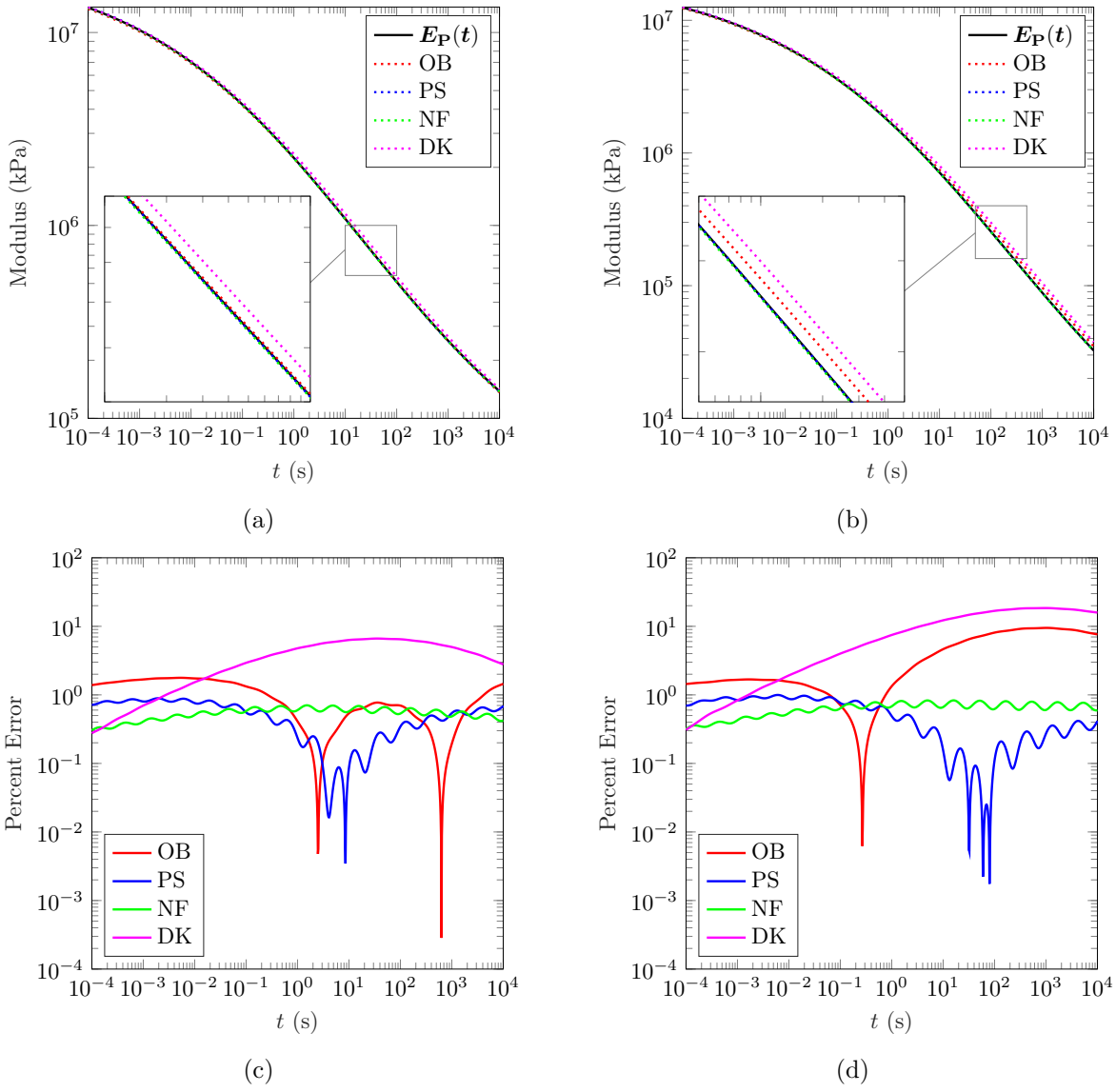

Figure 7.3. Near-exactly converted relaxation modulus, $\boldsymbol{E_P(t)}$, plotted with the approximately converted moduli from the OB, PS, NF, and DK methods for (a) PG-67B and (b) PG-64B. Percent errors of the approximate conversions with respect to the near-exactly converted modulus are also given for (c) PG-67B and (d) PG-64B.

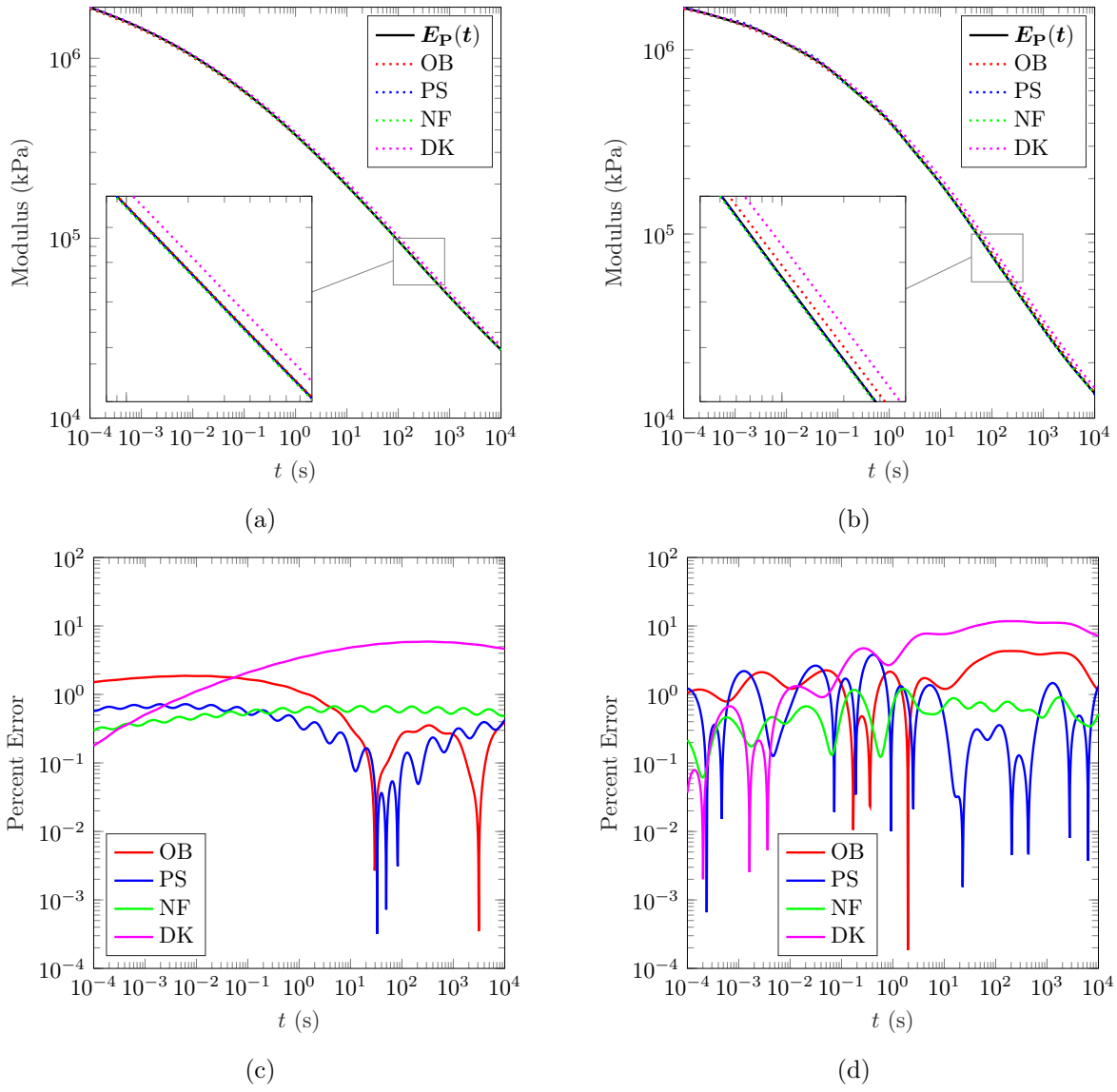

Figure 7.4. Near-exactly converted relaxation modulus, $\boldsymbol{E_P(t)}$, plotted with the approximately converted moduli from the OB, PS, NF, and DK methods for (a) GA-82B and (b) GA-129. Percent errors of the approximate conversions with respect to the near-exactly converted modulus are also given for (c) PG-67B and (d) PG-64B.

7.4 Conclusions

7.4.1 Summary

In this chapter, numerical studies were conducted to determine a generally appropriate value for β when converting between sigmoidal functions for $E(t)$ and $|E^*|$. Two data sets of AMPT-measured dynamic modulus were used for the study, where the first set contains 11 lab-prepared asphalt samples, and the second set comprises 19 samples taken from *in situ* asphalt pavements. A robust numerical procedure was used to determine the optimal β value for each pavement sample. Statistical analysis of the results suggests the appropriate value is $\beta_{\text{opt}} = 0.0673 \pm 0.0009$ with 95% confidence.

The effectiveness of the optimal β approach was compared to other approximate $|E^*|/E(t)$ interconversion techniques, namely the Daniel-Kim, Park-Schapery, and Ninomiya-Ferry methods. The DK method uses the same β factor approach to interconversion as the OB approach, whereas the PS and NF methods employ more sophisticated procedures. The proposed OB approach produced conversion errors of 1.41% among all 30 asphalt samples, compared to 4.3%, 0.51%, and 0.55% using the DK, PS, and NF methods, respectively. Although the OB method produced slightly higher errors than PS and NF, it is significantly easier to implement and involves fewer restrictions. Additionally, OB led to notably lower conversion errors than DK, which was identified from literature as the most accurate previous approach using the β factor.

7.4.2 Limitations

Limitations of the results are as follows. First, only experimental data for $|E^*|$ was used for the studies. Consequently, when individually determining the optimal β value for each asphalt sample, the $E(t)$ converted by OB was validated against an $E(t)$ derived from a near-exact Prony series fit. Ideally, the $E(t)$ used for validating the OB conversion should be obtained from experimental relaxation testing. Another restriction of the present study is that all test data are based on hot mix asphalt materials used in Georgia, USA, such as PG 64-22, PG 67-22, and PG 76-22. Although these mixtures are used elsewhere, it would be beneficial to expand the study to include data representative of a wider variety of asphalt materials.

Four different VW pavement models—denoted A, B, C, and D—are used in all studies. Each model consists of four axisymmetric material layers: two distinct asphalt concrete layers at the top, a graded aggregate base (GAB) layer (*i.e.*, crushed rock) in the middle, and a subgrade soil layer at the foundation. A visualization of the general layout used for all models is shown in Fig. 4.4, and the material properties and geometry of each are given in Table 4.1. The values for the dynamic moduli (d_1–d_4) are derived from various hot mix asphalt samples tested by Kim *et al.* [5], and an overall damping of 0.1% is assumed for all cases. The remaining material property and geometry values are chosen from ranges based on pavement configurations common in Georgia, USA.

Chapter 8

Conclusion

8.1 Summary

New techniques and analyses are provided in this dissertation to improve FWD backcalculation efficacy. The included studies address gaps in the research space which concern issues that are the most hindering to backcalculation accuracy. Special attention is given to the optimization involved, which has seen little investigation over the years despite playing an integral role in backcalculation. In particular, ill-posedness and the effective frequency range are considerably examined, which are two pervasive computational issues that have only recently been discovered in the optimization.

The contributions of this dissertation are organized into five key topics as follows:

1. The development of UGA-PAVE—a dynamic, gradient-based FWD backcalculation software which contains a novel optimization method.

2. Verification of UGA-PAVE via backcalculation of accurate pavement layer moduli under ill-posed optimization.

3. Validation of dynamic modulus backcalculated by UGA-PAVE with lab-measured data.

4. Examination of changes to the FWD testing procedure that can improve backcalculation accuracy.

5. An improved method for approximate conversion between widely used models of asphalt's viscoelastic stiffness.

The first topic is presented in Chapter 3, which contains a detailed theoretical description of the two major components of UGA-PAVE. The first component is ViscoWave, a state-of-the-art algorithm for modeling dynamic deflections in layered viscoelastic media developed by Lee [7]. The second component is tandem trust-region, a newly developed optimization method which is an amalgamation of the subspace trust-region interior reflective and Levenberg Marquardt algorithms.

The second topic is addressed in Chapter 4. The TTR optimizer is compared across 36,000 simulated ill-posed backcalculations to its constituents, STIR and LMA, as well as a robust commercial option, MATLAB's *lsqnonlin* package. The TTR algorithm exhibits the best overall performance for ill-posed optimization, including the identification of suitable minima (*i.e.*, sufficiently accurate dynamic modulus parameters).

The third topic is contained in Chapter 5. For the validation study, FWD testing was conducted at several locations across Georgia, USA, and pavement cores were extracted from the same locations and tested with an AMPT device. Then, the FWD-backcalculated dynamic modulus is compared to the dynamic modulus measured via AMPT. The dynamic modulus obtained from UGA-PAVE and AMPT exhibit good agreement within the EFR for locations where accurate knowledge of the pavement layer profile was available.

The fourth topic is covered in Chapter 6, wherein the effects of changes to the FWD testing setup on ill-posed optimization and the effective frequency range are investigated across 720,000 simulated backcalculations. Examination of the FWD load characteristics reveals the duration of the impact has the most significant effect on the EFR. Briefer impacts improve backcalculation accuracy by expanding the range of excited frequencies. Additionally, backcalculation performance can be significantly improved by using a number of displacement sensor measurements equal to or greater than the number of backcalculated layer moduli, which avoids ill-posed optimization.

Finally, Chapter 7 pertains to the fifth topic, in which a popular approach for approximate interconversion between dynamic modulus and relaxation modulus is improved. A rigorous numerical study is conducted using AMPT-measured dynamic modulus of 30 asphalt samples. Relaxation modulus is near-exactly converted for each sample. The improved technique, the optimal β method, is compared with three alternative approaches—the Daniel-Kim, Park-Schapery, and Ninomiya-Ferry methods—in approximate interconversion from $|E^*|$ to $E(t)$. The optimal β

method demonstrates similar performance as the best alternatives while being significantly easier to implement.

8.2 Outlook

The FWD remains a powerful tool for nondestructive asphalt pavement testing. However, significant issues are evident with the techniques that have been developed over the years for analyzing the FWD measurements. The vast majority of backcalculation research has been directed toward developing high fidelity pavement models. Indeed, these models boast impressive aptitude for simulating real-world behavior, but they constitute only half of the backcalculation methodology. The other half, optimization, has received comparatively little attention in the context of FWD backcalculation. This is a shocking revelation, because the intricacy and mathematical complexity of optimization theory rivals that of physics modeling.

Although many issues and limitations exist with FWD backcalculation (as with any methodology), the author believe the two most important issues to address are currently the effective frequency range and ill-posed optimization. The most widely regarded downside of FWD testing is it requires traffic lanes to be closed for long time periods to conduct testing. Sufficient expansion of the EFR can reduce the number of temperatures required to determine an $|E^*|$ mastercurve from FWD testing (vis-à-vis time-temperature superposition), meaning less testing needs to be conducted. On the other hand, ill-posed optimization significantly hinders the likelihood that a backcalculated result accurately reflects reality—regardless of the range of frequencies covered by the EFR. Both issues are integral to the efficacy of FWD backcalculation and should be given significantly more attention.

Finally, the approach used to solve the inverse problem in FWD backcalculation is known as a model updating procedure. Such approaches are surely powerful, but they are notorious for being computationally expensive. Great strides have been made recently in Bayesian inference, an indirect method for solving inverse problems. Bayesian inference is a remarkably powerful technique that inherently contains regularization properties (useful for ill-posed problems), and it has demonstrated capability for accurately predicting dynamic responses of structures despite modeling errors (a common situation in FWD practice). Based on these qualities and its high

computational efficiency, the author believes Bayesian inference may have the potential to be the most significant advancement in FWD backcalculation methodology since the advent of dynamic approaches.

Bibliography

[1] M. A. Branch, T. F. Coleman, and Y. Li, "A subspace, interior, and conjugate gradient method for large-scale bound-constrained minimization problems," *SIAM J. Sci. Comput.*, vol. 21, pp. 1–23, 1999.

[2] S. Bellavia and E. Riccietti, "On an elliptical trust-region procedure for ill-posed nonlinear least-squares problems," *J. Optim. Theory Appl.*, vol. 178, pp. 824–859, 2018.

[3] A. R. Conn, N. I. Gould, and P. L. Toint, *Trust-Region Methods*. Mathematical Programming Society/Society for Industrial and Applied Mathematics, 2000.

[4] T. F. Coleman and Y. Li, "A reflective Newton method for minimizing a quadratic function subject to bounds on the variables," *SIAM Journal on Optimization*, vol. 6, no. 4, pp. 1040–1058, 1996.

[5] S.-H. Kim, R. A. Etheridge, M. G. Chrozepa, and Y. R. Kim, "Development of MEPDG input database for asphalt mixtures," Tech. Rep. 16-19, GDOT Research Project, April 2019.

[6] S. S. Kim, H. S. Lee, S. A. Durham, R. B. Davis, and R. C. Romeo, "Updated layer coefficients for GDOT flexible pavement design," Tech. Rep. FHWA-GA-22-1805, Georgia Department of Transportation, 2022.

[7] H. S. Lee, *Development of a new solution for viscoelastic wave propogation of pavement structures and its use in dynamic backcalculation*. PhD thesis, Michigan State University, 2013.

[8] A. Bohn, P. Ullidtz, R. Stubstad, and A. Sorensen, "Danish experiments with the French falling weight deflectometer," in *Third International Conference on the Structural Design of Asphalt Pavements*, pp. 1119–1128, 1972.

[9] R. E. Smith and R. L. Lytton, "Operating characteristics and user satisfaction of commerically available NDT equipment," *Transportation Research Record*, vol. 1007, pp. 1–10, 1985.

[10] W. M. Moore, D. I. Hanson, and J. W. Hall, "An introduction to nondestructive structural evaluation of pavements," *Transportation Research Circular*, no. 189, 1978.

[11] N. M. Isada, "Detecting variations in load-carrying capacity of flexible pavements," Tech. Rep. 21, NCHRP Report, 1966.

[12] F. W. Brands and J. C. Cook, "Pavement deflection measurement - dynamic - phase III WSU impulse index computer, section I (suitcase)," Tech. Rep. H-37, Washington State Highway Commission, 1972.

[13] F. W. Brands and J. C. Cook, "Pavement deflection measurement - dynamic - phase III section II (vehicle)," Tech. Rep. H-38, Washington State Highway Commission, 1972.

[14] H. Ceylan, K. Gopalakrishnan, and A. Guclu, "Advanced approaches to characterizing non-linear pavement system responses," *Transportation Research Record*, vol. 2005, pp. 86–94, 2007.

[15] S. Zaghloul and T. White, "Use of a three-dimensional, dynamic finite element program for analysis of flexible pavement," *Transportation Research Record*, vol. 1388, pp. 60–69, 1993.

[16] M. Saltan and M. Karasahin, "A finite element based backcalculation program for flexible pavements," *Indian Journal of Engineering & Materials Sciences*, vol. 13, pp. 221–230, 2006.

[17] A. B. Goktepe, E. Agar, and A. H. Lav, "Advances in backcalculating the mechanical properties of flexible pavements," *Advances in Engineering Software*, vol. 37, pp. 421–431, 2006.

[18] R. Liang and S. Zeng, "Efficient dynamic analysis of multilayered system during Falling Weight Deflectometer experiments," *Journal of Transportation Engineering*, vol. 128, no. 4, pp. 366–374, 2002.

[19] K. Gopalakrishnan, S. Kim, H. Ceylan, and O. Kaya, "Development of asphalt dynamic modulus master curve using falling weight deflectometer measurements, TR-659," *InTrans Project Reports*, p. 69, 2014.

[20] D. Cao, Y. Zhao, W. Liu, and J. Ouyang, "Comparisons of asphalt pavement responses computed using layer properties backcalculated from dynamic and static approaches," *Road Mater Pavement Des*, vol. 20, pp. 1114–1130, 2019.

[21] R. Y. Liang and J. X. Zhu, "Efficient computational algorithms for forward and backward analysis of a dynamic pavement system," *Computers & Structures*, vol. 69, pp. 255–263, 1998.

[22] R. W. Meier and G. J. Rix, "Backcalculation of flexible pavement moduli from falling weight deflectometer data using artificial neural networks," *Transportation Research Record*, vol. 1473, pp. 72–81, 1995.

[23] K. Chatti, Y. Ji, and R. Harichandran, "Dynamic time domain backcalculation of layer moduli, damping, and thicknesses in flexible pavements," *Transportation Research Record*, vol. 1869, pp. 106–116, 2004.

[24] S. Varma, M. E. Kutay, and E. Levenberg, "Viscoelastic genetic algorithm for inverse analysis of asphalt layer properties from falling weight deflections," *Transportation Research Record*, vol. 2369, pp. 38–46, 2013.

[25] H. S. Lee, D. Ayyala, and H. V. Quintus, "Dynamic backcalculation of viscoelastic asphalt properties and master curve construction," *Transportation Research Record*, vol. 2641, pp. 29–38, 2017.

[26] S. S. Madsen and E. Levenberg, "Dynamic backcalculation with different load-time histories," *Road Materials and Pavement Design*, vol. 19:6, pp. 1314–1333, 2018.

[27] M. Li and H. Wang, "Prediction of asphalt pavement responses from FWD surface deflections using soft computing methods," *Journal of Transportation Engineering*, 2018.

[28] P. Liu, D. Wang, and M. Oeser, "Application of semi-analytical finite element method coupled with infinite element for analysis of asphalt pavement structural response," *J Traffic Transp Eng (Engl Ed)*, vol. 2, pp. 48–58, 2015.

[29] H. Wang and M. Li, "Comparative study of asphalt pavement responses under FWD and moving vehicular loading," *J Transp Eng*, vol. 142, p. 04016069, 2016.

[30] I. Wollny and F. H. M. Kaliske, "Numerical modeling of inelastic structures at loading of steady state rolling," *Comput Mech*, vol. 57, pp. 867–886, 2016.

[31] M. Kaliske, R. Behnke, F. Hartung, and I. Wollny, "Multi-physical and multi-scale theoretical-numerical modeling of tire-pavement interaction," in *Coupled System Pavement–Tire–Vehicle*, pp. 1–39, 2021.

[32] E. Levenberg, "Inverse analysis of viscoelastic pavement properties using data from embedded instrumentation," *Int J Numer Anal Methods Geomech*, vol. 37, pp. 1016–1033, 2013.

[33] M. Nasimifar, S. Thyagarajan, and N. Sivaneswaran, "Backcalculation of flexible pavement layer moduli from traffic speed deflectometer data," *Transp Res Rec*, vol. 2641, pp. 66–74, 2017.

[34] S. Andersen, E. Levenberg, and M. B. Andersen, "Inferring pavement layer properties from a moving measurement platform," in *Bearing Capacity of Roads, Railways and Airfields*, pp. 675–682, 2017.

[35] C. P. Nielsen, "Visco-elastic back-calculation of traffic speed deflectometer measurements," *Transp Res Rec*, vol. 2673, pp. 439–448, 2019.

[36] C. Wu, H. Wang, J. Zhao, X. Jiang, and Y. Qiu, "Asphalt pavement modulus backcalculation using surface deflections under moving loads," *Comput-Aided Civ Infrastruct Eng*, vol. 35, pp. 1246–1260, 2020.

[37] J. Fan, T. Ma, J. Zhu, Y. Zhu, and Y. Zhang, "Characteristics of high-speed deflection basin and structural parameter back-calculation of asphalt pavement with different structural states," *Constr Build Mater*, vol. 341, p. 127869, 2022.

[38] Z. Sun, C. Kasbergen, K. N. van Dalen, K. Anupam, A. Skarpas, and S. M. J. G. Erkens, "A parameter identification technique for traffic speed deflectometer tests of pavements," *Road Mater Pavement Des*, 2022.

[39] E. Levenberg, M. Pettinari, S. Baltzer, and B. M. L. Christensen, "Comparing traffic speed deflectometer and falling weight deflectometer data," *Transp Res Rec*, vol. 2672, pp. 22–31, 2018.

[40] D. Steele, H. S. Lee, C. Beckemeyer, and T. Van, "Moving wheel versus impact deflections and their use in pavement evaluation," *Transp Res Rec*, vol. 2675, pp. 293–305, 2021.

[41] J. Berenger, "A perfectly matched layer for the absorption of electromagnetic waves," *Journal of Computational Physics*, vol. 114, no. 2, pp. 185–200, 1994.

[42] U. Basu and A. K. Chopra, "Perfectly matched layers for time-harmonic elastodynamics of unbounded domains: theory and finite-element implementation," *Computer Methods in Applied Mechanics and Engineering*, vol. 192, pp. 1337–1375, 2003.

[43] S. S. Madsen, S. Krenk, and O. Hededal, "Perfectly matched layer (PML) for transient wave propagation in a moving frame of reference," in *4th ECCOMAS Thematic Conference on Computational Methods in Structural Dynamics and Earthquake Engineering*, 2013.

[44] H. Kohno, K. J. Bathe, and J. C. Wright, "A finite element procedure for multiscale wave equations with application to plasma waves," *Computers and Structures*, vol. 88, pp. 87–94, 2010.

[45] S. Ham and K. J. Bathe, "A finite element method enriched for wave propagation problems," *Computers and Structures*, vol. 94–95, pp. 1–12, 2012.

[46] W. T. Thomson, "Transmission of elastic waves through a stratified solid medium," *Journal of Applied Physics*, vol. 21, pp. 89–93, 1950.

[47] N. A. Haskell, "The dispersion of surface waves on multilayered media," *Bulletin of Seismological Society of America*, vol. 43, pp. 17–34, 1953.

[48] E. Kausel and J. M. Roësset, "Stiffness matrices for layered soils," *Bulletin of the Seismological Society of America*, vol. 71, pp. 1743–1761, 1981.

[49] J. Lysmer, "Lumped mass method for Rayleigh waves," *Bulletin of the Seismological Society of America*, vol. 60, pp. 89–104, 1970.

[50] S. A. Rizzi and J. F. Doyle, "A spectral element approach to wave motion in layered solids," *Journal of Vibration and Acoustics*, vol. 114, pp. 569–577, 1992.

[51] J. F. Doyle, *Wave Propagation in Structures: Spectral Analysis Using Fast Discrete Fourier Transforms*. New York: Springer, 1997.

[52] R. Al-Khoury, A. Scarpas, C. Kasbergen, and J. Blaauwendraad, "Spectral element technique for efficient parameter identification of layered media. I. Forward calculation," *International Journal of Solids and Structures*, vol. 38, pp. 1605–1623, 2001.

[53] R. Al-Khoury, A. Scarpas, C. Kasbergen, and J. Blaauwendraad, "Spectral element technique for efficient parameter identification of layered media. part II: Inverse calculation," *International Journal of Solids and Structures*, vol. 38, pp. 8753–8772, 2001.

[54] R. Al-Khoury, A. Scarpas, C. Kasbergen, and J. Blaauwendraad, "Spectral element technique for efficient parameter identification of layered media. part III: Viscoelastic aspects," *International Journal of Solids and Structures*, vol. 39, pp. 2189–2201, 2002.

[55] K. Chatti and K. K. Yun, "SAPSI-M: Computer program for analyzing asphalt concrete pavements under moving arbitrary loads," *Transportation Research Record*, vol. 1539, pp. 88–95, 1996.

[56] Y. Ji, *Frequency and time domain backcalculation of flexible pavement layer parameters*. PhD thesis, Michigan State University, 2005.

[57] W. Zhang, A. Drescher, and D. E. Newcomb, "Viscoelastic analysis of diametral compression of asphalt concrete," *Journal of Engineering Mechanics*, vol. 123, pp. 596–603, 1997.

[58] W. Zhang, A. Drescher, and D. E. Newcomb, "Viscoelastic behavior of asphalt concrete in diametral compression," *Journal of Transportation Engineering*, vol. 123, pp. 495–502, 1997.

[59] J. S. Bendat and A. G. Piersol, *Random Data: Analysis and Measurement Procedures*. New Jersey: John Wiley & Sons, Inc., 4 ed., 2010.

[60] H. S. Lee, "Viscowave–A new solution for viscoelastic wave propagation of layered structures subjected to an impact load," *International Journal of Pavement Engineering*, vol. 15, pp. 542–557, 2014.

[61] H. S. Lee, D. Steele, and H. V. Quintus, "Who says backcalculation is only about layer moduli?," *Transportation Research Record*, vol. 2673, pp. 317–331, 2019.

[62] Y.-C. Lee, Y. R. Kim, and S. R. Ranjithan, "Dynamic analysis-based approach to determine flexible pavement layer moduli using deflection basin parameters," *Transp Res Rec*, vol. 1639, pp. 36–42, 1998.

[63] O. Pekcan, E. Tutumluer, and M. R. Thompson, "Nondestructive flexible pavement evaluation using ILLI-PAVE based artificial neural network models," in *Geocongress 2006*, pp. 1–6, 2006.

[64] N. Rakesh, A. K. Jain, M. A. Reddy, and K. S. Reddy, "Artificial neural networks–genetic algorithm based model for backcalculation of pavement layer moduli," *Int J Pavement Eng*, vol. 7, pp. 221–230, 2006.

[65] S. Sharma and A. Das, "Backcalculation of pavement layer moduli from falling weight deflectometer data using an artificial neural network," *Canadian J Civ Eng*, vol. 35, pp. 57–66, 2008.

[66] H. Wang, M. Li, P. Szary, and X. Hu, "Structural assessment of asphalt pavement condition using backcalculated modulus and field data," *Constr Build Mater*, vol. 211, pp. 943–951, 2019.

[67] M. Li and H. Wang, "Development of ANN-GA program for backcalculation of pavement moduli under FWD testing with viscoelastic and nonlinear parameters," *International Journal of Pavement Engineering*, 2017.

[68] S. I. Kabanikhin, "Definitions and examples of inverse and ill-posed problems," *J. Inv. Ill-Posed Problems*, vol. 17, pp. 317–357, 2008.

[69] X. G. Hua, Y. Q. Ni, and J. M. Ko, "Adaptive regularization parameter optimization in output-error-based finite element model updating," *Mechanical Systems and Signal Processing*, vol. 23, pp. 563–579, 2009.

[70] R. Dongré, L. Myers, and J. D'Angelo, "Conversion of testing frequency to loading time: Impact on performance predictions obatined from the M-E Pavement Design Guide," in *Transportation Research Board 85th Annual Meeting*, pp. 574–579, 2006.

[71] Y. R. Kim, *Modeling of Asphalt Concrete*. The American Society of Civil Engineers Press, 2009.

[72] T. Pellinen, M. Witczak, and R. Bonaquist, "Asphalt mix master curve construction using sigmoidal fitting function with non-linear least squares optimization," in *15th ASCE Engineering Mechanics Conference*, 2002.

[73] I. Zaabar, K. Chatti, H. S. Lee, and N. Lajnef, "Backcalculation of asphalt concrete modulus master curve from field-measured falling weight deflectometer data," *Transportation Research Record*, vol. 2457, pp. 80–92, 2014.

[74] S. Varma and M. E. Kutay, "Backcalculation of viscoelastic and nonlinear flexible pavement layer properties from falling weight deflections," *International Journal of Pavement Engineering*, vol. 17:5, pp. 388–402, 2016.

[75] F. R. Schwarzl and L. C. E. Struik, "Analysis of relaxation measurements," *Advances in Molecular Relaxation Processes*, vol. 1, pp. 201–255, 1968.

[76] J. D. Ferry, *Viscoelastic Properties of Polymers*. Wiley, New York, 1980.

[77] R. M. Christensen, *Theory of Viscoelasticity: An Introduction*. Academic Press, 1982.

[78] N. W. Tschoegl, *The phenomenological theory of linear viscoelastic behavior: An introduction*. Springer-Verlag, 1989.

[79] S. W. Park and R. A. Schapery, "Methods of interconversion between linear viscoelastic material functions. Part I—a numerical method based on Prony series," *International Journal of Solids and Structures*, vol. 36, pp. 1653–1675, 1999.

[80] K. Ninomiya and J. D. Ferry, "Some approximate equations useful in the phnomenological treatment of linear viscoelastic data," *Journal of Colloid Science*, vol. 14, pp. 36–48, 1959.

[81] P. Fernández, D. Rodríguez, M. J. Lamela, and A. Fernández-Canteli, "Study of the interconversion between viscoelastic behaviour functions of PMMA," *Mechanics of Time-Dependent Materials*, vol. 15, pp. 169–180, 2011.

[82] S. W. Park and R. A. Schapery, "Methods of interconversion between linear viscoelastic material functions. Part II—an approximate analytical method," *International Journal of Solids and Structures*, vol. 36, pp. 1677–1699, 1999.

[83] S. Mun, G. R. Chehab, and Y. R. Kim, "Determination of time-domain viscoelastic functions using optimized interconversion techniques," *Road Materials and Pavement Design*, vol. 8, pp. 351–365, 2007.

[84] R. A. Tarefder and A. S. M. Asifur Rahman, "Interconversion of dynamic modulus to creep compliance and relaxation modulus: Numerical modeling and laboratory validation," Tech. Rep. 456-438, Nevada Department of Transportation, September 2016.

[85] A. S. M. Asifur Rahman and R. A. Tarefder, "Interconversion of frequency domain complex modulus to time domain modulus and compliance of asphalt concrete: Numerical modeling and laboratory validation," in *Proceedings of the ASME 2016 International Mechanical Engineering Congress and Exposition*, no. IMECE2016-66292, 2016.

[86] J. S. Daniel and Y. R. Kim, "Relationships among rate-dependent stiffnesses of asphalt concrete using laboratory and field test methods," *Transportation Research Record*, vol. 1630, pp. 3–9, 1998.

[87] I. L. Al-Qadi, M. A. Elseifi, P. J. Yoo, S. H. Dessouky, N. Gibson, T. Harman, J. D'Angelo, and K. Petros, "Accuracy of current complex modulus selection procedure from vehicular load pulse," *Transportation Research Record*, vol. 2087, pp. 81–90, 2008.

[88] I. L. Al-Qadi, W. Xie, and M. A. Elseifi, "Frequency determination from vehicular loading time pulse to predict appropriate complex modulus in MEPDG," *Journal of the Association of Asphalt Paving Technologists*, vol. 77, pp. 739–772, 2008.

[89] M. W. Witczak, K. Kaloush, T. Pellinen, M. El-Basyouny, and H. Von Quintus, "Simple performance test for superpave mix design," Tech. Rep. 465, NCHRP, 2002.

[90] A. Loulizi, G. W. Flintsch, and K. McGhee, "Determination of in-place hot-mix asphalt layer modulus for rehabilitation projects by a mechanistic-empirical procedure," *Transportation Research Record*, vol. 2037, pp. 53–62, 2007.

[91] F. Leiva-Villacorta and D. Timm, "Falling weight deflectometer loading pulse duration and its effect on predicted pavement responses," in *92nd Annual Meeting on Transportation Research Board*, pp. 13–22171, 2013.

[92] V. P. Le, H. J. Lee, J. M. Flores, W. J. Kim, and J. Baek, "New approach to construct master curve of damaged asphalt concrete based on falling weight deflectometer back-calculated moduli," *Journal of Transportation Engineering*, vol. 142(11), p. 04016048, 2016.

[93] D. Cao, C. Zhou, Y. Zhao, G. Fu, and W. Liu, "Effectiveness of static and dynamic backcalculation approaches for asphalt pavement," *Canadian Journal of Civil Engineering*, vol. 47, pp. 846–855, 2020.

[94] Y. Deng, X. Luo, Y. Zhang, S. Cai, K. Huang, X. Shi, and R. L. Lytton, "Determination of flexible pavement deterioration conditions using Long-Term Pavement Performance database and artificial intelligence-based finite element model updating," *Structural Control and Health Monitoring*, vol. 28, p. e2671, 2021.

[95] R. C. Koole, "Overlay design based on falling weight deflectometer measurements," *Transportation Research Record*, vol. 700, pp. 59–72, 1979.

[96] B. Sebaaly, T. G. Davies, and M. S. Mamlouk, "Dynamics of falling weight deflectometer," *J. Transp. Eng.*, vol. 111(6), pp. 618–632, 1985.

[97] Y. R. Kim, B. Xu, and Y. Kim, "A new backcalculation procedure based on dispersion analysis of fwd time-history deflections and surface wave measurements using artificial neural networks," in *Nondestructive Testing of Pavement and Backcalculation of Moduli: Third Volume*, pp. 297–312, 2000.

[98] K. Chatti and L. Lei, "Forward calculation of subgrade modulus using falling weight deflectometer time histories and wave propagation theory," in *GeoCongress 2012*, pp. 1400–1409, 2012.

[99] Y. Zhao, D. Cao, and P. Chen, "Dynamic backcalculation of asphalt pavement layer properties using spectral element method," *Road Materials and Pavement Design*, vol. 16:4, pp. 870–888, 2015.

[100] G. Bazi and T. B. Assi, "Asphalt concrete master curve using dynamic backcalculation," *International Journal of Pavement Engineering*, vol. 23, pp. 95–106, 2020.

[101] G. Fu, C. Zhou, and W. Liu, "Determination of effective frequency range excited by falling weight deflectometer loading history for asphalt pavement," *Construction and Building Materials*, vol. 235, no. 117792, 2020.

[102] T. G. Davies and M. S. Mamlouk, "Theoretical response of multilayer pavement systems to dynamic nondestructive testing," *Transportation Research Record*, vol. 1022, pp. 1–7, 1985.

[103] G. Turkiyyah, "Feasibility of backcalculation procedures based on dynamic FWD response data," Tech. Rep. WA-RD 586.1, Washington State DOT, 2005.

[104] "JILS instrumentation specifications." https://www.jilsfwd.com/products/fwd-hwd-equipment.php. Accessed: 2010-10-29.

[105] K. F. Graff, *Wave Motion in Elastic Solids*. Dover Publications, Inc., 1975.

[106] P. Cornille, "Computation of hankel transforms," *SIAM Review*, vol. 14, pp. 278–285, 1972.

[107] Y. R. Kim, "General viscoelastic solutions for the multilayered systems subjected to static and moving loads," *Journal of Materials in Civil Engineering*, vol. 23, pp. 1007–1016, 2011.

[108] J. Abate and P. P. Valko, "Multi-precision Laplace transform inversion," *International Journal for Numerical Methods in Engineering*, vol. 60, pp. 979–993, 2004.

[109] N. Sivaneswaran, S. L. Kramer, and J. P. Mahoney, "Advanced backcalculation using a nonlinear least squares optimization technique," *Transportation Research Record*, vol. 1293, pp. 93–102, 1991.

[110] T. F. Coleman and Y. Li, "An interior trust region approach for nonlinear minimization subject to bounds," *SIAM Journal on Optimization*, vol. 6, no. 2, pp. 418–445, 1996.

[111] J. J. Moré and D. C. Sorensen, "On the use of directions of negative curvature in a modified Newton method," *Mathematical Programming*, vol. 16, pp. 1–20, 1979.

[112] J. J. Moré and D. C. Sorensen, "Computing a trust region step," *SIAM J. Sci. Stat. Comput.*, vol. 4, no. 3, pp. 553–572, 1983.

[113] D. C. Sorensen, "Minimization of a large-scale quadratic function subject to a spherical constraint," *Siam J. Optim.*, vol. 7, pp. 141–161, 1997.

[114] K. Levenberg, "A method for the solution of certain non-linear problems in least squares," *Quarterly of Applied Mathematics*, vol. 2, no. 2, pp. 164–168, 1944.

[115] D. D. Morrison, "Methods for nonlinear least squares problems and convergence proofs," in *Tracking Programs and Orbit Determination*, pp. 1–9, 1960.

[116] D. W. Marquardt, "An algorithm for least-squares estimation of nonlinear parameters," *Journal of the Societ for Industrial and Applied Mathematics*, vol. 11, no. 2, pp. 431–441, 1963.

[117] "Matlab Optimization Toolbox," 2022. The MathWorks, Natick, MA, USA.

[118] A. A. Giunta, S. F. Wojtkiewics, and M. S. Eldred, "Overview of modern design of experiments methods for computational simulations," in *41st AIAA Aerospace Sciences Meeting and Exhibit*, 2003.

[119] AASHTO, *AASHTO Interim Guide for Design of Pavement Structures*. American Association of State Highway and Transportation Officials, 1972.

[120] V. C. Janoo, "Layer coefficients for NHDOT pavement materials," Tech. Rep. 94-30, U.S. Army Corps of Engineers: Cold Regions Research & Engineering Laboratory, September 1994.

[121] H. U. Bahia, P. J. Bosscher, J. Christensen, and Y. H. Hu, "Layer coefficients for new and reprocessed asphaltic mixes," Tech. Rep. WI/SPR 04-00, Wisconsin Department of Transportation, 2000.

[122] K. Peters-Davis and D. H. Timm, "Recalibration of the asphalt layer coefficient," Tech. Rep. 09-03, National Center for Asphalt Technology, Auburn University, 2009.

[123] R. K. Taylor, "Structural coefficient for high polymer modified asphalt mixes," Tech. Rep. Final Report BE321, Florida Department of Transportation, 2019.

[124] AASHTO, *Guide for Design of Pavement Structures*. American Association of State Highway and Transportation Officials, 1993.

[125] M. A. Lanotte and M. E. Kutay, "Determination of AASHTO 1993 layer coefficients consider time- and temperature-dependency of the asphalt mixture," in 10^{th} *International Conference on the Bearing Capacity of Roads, Railways, and Airfields*, 2017.

[126] R. Nemati, E. V. Dave, and J. E. Sias, "Generalized methodology to develop mechanistically informed asphalt mixture layer coefficients for aashto 1993 pavement design approach," *Transportation Research Record*, 2021.

[127] R. N. Stubstad, Y. J. Jiang, M. L. Clevenson, and E. O. Lukanen, "Review of the long-term pavement performance backcalculation results–final report," Tech. Rep. FHWA-HRT-05-150, Federal Highway Administration, 2006.

[128] "MATLAB Statistics and Machine Learning Toolbox," 2022. The MathWorks, Natick, MA, USA.